MECHANICAL PROPERTIES OF OXIDE DISPERSION STRENGTHENED INCONEL 625 ALLOY PRODUCED BY LASER POWDER BED FUSION

A THESIS SUBMITTED TO
THE GRADUATE SCHOOL OF NATURAL AND APPLIED SCIENCES
OF
MIDDLE EAST TECHNICAL UNIVERSITY

BY

KADİR TUĞRUL DEMİRCİ

IN PARTIAL FULFILLMENT OF THE REQUIREMENTS
FOR
THE DEGREE OF MASTER OF SCIENCE
IN
METALLURGICAL AND MATERIALS ENGINEERING

NOVEMBER 2024

Approval of the thesis:

MECHANICAL PROPERTIES OF OXIDE DISPERSION STRENGTHENED INCONEL 625 ALLOY PRODUCED BY LASER POWDER BED FUSION

submitted by **KADİR TUĞRUL DEMİRCİ** in partial fulfillment of the requirements for the degree of **Master of Science** i**n Metallurgical and Materials Engineering, Middle East Technical University** by,

Prof. Dr. Naci Emre Altun
Dean, **Graduate School of Natural and Applied Sciences** _____

Prof. Dr. Ali Kalkanlı
Head of the Department, **Metallurgical and Materials Eng.** _____

Prof. Dr. Arcan F. Dericioğlu
Supervisor, **Metallurgical and Materials Eng., METU** _____

Dr. Selen Nimet Gürbüz Güner
Co-Supervisor, **Nuclear Energy Research Institute, TENMAK** _____

Examining Committee Members:

Prof. Dr. C. Hakan Gür
Metallurgical and Materials Eng., METU _____

Prof. Dr. Arcan F. Dericioğlu
Metallurgical and Materials Eng., METU _____

Prof. Dr. Y. Eren Kalay
Metallurgical and Materials Eng., METU _____

Prof. Dr. Benat Koçkar
Mechanical Eng., Hacettepe University _____

Assist. Prof. Dr. Irmak Sargın
Metallurgical and Materials Eng., METU _____

Date: 26.11.2024

I hereby declare that all information in this document has been obtained and presented in accordance with academic rules and ethical conduct. I also declare that, as required by these rules and conduct, I have fully cited and referenced all material and results that are not original to this work.

Name, Last name : Kadir Tuğrul Demirci

Signature :

ABSTRACT

MECHANICAL PROPERTIES OF OXIDE DISPERSION STRENGTHENED INCONEL 625 ALLOY PRODUCED BY LASER POWDER BED FUSION

Demirci, Kadir Tuğrul
Master of Science, Metallurgical and Materials Engineering
Supervisor: Prof. Dr. Arcan F. Dericioğlu
Co-Supervisor: Dr. Selen Nimet Gürbüz Güner

November 2024, 139 pages

The global energy demand, especially in developing countries, is expected to increase by 50% in the coming decades due to improving living standards. Nuclear energy, especially produced by Generation IV reactors, will have a crucial role in meeting this demand. Among these, molten salt reactors (MSRs) stand out for their safety, efficiency, and versatility. However, current structural materials fail under the extreme conditions of MSRs, including high temperatures, radiation, and corrosive environments. Nickel-based superalloys are promising candidates for these challenges due to their high-temperature strength, resistance to radiation and corrosion. Oxide dispersion strengthening (ODS) can further enhance these properties, while additive manufacturing (AM) offers a sustainable route to produce complex ODS alloy geometries. In this study, a new ODS Inconel 625 (IN625) alloy, containing 0.3 wt% Y_2O_3 and 0.4 wt% Hf has been developed and produced, using laser powder bed fusion (L-PBF), which is one of the most important AM methods. A production matrix with varying laser power and scan velocity has led to over 99.9% densification for ODS IN625. Microstructural analysis revealed carbides and coarse oxide formations, while nano-oxides were observed using TEM. Two different heat treatments containing solutionizing and aging (SA), and direct aging

(DA) have been applied to the samples Among heat-treated materials, DA applied ODS samples possessed the optimal mechanical properties at both room temperature and at 700 °C. For comparison, same mechanical tests have been applied on a standard IN625 produced by L-PBF, along with a conventionally produced IN625 rod.

Keywords: Nuclear Energy, Inconel 625, Oxide Dispersion Strengthening, Laser Powder Bed Fusion, Mechanical Properties.

ÖZ

OKSİT DİSPERSİYONU İLE GÜÇLENDİRİLEN LAZER TOZ YATAK FÜZYONU İLE ÜRETİLMİŞ INCONEL 625 ALAŞIMLARININ MEKANİK ÖZELLİKLERİ

Demirci, Kadir Tuğrul
Yüksek Lisans, Metalurji ve Malzeme Mühendisliği
Tez Yöneticisi: Prof. Dr. Arcan F. Dericioğlu
Ortak Tez Yöneticisi: Dr. Selen Nimet Gürbüz Güner

Kasım 2024, 139 sayfa

Özellikle gelişmekte olan ülkelerde enerji talebinin, yaşam standartlarının yükselmesiyle birlikte önümüzdeki on yıllarda %50 oranında artması beklenmektedir. Özellikle IV. Nesil reaktörler tarafından üretilen nükleer enerji, bu talebin karşılanmasında kilit bir rol oynayacaktır. Eriyik tuz reaktörleri (MSR), eşsiz güvenlik, verimlilik ve çok yönlülük özellikleri nedeniyle yeni nesil reaktörler arasında önemli bir ilgi görmektedir. Bununla birlikte, mevcut yapısal malzemeler, yüksek sıcaklıklar, radyasyon ve korozif ortamlar gibi MSR'lerin ekstrem koşullarına dayanamaz. Nikel esaslı süperalaşımlar, yüksek sıcaklık dayanımları ve radyasyon ile korozyon dirençleri sayesinde bu zorluklar için güçlü adaylardır. Oksit dispersiyon güçlendirme (ODS), bu özellikleri daha da geliştirebilirken, eklemeli imalat (AM) karmaşık ODS alaşım geometrilerinin üretilmesi için sürdürülebilir bir yöntem sunmaktadır. Bu çalışmada, en önemli katmanlı imalat (AM) yöntemlerinden biri olan lazer toz yatağı füzyonu (L-PBF) kullanılarak, %0.3 ağırlık oranında Y_2O_3 ve %0.4 ağırlık oranında Hf içeren yeni bir ODS Inconel 625 (IN625) alaşımı geliştirilmiş ve üretilmiştir. Değişken lazer gücü ve tarama hızı değerlerini

içeren üretim matrisi, ODS IN625 için %99.9'dan fazla yoğunluk elde edilmesini sağlamıştır. Mikroyapısal analiz, karbürler ve iri oksit oluşumlarını ortaya çıkarırken, nano oksitler TEM kullanılarak gözlemlenmiştir. Numunelere çözündürme ve yaşlandırma ile doğrudan yaşlandırma içeren iki farklı ısıl işlem uygulanmıştır. Isıl işlem uygulanmış malzemeler arasında, doğrudan yaşlandırma uygulanmış ODS numuneleri hem oda sıcaklığında hem de 700 °C'de en uygun mekanik özelliklere sahip olmuştur. Karşılaştırma amacıyla, aynı mekanik testler L-PBF ile üretilmiş standart bir IN625 ve geleneksel yöntemle üretilmiş bir IN625 çubuğa da uygulanmıştır.

Anahtar Kelimeler: Nükleer Enerji, Inconel 625, Oksit Dispersiyonlu Güçlendirme, Lazer Toz Yatağı Füzyonu, Mekanik Özellikler.

To my dearest family

ACKNOWLEDGMENTS

I would like to express my sincere gratitude to my supervisor Prof. Dr. Arcan Dericioğlu, for his guidance and inspiration during this thesis. I am indebted to my co-advisor Dr. Selen Nimet Gürbüz Güner, for her unwavering support, valuable suggestions and dedication throughout this project. I am also thankful to my former supervisor, Assist. Prof. Dr. Eda Aydoğan Güngör, for her guidance and support.

This work was funded by Turkish Energy, Nuclear and Mineral Research Agency under project number A2.H1.P3. I would like to thank project members Assoc. Prof. Dr. Erhan Aksu, İlhan Bükülmez, Dr. Ömer Faruk Koç and Duygu Tatlıdil for their collaboration.

My special thanks go to my lab mates Aylin Aktaş, Yavuz Yıldız, Berk Tanrısevdi and Hasan Tahsin Koç, where I consider myself lucky to have worked beside them. I am grateful to Ali Özalp, for his endeavor on the mechanical testing of samples, and to Yeşim Yalçın and Umut Tukaç for their various yet profound help during this study.

I would like to acknowledge Dr. Murat Tolga Ertürk, Dr. Süha Tirkeş, Dr. Özgür Duygulu and Dr. Seçkin Öztürk for their assistance with materials testing and TEM analyses.

My heartfelt thanks go to Yeşim Atak, who has been everything I could ever need, whether as a friend, a co-worker, a mentor, or a sister; she has always been there for me in every possible way. I would like to thank Deniz and Fadik Nazlı Saraç, for their everlasting friendship and for inspiring me in ways they may not even realize.

Last but not least, to my parents, Münür and Fatma Demirci; and my brother, Yusuf Berker Demirci—your encouragement has been my strength. This work, and all I have ever accomplished, would not be possible without you. I am forever thankful for your presence in my life.

TABLE OF CONTENTS

LIST OF TABLES

TABLES

LIST OF FIGURES

FIGURES

LIST OF ABBREVIATIONS

ABBREVIATIONS	
AB	As-Built
AM	Additive Manufacturing
AR	As-Received
ASTM	American Society of Testing and Materials
BCC	Body-Centered Cubic
BD	Building Direction
BFTEM	Bright-Field Transmission Electron Microscopy
BSE	Backscattered Electron
CAD	Computer-Aided Design
DED	Directed Energy Deposition
DLD	Direct Laser Deposition
DLF	Directed Light Fabrication
DMLS	Direct Laser Metal Sintering
DSA	Dynamic Strain Aging
EBDM	Electron Beam Direct Manufacturing
EBM	Electron Beam Melting
EBSD	Electron Backscatter Diffraction
EDX	Energy Dispersive Spectroscopy
E-PBF	Electron Powder Bed Fusion
ESR	Electro Slag Remelting

EU	European Union
FCC	Face-Centered Cubic
Gen. IV	Generation IV
GFR	Gas-Cooled Fast Reactor
GIF	Generation IV International Forum
GMAW	Gas Metal Arc Welding
HAADF	High-Angle Annular Dark-Field
HCP	Hexagonal Close-Packed
HIP	Hot Isostatic Pressing
IEA	International Energy Agency
IN625	Inconel 625
IPF	Inverse Pole Figure
KAM	Kernel Average Misorientation
LAGB	Low-Angle Grain Boundaries
LBM	Laser Beam Melting
LENS	Laser Engineered Net Shaping
LFR	Lead-Cooled Fast Reactor
L-PBF	Laser Powder Bed Fusion
MA	Mechanical Alloying
MSR	Molten Salt Reactor
MUD	Multiple Uniform Density
ODS	Oxide Dispersion Strengthened

ODS-IN625	Oxide Dispersion Strengthened Inconel 625
OM	Optical Microscopy
PBF	Powder Bed Fusion
PLC	Portevin-Le Chatelier
RT	Room Temperature
SA	Solutionized and Aged
SCWR	Supercritical Water-Cooled Reactor
SE	Secondary Electron
SEM	Scanning Electron Microscopy
SFE	Stacking Fault Energy
SFR	Sodium-Cooled Fast Reactor
SLM	Selective Laser Melting
STD IN625	Standard Inconel 625
STEM	Scanning Transmission Electron Microscopy
TCP	Topologically Close-Packed
TEM	Transmission Electron Microscopy
TTT	Time-Temperature-Transformation
VED	Volumetric Energy Density
VHTR	Very High Temperature Reactor
VIM	Vacuum Induction Melting
WAAM	Wire Arch Additive Manufacturing
WEC	World Energy Council

CHAPTER 1

INTRODUCTION

With accelerated living standards worldwide, the conflicts on energy demand and production methods continue to rise. While natural resources are harmful for the environment and becomes limited in availability, the inclination to produce electricity using nuclear power has regained attention despite the ongoing debate on their potential risks. In the early 21st century, a new generation of nuclear power plants (i.e., Generation IV reactors) was proposed, and current research is focused on developing structural materials capable of withstanding their demanding conditions. Among the next-generation reactors, molten salt reactors (MSRs) come to the forefront due to their unique characteristics such as the fuel type, safety, sustainability and mobility. In MSRs, nuclear reactions take place within a molten salt medium, which can both be used as coolant and fuel. Fissile elements can be continuously dissolved into the molten salt and the mode of the reaction can be controlled by adjusting the composition of the molten salt, or the amount of the solute. In a case of emergency, the molten salt is immediately dumped into a freeze plug, offering an unmatched safety for this type of reactors. However, structural materials in MSRs experience very high temperatures around 700 °C, as well as a highly corrosive and irradiating environments. As a result, the number of structural materials licensed for MSR applications is scarce to fully incorporate them for commercial power production and numerous studies are being conducted to develop advanced materials to endure extreme condition they will be facing.

IN625 is a solid solution strengthened nickel-based superalloy, including up to eight different elements in its Ni matrix. Owing to their excellent mechanical behavior under hostile conditions such as high temperature and corrosion, it has a broad range of application areas, such as aerospace, chemical, marine and energy industries.

Along with the demanding conditions, the structural components for such industries have quite often an intricate shape, which extend their production lead time and limits the production methods. Additive manufacturing (AM), in this regard, offers significant convenience by reducing the lead times and enabling the production of intricate shapes. Several AM methods are commercially used to produce metal parts. Among them, L-PBF has attracted the most attention, due to its versatility, applicability and high amount of research gap to fully commercialize them. The number of studies on the L-PBF of nickel-based superalloys has increased exponentially, to fully understand and discover the ways to produce superalloys without sacrificing their mechanical properties. IN625 is one of the most studied material on L-PBF studies, due to their excellent mechanical properties, as well as their suitability for AM. Specifically, owing to the low amount of Al and Ti, IN625 a highly-weldable alloy, making them compatible with AM methods, where the powders are fused together by the application of high amounts of heat.

However, the heat cycles in L-PBF are very different compared to the conventional production methods. Specifically, the rapid cooling rates, reaching up to 10^6 K/s in L-PBF, results in a quenched-in state for the elements within IN625 which leads to distinct features. This process produces a unique structure with sub-micron dendrite arm spacing and often leads to the segregation of Nb and Mo. Additionally, a substantial amount of residual stress builds up during the L-PBF process, which necessitates the application of specific heat treatments to alleviate it.

Having high number of elements within the composition makes IN625 a highly complex alloy in terms of microstructure. In other words, IN625 is capable of forming several different phases, presence or absence of which strongly affects the mechanical properties. The majority of second-phase particles form after a certain type of exposure to heat. For example, primary and second carbides are usually found in the microstructure, the former precipitates during solidification, while the latter precipitates between a certain temperature ranges over time. The effect of the

carbides on the mechanical properties can vary. Due to their irregular shape and sizes, their presence is sometimes considered detrimental. However, grain boundary carbides suppress the grain growth during recrystallization and inhibit the grain boundary sliding and improve the creep properties. On the other hand, γ″, the strengthening phase, is formed between 650 and 900 °C. They are formed because of the high Nb content within the microstructure, with the stoichiometry of Ni_3Nb and ellipsoidal shape. Although their presence strengthens the alloy remarkably, γ″ is a metastable phase, which coarsens and transforms into metastable δ phase after extended heat exposure. δ phases are large and acicular in shape, and they are often considered as detrimental since they behave as crack initiation sites while depleting the solid-solution strengthening Nb within the microstructure. In some cases, however, the co-presence of the δ and γ″ phases are found to enhance the mechanical properties. The effect of the depletion of the solid-solution elements from the matrix is much more severe when topologically close-packed (TCP) phases form. The most common TCP phase seen in IN625 is Laves phase, having the A_2B stoichiometry with a very irregular shape, which significantly deteriorates the mechanical properties. Tailoring and achieving a desired combination of mechanical properties requires an extensive knowledge on the phase transformations and kinetics of IN625.

ODS is a strengthening method for advanced alloys to further enhance their mechanical properties, where thermally stable nano-oxides are inserted into the alloy's matrix. These nano-oxides hinder the dislocation motion and pin the grain boundaries, while remaining stable at very high temperatures. ODS is usually implemented by the addition of a certain amount of Y_2O_3 via conventional powder metallurgical methods, to form nano-sized and stoichiometric complex oxides. Mechanical alloying by ball milling puts alloy powders into a supersaturated position, where yttria is dissolved within the powder. However, this significantly distorts the shape of the alloy and decrease their flowability, making it inapplicable for L-PBF production. The size and number of nano-oxides depend on the secondary element combined with Y. For instance, Y-Al-O oxides are on the order of hundreds

of nm in size, while Y-Ti-O and Y-Hf-O oxides are much smaller in size and greater in number. External elemental powders may be added before L-PBF to facilitate nano-oxide formation and refine their size. A successful ODS for L-PBF necessitates satellite formations of nano-oxides on the alloy powder without compromising its sphericity, which is only achieved by means of mechanical mixing.

Studies on developing ODS superalloys by means of AM are still in its early stages and the number of publications is limited. As such, optimal production parameters for ODS superalloys via L-PBF have yet to be fully established. In order words, there is still a plenty of room for research to fully optimize and develop strategies for ODS and L-PFB to fully incorporate advanced materials for specific applications.

This work aims to develop a new class of ODS IN625, by adding and mixing 0.3 wt% Y_2O_3 and 0.4% Hf with IN625 to enhance its properties for use in harsh environments. Several different processing parameters were tested, followed by comprehensive investigations to optimize the benefits ODS can provide. A standard IN625 was also produced after following the same procedure, for a proper comparison. The presence of nano-oxides and their impact on the mechanical properties both at RT and 700 °C have been assessed quantitatively. Solutionizing and aging (SA) and direct aging (DA) heat treatments were applied to as-built (AB) alloys to observe the mechanical property changes. For SA condition, a conventionally rod has also been subjected to this heat-treatment for comparison. Consequently, superior mechanical properties have been obtained for ODS alloys, while ductility is increased.

This thesis consists of five chapters, starting with a brief information on the energy demand and the relation between IN625, L-PBF production and ODS. The introductory information has been extensively elaborated in the Chapter 2, following a top-down approach on superalloys, the common phases observed, production methods, strengthening mechanisms, IN625, ODS, and recent studies on ODS

IN625, with a comprehensive review of the latest literature. Chapter 3 details the experimental procedures used in this study, from starting materials to mechanical property assessments, including the optimization of mechanical mixing, L-PBF production, and heat treatments. In Chapter 4, the results of the study, which includes the effects of different parameters, the selection of optimal conditions, and the characterization of the alloys, are presented. Both quantitative and visual data are provided, with a more focus on the detailed characterization of the AB alloys. This thesis sheds a light on the improvement of the mechanical properties of the ODS alloys thoroughly, after concluding remarks and suggested future work in Chapter 5.

CHAPTER 2

LITERATURE REVIEW

2.1 Global Energy Demand and Nuclear Energy

The focus on energy conservation and consumption has become increasingly important in the 21st century [1]. The World Energy Council (WEC) anticipates the global energy demand to rise by 45 to 60% by 2060. In the European Union (EU) alone, the energy demand is estimated to increase by nearly 20% by 2030. The International Energy Agency (IEA) projects that the use of primary energy sources will grow to 334 million barrels per day in oil equivalent, which is 1.5 times more than in 2000 [2–5]. The rising living standards and economic growth trigger this energy demand, especially in developing countries. According to the Paris Climate Agreement, the rise in global temperature aimed to be kept under 2° C, and the energy demand contradicts the reduction of CO_2 emissions to alleviate global warming [6–8]. Carbon-based fuels (i.e., oil, coal and natural gas) still have the most outstanding share in fulfilling the global energy demand within the last decade, which is outlined in Fig. 2.1. This demand is expected to increase further with global economic growth, technological development, and societal progress. Moreover, the decline of fossil fuel reserves, as well as their negative environmental impact, highlights the need for cleaner energy alternatives. Currently, renewable energy sources (i.e., nuclear, solar, hydropower and wind) hold great promise for meeting future energy needs while reducing CO_2 emissions and mitigating the effects of climate change [6,8–10]. While renewables are crucial in shifting to low-carbon energy production, they are inadequate to meet rising energy demand.

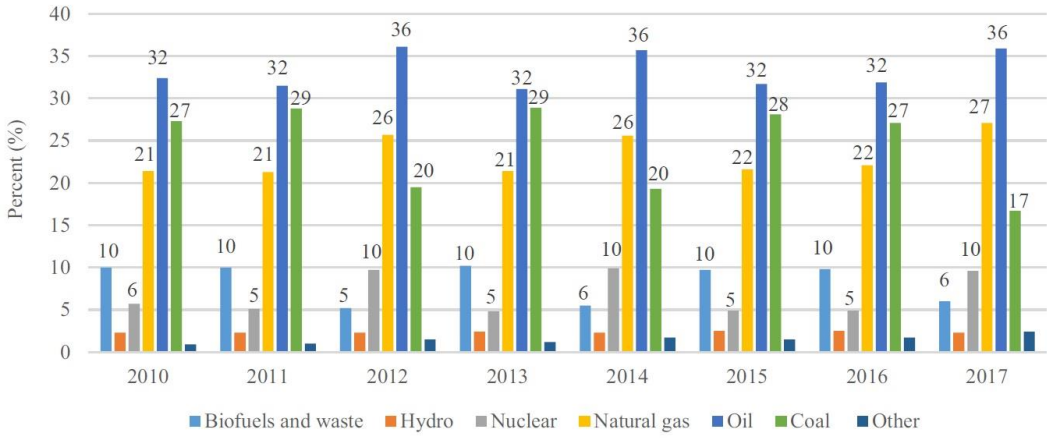

Figure 2.1 The global energy consumption shares between 2010 and 2017 (Adapted from [2]).

Nuclear energy, among other renewables, prevails as a vital alternative for future power generation, mainly because it does not emit CO_2, operates safely, and generates vast amounts of electricity from a single plant. In fact, nuclear energy comes after hydroelectric power as a source of clean electricity. Although there are ongoing debates regarding the risks of nuclear power in terms of nuclear accidents and radioactive waste management, nuclear energy is still considered one of the most viable options for meeting global energy demand and reducing reliance on fossil fuels [11–13]. A comparison of the products generated from electricity production through coal and nuclear reactions is illustrated in Fig. 2.2.

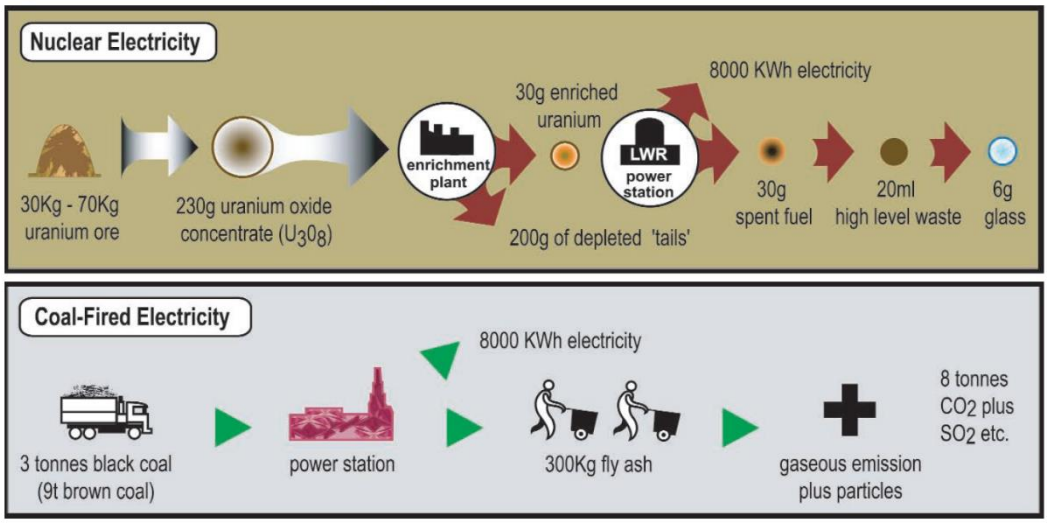

Figure 2.2 Waste comparison in nuclear and coal-based electricity production [14].

2.1.1 Overview of Nuclear Energy Generation

Nuclear energy simply utilizes the energy released from the nucleus of atoms, which can be produced via fission and fusion reactions. In fission reactions, the nucleus of a heavy, unstable atom is split into smaller parts by a chain reaction, where significant energy is released. In fusion reactions, conversely, combining the nuclei of two lighter atoms releases an even more substantial amount of energy. However, all of today's nuclear power plants are based on the nuclear fission of uranium and plutonium [15–17]. The implementation of nuclear energy began in the mid-20th century, with countries such as the United States, the United Kingdom, Russia, and France leading the commercialization of first-generation nuclear power plants. Significant advancements in nuclear energy technology occurred between 1970 and 1985 [13]. However, the global perspective on nuclear energy changed abruptly, after the well-known Chernobyl accident in 1986 [18]. After the incident, many countries have phased out nuclear energy development, and the number of nuclear power plants built has considerably dropped. Nevertheless, the development of nuclear energy has persisted despite the implementation of stricter safety policies by many nations and organizations. The peril of climate change, energy security

problems, and unstable fossil fuel prices compel many nations to reconsider nuclear energy as an option. Eventually, new roadmaps to handle both sides of this discrepancy have been set within the last decade. Currently, nuclear reactors in use are classified as generation II and III reactors. Research and development efforts, however, are focused on licensing generation IV (Gen. IV) nuclear reactors, which have all attributes of the former generation reactors [15,19–21].

2.1.2 Generation IV Nuclear Reactors

Gen. IV reactors are defined as advanced nuclear reactors of the following decades in which enhanced safety, efficiency and sustainability are provided. Also, important issues from previous generations, such as waste management and proliferation resistance, are intended to be minimized [22]. At the beginning of the 21st century, six different reactor technologies were introduced by the Generation IV International Forum (GIF), which are outlined in Table 2.1.

Table 2.1 Summary of Gen IV. Reactor Designs [21,22].

System	Neutron Spectrum	Coolant	Outlet Temperature	Fuel Cycle	Size (MW_e)
Very High Temperature Reactor (VHTR)	Thermal	Helium	Up to 1000	Open	250-300
Gas-Cooled Fast Reactor (GFR)	Fast	Helium	850	Closed	1200
Sodium-Cooled Fast Reactor (SFR)	Fast	Sodium	500-550	Closed	50-150 300-1500 600-1500
Lead-Cooled Fast Reactor (LFR)	Fast	Lead	480-570	Closed	20-180 300-1200 600-1000
Molten Salt Reactor (MSR)	Thermal or fast	Fluoride salts	700-800	Closed	1000
Supercritical Water-Cooled Reactor (SCWR)	Thermal or fast	Water	510-625	Open or closed	300-700 1000-1500

Among six Gen. IV nuclear reactors proposed, MSRs come to the forefront due to their unique attributes, such as unmatched safety, high thermal efficiency, and utilization of various fuel types.

2.1.3 Molten Salt Reactors

MSRs are reactors with a fast or thermal neutron spectrum that are cooled by means of molten salts with graphite as moderator. The fact that molten salts can also be used as fuels makes MSRs have distinct properties from the other Gen. IV reactors, where solid fuels are used. A eutectic mixture of fluorides of fissile elements (e.g., UF_4) and carrier salts (e.g., LiF – BeF_2) is prepared to form the fluid [23,24]. The heat is generated through the nuclear reactions in the reactor core and transferred to the heat exchanger by the fuel salt. While the fuel salt returns to the reactor core for further reactions, the heat in the heat exchanger is transferred by coolant salt to a steam or gas cycle to generate electricity [25]. A schematic illustration depicting the working principle of the MSR is illustrated Fig. 2.3.

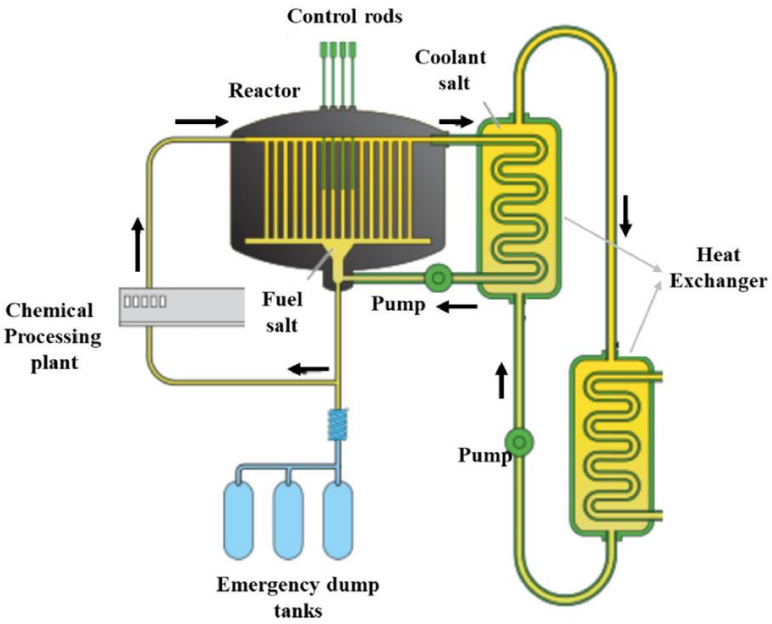

Figure 2.3 Schematic of MSR and its components [25].

Molten salts are considered highly promising in future nuclear applications, as they offer a safe, more efficient, and sustainable means of electricity generation. The most significant characteristics that make MSRs attractive are as follows;

- Among the other coolants used in conventional nuclear power plants, molten salts possess the greatest heat capacity which allows MSRs to be operated at atmospheric pressure.
- Molten salts have higher boiling points and low vapor pressures, which allows reactions to take place at higher temperatures and improves efficiency.
- Molten salts are chemically inert, and the possibility of a catastrophic failure due to a reaction with air and water is highly unlikely.
- Nuclear meltdown will not be the case since the fuel mixture is a molten fluid. Nevertheless, in any case of an accident, fuel is immediately drained to the emergency tanks to be frozen.
- Unlike conventional reactors, where the fuel is removed and processed separately, on-line fuel processing is possible in MSRs.

Despite all the novelties MSRs offer, it is important to note that the operating conditions of MSRs are extremely hostile. Specifically, service temperatures higher than 700 °C, along with the use of corrosive molten salts and excessive neutron irradiation, significantly limit the range of suitable materials [23,26–28]. Thus, the unavailability of the structural materials for specific components keeps MSRs from being officially licensed.

2.1.4 Material Requirements and Candidate Materials

The expected characteristics from Gen. IV reactors, including MSRs, are typically exceptional toughness at elevated temperatures, structural integrity against irradiation-induced defects (e.g., void swelling) and chemical compatibility with the coolant and fuel. In MSRs, the highly corrosive nature of molten salts becomes more severe at higher temperatures and with fission by-products [28–30]. This is demonstrated by a three-axis chart including the service temperature, irradiation

damage and corrosion susceptibility shown Fig. 2.4, where the working environments of present and future nuclear reactor types are compared.

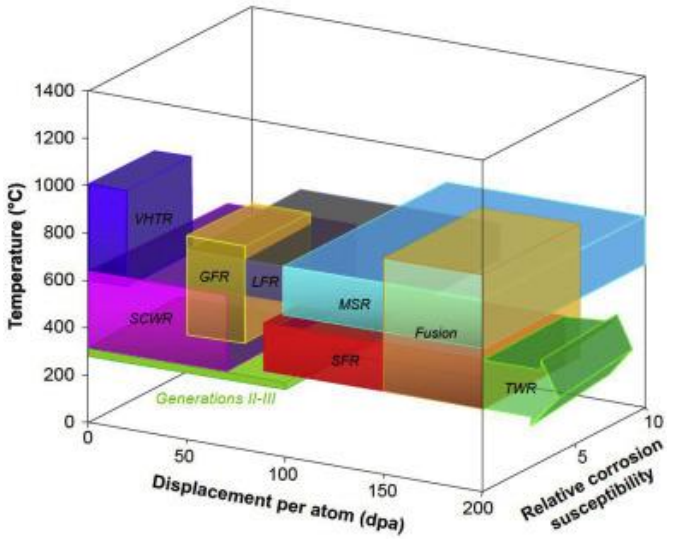

Figure 2.4 Operating conditions of several advanced nuclear reactors [29].

Common materials for corrosive environments (e.g., stainless steel) are not applicable in MSRs due to the high solubility of oxide layer-forming elements in molten salt [31]. To this end, studies are focused on altering the fluorine potential of molten salt by the addition of metallic elements [32]. Additionally, structural components are coated with metals insensitive to molten salt corrosion [33]. Another important issue for structural materials in MSRs is their susceptibility to high temperature He embrittlement at grain boundaries. The formation and growth of He bubbles at grain boundaries significantly reduce the material's creep strength and ductility. To mitigate this, the dispersion of fine particles and the formation of dislocations and twins were employed to capture He bubbles [29,34–36]. Ultimately, proposed and studied materials for MSR applications are nickel-based superalloys, graphite, ceramics and refractory alloys, owing to their ability to withstand harsh environments MSRs have [30]. Among these materials, nickel-based superalloys have been considered the most viable option due to their excellent intrinsic mechanical properties at elevated temperatures, as well as their corrosion and irradiation resistance.

2.2 Superalloys

Superalloys are a class of special types of alloys composed of many elements, mostly based upon Group VIIIB (i.e., Fe, Ni and Co). They are designed to maintain their mechanical properties under extreme conditions such as high temperatures, corrosive environments and high neutron flux. Under such conditions, the mechanical properties of typical titanium alloys and steel begin to deteriorate (i.e., after 540° C). However, superalloys are capable of retaining their integrity at service temperatures up to 1000 °C, making them ideal for numerous application areas, including aircraft components, gas turbines, and plant equipment for chemical, nuclear and marine industries [37–40]. Prominent mechanical properties of superalloys at elevated temperatures are superior strength, creep, wear, oxidation and erosion resistance, along with good surface stability [41]. Superalloys have a face-centered cubic (FCC) austenite matrix that contains several elements like chromium, and small additions of Al, Nb, Ta, Ti, Mo and W can be made to tailor the desired properties. Superalloys are mainly classified as nickel, iron-nickel and cobalt-based superalloys. Although pure iron and cobalt exhibit a body-centered cubic (BCC) and hexagonal close-packed (HCP) lattice structure, respectively, at low temperatures, they transform into FCC structure at high temperatures. Austenite stabilizers can also be added to these elements to retain the FCC structure at low temperatures. On the other hand, nickel has an FCC lattice structure up to its melting point [37,38,40,42]. Among others, nickel-based superalloys have been the main focus of studies due to their versatility, lower cost and various strengthening mechanisms [43,44]. The dominance of nickel-based superalloys is chronologically shown in Fig. 2.5.

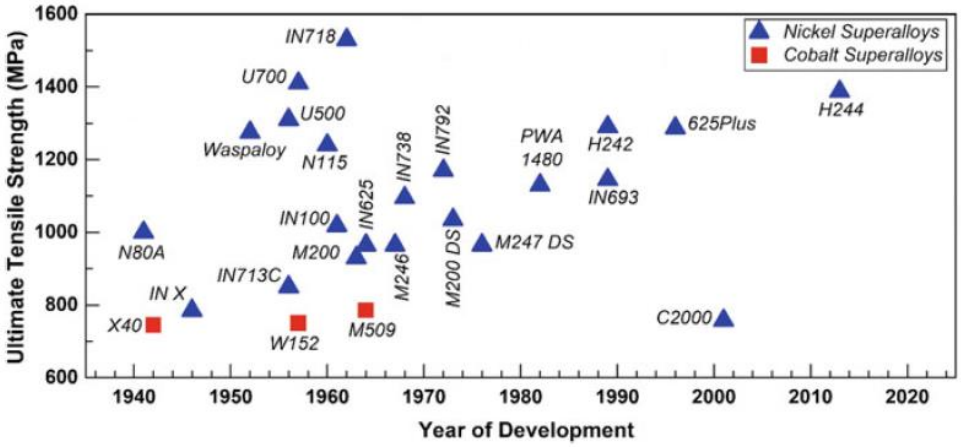

Figure 2.5 The timeline of superalloy development with respect to their UTS. (Adapted from [42]).

2.2.1 Nickel-Based Superalloys

Nickel-based superalloys are very complex alloy systems that usually contain around ten alloying elements, with nickel as the solute [45]. Due to their diverse compositions, nickel-base superalloys are capable of forming very intricate microstructures. Their excellent strength under harsh service conditions stems from at least one of the three strengthening mechanisms, namely, solid solution strengthening, precipitation hardening and carbide precipitation at grain boundaries [46].

2.2.2 Phases in Nickel-Based Superalloys

There are several different phases in nickel-base superalloys. The FCC γ matrix constitutes the majority of the microstructure, residing in the secondary phases [39]. The matrix is mainly composed of nickel, but there are significant amounts of solid-solution elements due to the extensive solubility of the γ phase. This also leads to the precipitation of strengthening intermetallic phases (i.e., γ′ and γ′′), carbides, borides, nitrides and topologically close-packed phases (TCP) [39,47].

Table 2.2 Alloying elements and their effects in nickel-base superalloys [48].

Element(s)	Effects
Ni	Constituting γ matrix, formation of γ′ and γ″ phases
Cr	Solid-solution strengthening, oxidation and sulphidation resistance
Co	Solid-solution strengthening, lowering stacking fault energy, increasing the solvus temperature of γ′ phase
Mo, Ta, W	Solid solution strengthening, carbide formation (e.g., MC, M_6C)
Ti	Formation of γ′ phase, MC-type carbides and nitrides
Al	Formation of γ′ phase, enhancing oxidation resistance
B and Zr	Improving creep strength, inhibiting η phase formation
Nb	Formation of γ″ phase and MC-type carbides
C	Formation of several carbides (e.g., MC, $M_{23}C_6$, M_6C and M_7C_3)

2.2.2.1 γ′ and γ″ Phases

The γ′ phase, the main strengthening phase in most superalloys, forms in the presence of aluminum and titanium and has the FCC (ordered $L1_2$) crystal structure with the formulas Ni_3Al and $Ni_3(Al,Ti)$, respectively [49]. γ′ phase is coherent with the γ matrix, assuming a spherical, cuboidal or plate-like shape, depending on the specific composition and heat treatment [47]. Due to their sound thermal stability, these precipitates provide a great deal of strength and creep resistance at higher temperatures. The γ″ phase is another strengthening phase seen in niobium-bearing nickel-base superalloys. It has the BCT (ordered $D0_{22}$) crystal structure with the formula Ni_3Nb and assumes a disk-shaped morphology [50,51]. γ″ disks are nanoscale, with a thickness of around 10 nm and a diameter of 50 nm [52]. Precipitation of γ′ and metastable γ″ phases occurs at higher temperatures. The strengthening effect of these two phases strongly depends on their distribution, size and volume fraction, determined by the specific heat treatment [53]. Prolonged exposure to elevated temperatures may cause the γ′ and γ″ phases to transform into η and δ phases, respectively. η phase has the HCP ($D0_{24}$) crystal structure with the

formula Ni_3Ti, while δ phase has an orthorhombic ($D0_a$) crystal structure with the formula Ni_3Nb [54]. The unstable and stable forms of these phases are also named geometrically close-packed (GCP) phases [55,56]. The η phase forms intergranularly in a cellular form or intragranularly in an acicular form when the titanium-to-aluminum ratio is high [49,54]. Similarly, when metastable γ″ precipitates coarsen, they transform into stable δ phases in a needle or platelet shape [57]. Both η and δ phases are usually considered detrimental to the mechanical properties due to the fact that they act as stress concentration sites [58]. Lattice structures of GCP phases with the location of the elements are shown Fig. 2.6.

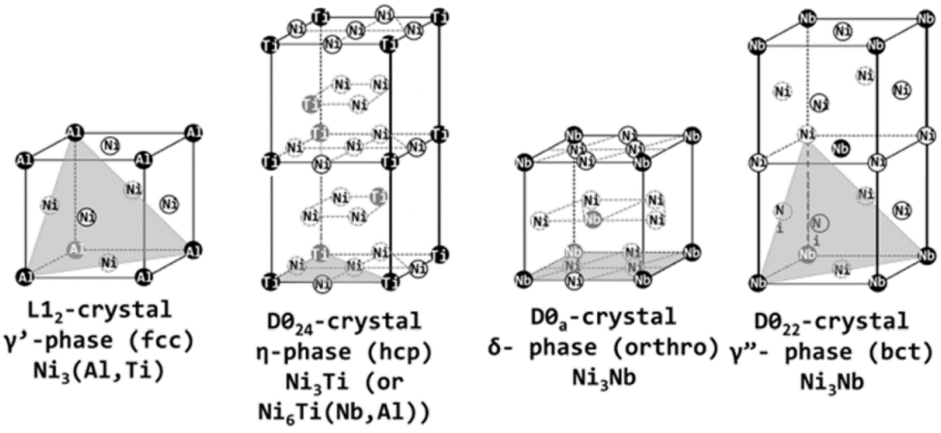

Figure 2.6 GCP phases in superalloys with their lattice structures [55].

2.2.2.2 Carbides

The elements within the composition of nickel-based superalloys have great affinity for carbon which is present up to 0.2 wt%. This leads to the formation of different types of carbide phases, such as MC, $M_{23}C_6$, M_6C and M_7C_3, in which the 'M' stands for metal atoms. Carbides are classified as primary and secondary carbides, according to their formation and stoichiometry. MC-type primary carbides form initially during solidification. They reside both at grain boundaries and within grains [51,59]. However, at elevated temperatures, the stability of MC-type carbides decreases, and they have a propensity for decomposing into secondary $M_{23}C_6$, M_6C

and M_7C_3 carbides at grain boundaries rich in chromium, molybdenum and tungsten [60]. $M_{23}C_6$ and M_7C_3 carbides are chromium-rich and are mostly found in chromium-bearing nickel-base superalloys. $M_{23}C_6$ carbides are the most common secondary carbides seen in superalloys [47]. Furthermore, M_7C_3 was also reported to transform into $M_{23}C_6$ at elevated temperatures [51]. On the other hand, M_6C carbides tend to form at greater temperatures than $M_{23}C_6$ carbides at the expense of heavy refractory metals such as tungsten, niobium and molybdenum [61]. Carbides can be both beneficial and detrimental to mechanical properties, depending on their location, dispersion, and shape. Owing to their irregular shape, carbides may act as crack initiation sites, deteriorating the strength and ductility. Conversely, carbides at grain boundaries hinder grain boundary sliding, thereby improving creep resistance [59,60,62,63].

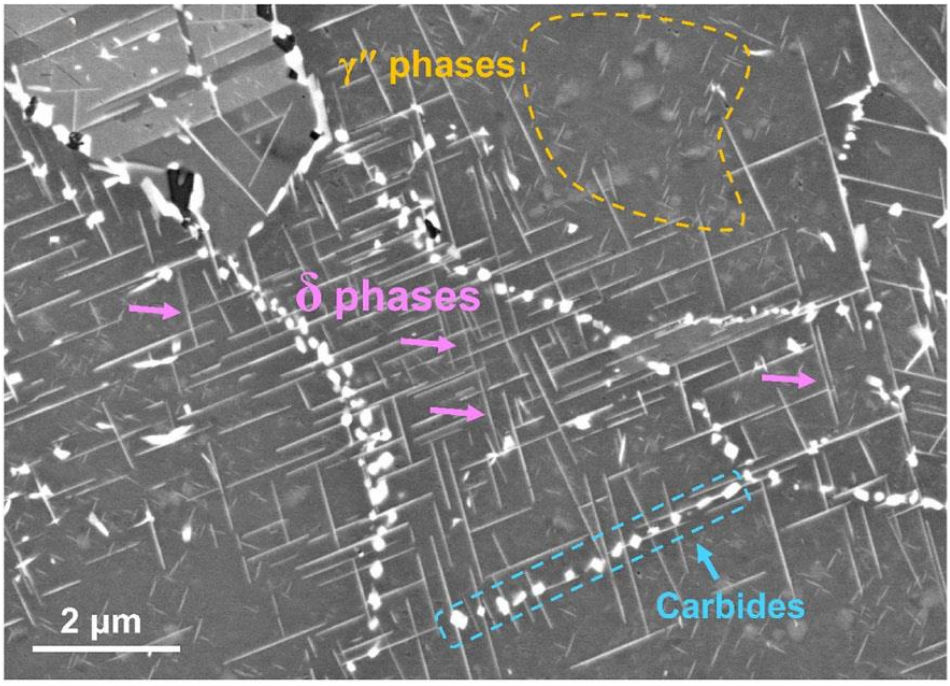

Figure 2.7 The presence of grain boundary carbides, δ and γ″ phases in Inconel 625 alloy, creep-deformed at 750 °C for 300 hours [64].

2.2.2.3 Topologically Close-Packed Phases

At elevated temperatures, nickel-base superalloys are prone to form detrimental TCP phases at the expense of refractory elements within the matrix. The name comes from their complex hexagonal-like crystal structure in which atoms are layered such that the coordination number reaches as high as 16 [48,65]. This arrangement results in a very low number of slip systems, making TCP phases very hard and brittle [66]. TCP phases deteriorate the mechanical properties of nickel-base superalloys by several mechanisms. Due to their acicular shape, they act as crack initiation sites during cyclic loading, and their brittle fracture facilitates crack propagation [67]. During formation, TCP phases consume strengthening elements from the matrix, reducing the solid solution strengthening effect. Common TCP phases seen in superalloys are Laves (A_2B), σ (A_xB_y) and μ ($A_{x'}B_{y'}$) where A denotes Fe, Ni or Co and B denotes Nb, Mo, Ta or Cr [47]. The morphology of the Laves phases with respect to primary carbides is demonstrated in Fig. 2.8. The σ and μ phases are not as commonly form as Laves phases. The σ phase, which nucleates on $M_{23}C_6$ precipitates, is structurally very similar to $M_{23}C_6$ carbides. Similarly, the μ phase is similar to M_6C carbides and forms when concentrations of molybdenum and tungsten are high [51]. Overall, knowledge and hindering the formation of TCP phases is essential to retain desired mechanical properties at elevated temperatures.

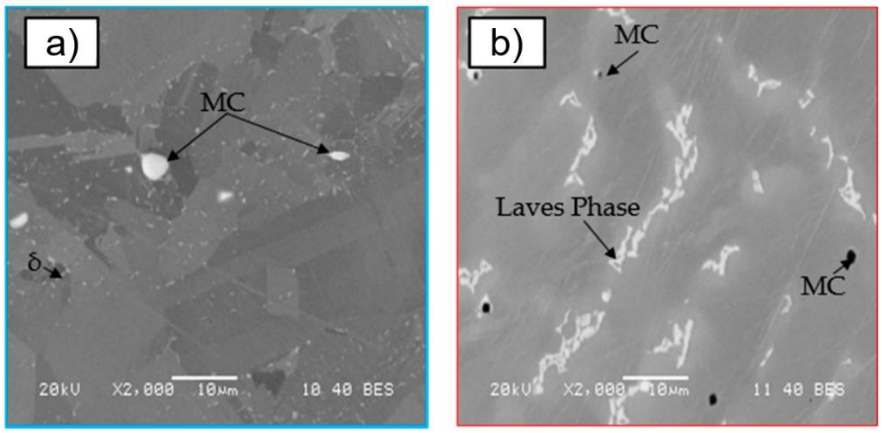

Figure 2.8 Intermetallic phases observed in a) wrought and b) additively manufactured Inconel 718 [68].

2.2.2.4 Borides and Nitrides

Boride and nitride phases can also be present in nickel-base superalloys. Boron and nitrogen tend to segregate to the grain boundaries and form various compounds. On the one hand, minor boron additions have been found to improve stress rupture properties and suppress the formation of TCP phases [49,51]. On the other hand, the presence of nitrides is considered deleterious to mechanical properties, as brittle and blocky nitrides like TiN and HfN form at grain boundaries [69]. Borides are also hard particles, typically observed in blocky or half-moon shapes [47]. Although borides and nitrides are found in superalloys, they are present in insignificant amounts compared to carbides. In summary, phases that can be observed in nickel-base superalloys are outlined in Table 2.3.

Table 2.3 Commonly observed phases in nickel-based superalloys, with their lattice structure and stoichiometry [47,49,70].

	Phase	Crystal System	Formula(s)
Solid Solution Matrix	γ	Cubic	Ni, Cr, Fe - Base
Geometrically Close-Packed Phases	γ′	Cubic	$Ni_3(Ti,Al)$
	γ″	Tetragonal	Ni_3Nb
	δ	Orthorhombic	Ni_3Nb
	η	Hexagonal	Ni_3Ti
Topologically Close-Packed Phases	σ	Tetragonal	FeCr, FeCrMo, CrFeMoNi
	μ	Rhombohedral	Co_2W_6, $(Fe,Co)_7(Mo,W)_6$
	Laves	Hexagonal	$Fe_2(Nb,Ti,Mo)$, $Co_2(Ta,Ti)$
Carbide Phases	MC	Cubic	TiC, NbC, HfC
	$M_{23}C_6$	Cubic	$(Cr,Fe,W,Mo)_{23}C_6$
	M_6C	Cubic	Fe_3Mo_3C, Fe_3Mo_3C, Fe_3Mo_3C, Fe_3Mo_3C,
	M_7C_3	Hexagonal	Cr_7C_3
Nitrides and Borides	MN	Cubic	TiN, (Ti,Nb,Zr)N
	M_3B_2	Tetragonal	Ta_3B_2, V_3B_2, Nb_3B_2

2.2.3 Strengthening Mechanisms

Principal strengthening mechanisms governing the mechanical properties of superalloys are solid solution strengthening, precipitation hardening and dispersion strengthening. Precipitation hardening involves thermally stable intermetallics that precipitate out at higher temperatures, while dispersion strengthening is provided by metallic carbide and oxide particles. These mechanisms work along with the intrinsic FCC structure, which has a high solubility for alloying elements, making the formation of strengthening phases possible. While grain size refinement and cold working can also contribute to strengthening, their effectiveness is limited at elevated temperatures. For instance, cold working only provides an increased strength up to around 540°C, and grain refinement is rarely employed for superalloys owing to the high-temperature environments they are designed for [71–73].

2.2.3.1 Solid Solution Strengthening

Solid solution strengthening in superalloys takes place due to the introduction of different alloying elements into the γ matrix. These elements distort the crystal lattice of the matrix because their atomic radii differ from that of nickel, thereby creating strain fields that impede dislocation motion [49,73,74]. This strengthening arises from two main mechanisms: atomic size misfit and elastic modulus misfit, where solute atoms of differing stiffness compared to the matrix create either hard or soft regions. The result is an increase in the strength compared to a pure Ni matrix [75]. Solid solution strengthening can lower stacking fault energy (SFE) in the crystal lattice, making it harder for dislocations to move and cross-slip. This mechanism becomes critical in preventing deformation at elevated temperatures. Lower SFE leads to dislocations dissociating into partials, forming hcp stacking fault ribbons, further restricting dislocation movement [71,76,77]. Certain solute elements, such as molybdenum, tungsten, chromium, and rhenium are prevalent in enhancing this hardening effect. Larger atomic size elements tend to reduce diffusion rates and

improve high-temperature performance but can also promote undesirable phases, such as TCP phases [49,65,78,79].

2.2.3.2 Precipitation Hardening

Precipitation hardening is considered one of the most effective techniques for altering the alloy's strength and ductility in balance. This mechanism mainly involves the interaction between precipitates and dislocations in which the movement of dislocations is hindered by the precipitates, leading to increased flow stress and moderate ductility [80]. Mechanisms pertaining to dislocation-particle interactions are determined according to the rigidity of the precipitate. Specifically, dislocations bypass hard precipitates by either Orowan looping or cross-slip without changing the particle. In contrast, soft precipitates are sheared by the dislocation (Fig. 2.9) [81]. In nickel-base superalloys, elements with low solubility in the γ matrix (e.g., Ti, Al, Nb) precipitate as intermetallic compounds, referred to as γ′ and γ″ phases. Impediment of dislocation motion by such particles is affected by various factors:

- Coherency strains between the matrix and precipitate due to lattice mismatch
- Antiphase boundary energy, which affects the difficulty of dislocation cutting
- Volume fraction and particle size of the precipitates [71,75,82]

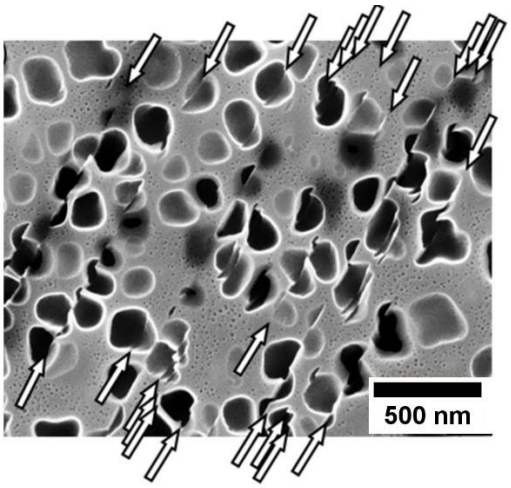

Figure 2.9 Sheared γ′ particles in a single crystal nickel-base superalloy [83].

2.2.3.3 Dispersion Strengthening

Dispersion strengthening in nickel-base superalloys is another way to enhance the mechanical properties. The mechanism is analogous to precipitation hardening, where second-phase particles effectively hinder the motion of dislocations. In this case, however, a strengthening component is added externally to form compounds rather than precipitating from the matrix at elevated temperatures. Moreover, because dispersed particles are usually hard and incoherent with the matrix, only Orowan looping contributes to strengthening. Dispersion strengthening is usually achieved through a special case called oxide dispersion strengthening, which will be reviewed in subsequent chapters. Also, creep properties can be enhanced by the formation of carbonitrides and secondary carbides at grain boundaries [71,84]. Interactions between dislocations and particles have been summarized in Fig. 2.10.

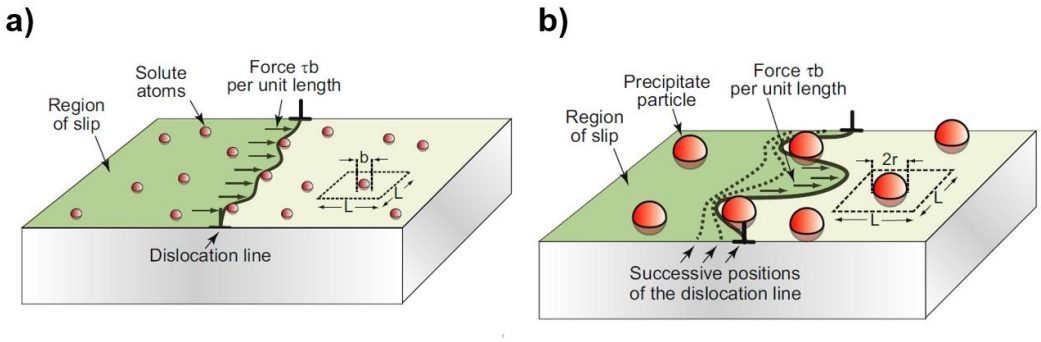

Figure 2.10 Dislocation-particle interactions in a) solid solution strengthening and b) dispersion and precipitation hardening (adapted from [74]).

2.3 Manufacturing Methods of Superalloys

2.3.1 Conventional Manufacturing of Superalloys

Conventional manufacturing of superalloys includes several standard processes, including remelting and casting, remelting and wrought processing, powder metallurgical consolidation and thermomechanical processing [85]. Ingots, then, are shaped into sheets, bars, tubes and other wrought products through thermomechanical processing [86]. Remelting the constituent elements by vacuum induction melting (VIM) to form ingots and castings is common. However, pouring the melt under vacuum conditions often results in intrinsic cavities and shrinkage in the ingots besides inclusions, which is why it is generally followed either by vacuum arc remelting or electro slag remelting (ESR) to mitigate these defects [42,87]. Nevertheless, micro and macro segregation takes place during the solidification of superalloys. The degree of segregation strongly depends on the composition of the alloy [88]. The use of superalloys for structural parts often requires intricate shapes, which are conventionally achieved through investment casting due to the difficulty of machining these materials. However, pores and structural instabilities may form in casting processes. To eliminate these issues, hot isostatic pressing (HIP) is applied to densify the castings and fill any pores, which results in an equiaxed structure [89,90]. Alternatively, powder metallurgy routes, usually followed by HIP, are

employed to produce components with more uniform microstructures and reduced porosity. The process chart of manufacturing methods of nickel-based superalloys is shown in Fig. 2.11.

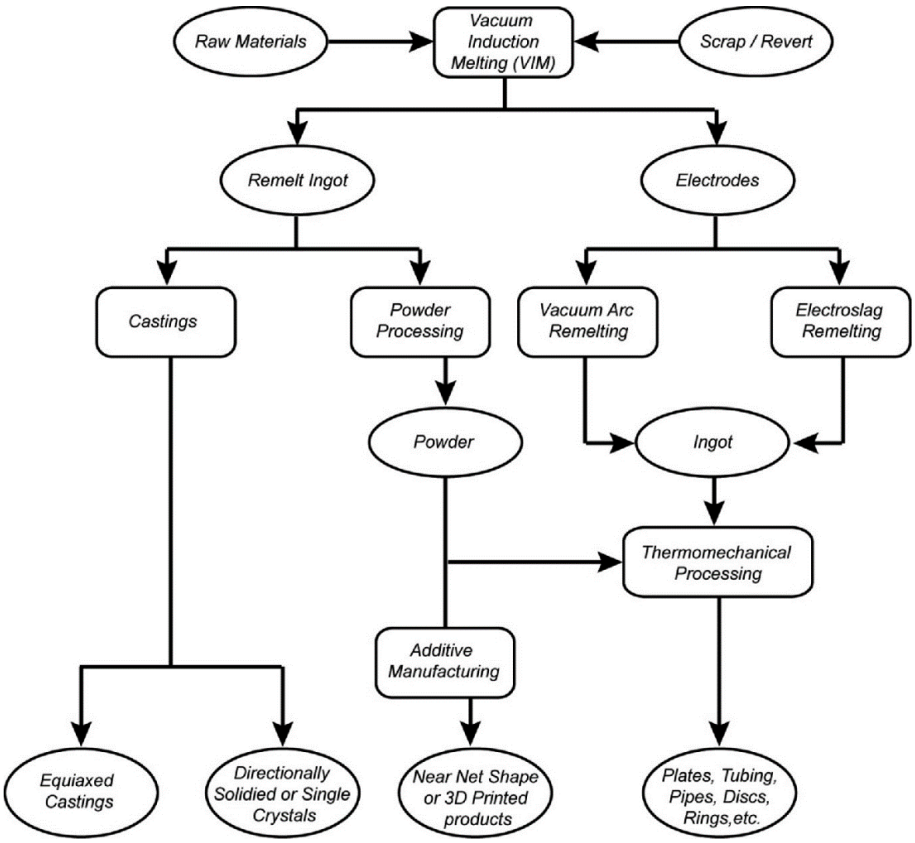

Figure 2.11 Flow chart depicting the manufacturing methods used to produce superalloy parts [42].

2.3.2 Additive Manufacturing of Superalloys

Additive manufacturing (AM) of metals is a novel process in which metal components are built layer by layer using computer-aided design (CAD) models [91,92]. Various metal-based AM techniques have been developed over the last decades. However, processes involving the rapid fusion and solidification of metals have been attracting the most interest over the decades, since they offer high flexibility in creating complex geometries, minimizing material waste and reducing lead times compared to conventional manufacturing methods. This is especially the

case for the nickel-base superalloys where traditional methods (e.g., casting and machining) are demanding, expensive and material-intensive. AM of nickel-base superalloys mostly utilizes powder or wire feedstock, which is fused by means of heat sources like lasers and electron beams. Specifically, studies within the last decade have been focused on methods such as laser powder bed fusion (L-PBF), electron beam melting (EBM) and directed energy deposition (DED) [55,92–95]. The progressive increase in research about powder bed fusion (PBF) AM of nickel-base superalloys can be seen in Fig. 2.12.

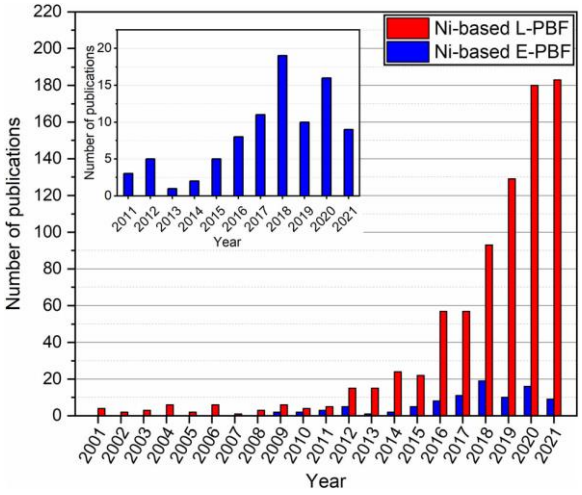

Figure 2.12 Number of publications through the last two decades on laser (L-PBF) and electron (E-PBF) powder bed fusion [94].

2.3.2.1 Laser Powder Bed Fusion

L-PBF is the most common metal AM technique in which a high-energy laser beam is used to melt metal powders in a powder bed. This process has other names such as selective laser melting (SLM), laser beam melting (LBM) and direct metal laser sintering (DMLS) [55,96]. A layer of metal powder on a substrate or on a previous layer is selectively melted and solidified according to the 2D layer profile of the part. The building platform is lowered according to the layer thickness and a new layer of powder is provided by a re-coater. This cycle continues until the desired shape is obtained. During the process, the building chamber is filled with an inert gas to

prevent any contamination [95,97]. L-PBF is governed by complex heat transfer and fluid flow dynamics, where rapid solidification occurs with cooling rates reaching up to 10^6 K/s. Four important factors determine how the laser beam interacts with metal powder: laser power (P), scan speed (v), layer thickness (t) and hatch distance (h). The shape, microstructure and mechanical properties of the finished product are significantly influenced by these factors. Although each parameter plays a different role, they are often combined into a single term known as volumetric energy density (VED) for a more thorough understanding [98].

$$\text{Volumetric Energy Density (J/mm}^3) \rightarrow \frac{\mathbf{P}\ (\text{J/s})}{\mathbf{V}\ (\text{mm/s}) \times \mathbf{h}\ (\text{mm}) \times \mathbf{t}\ (\text{mm})} \quad \text{(Eq. 2.1)}$$

As mentioned above, the metal powder in front of the molten pool is continuously melted and then solidifies almost instantaneously as the laser moves away. The large thermal gradients present during solidification induce convection which leads to the formation of localized melt pools, a common feature in L-PBF [99–102]. The shape and depth of the melt pool are determined by the scan speed. Faster scan speeds result in narrow and deeper melt pools while shallow and wider melt pools form at slower speeds. Improper control of the melt pool leads to defects such as gas pores and keyhole porosity. Therefore, careful analysis is performed especially in parameter studies [103,104]. A comprehensive schematic of the L-PBF process, including the key parameters and melt pool formation, is illustrated in Fig. 2.13.

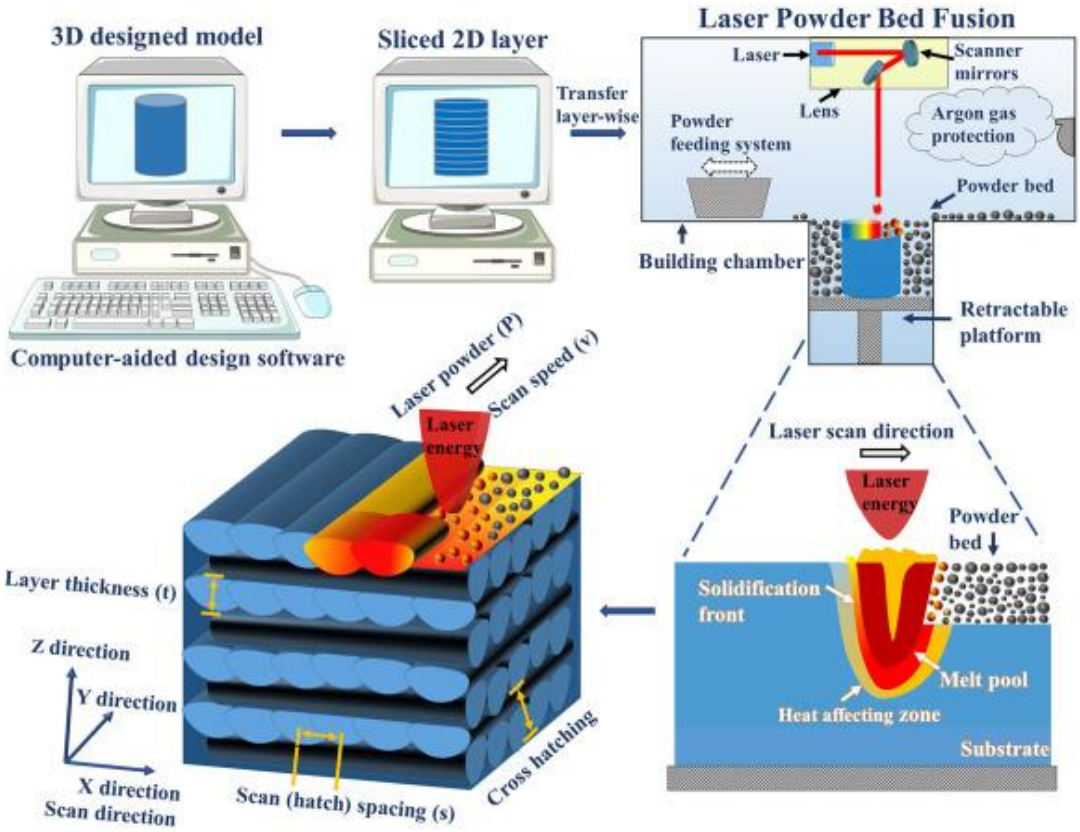

Figure 2.13 Schematic diagram depicting the stages in L-PFB [100].

2.3.2.2 Electron Beam Melting

EBM is another PBF method that uses a high-energy electron beam as the energy source to melt and fuse metal powders. This process is very similar to L-PBF in terms of operation which is why EBM is also referred to as E-PBF in literature. In both processes, near-net shape products having near full density can be produced [55,95,97,105]. In Fig. 2.14, the EBM process and its components are shown.

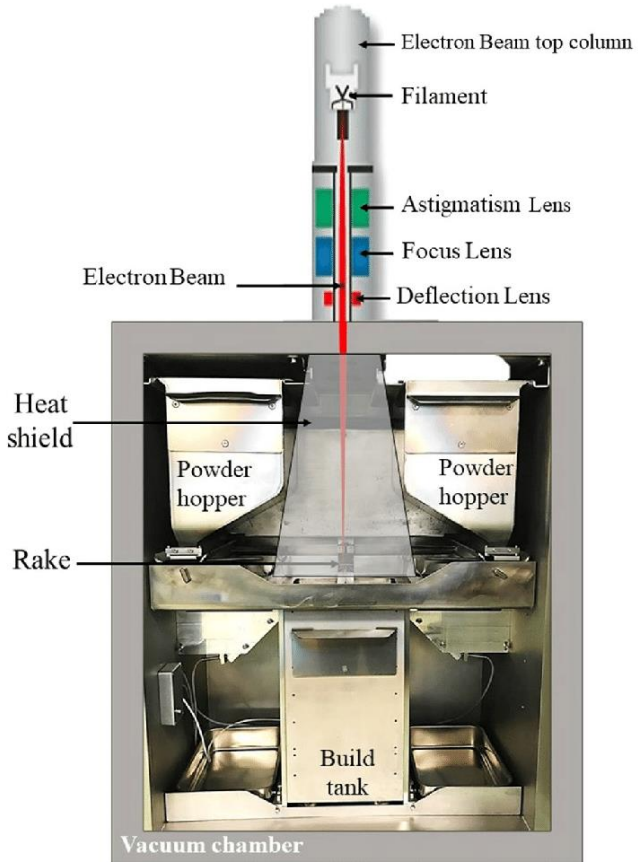

Figure 2.14 Schematic representation of the EBM process [106].

Although EBM shares operational similarities with L-PBF, it has remarkable differences in processing conditions, which makes EBM difficult to employ in metal AM studies (Fig. 2.12). One key difference is that EBM is performed under a vacuum environment, which limits the size of the build chamber and affects dimensional control [94]. Additionally, accelerated electrons have enough momentum to spatter powders during the process. Therefore, the powder size is larger in EBM than that of L-PBF. Another important factor is that in EBM, powders should be preheated to very high temperatures in EBM (up to 0.8 T_m) to facilitate fusion during scanning. High temperature preheating also leads to longer cooling times, which results in the formation of undesired phases, defects and inclusions, and makes superalloys more susceptible to cracking after the process [94,97,107,108]. Overall, process optimization is quite challenging in EBM, and it is not always applicable to all types of superalloys [109,110].

2.3.2.3 Directed Energy Deposition

DED is an AM method where either powder or wire feedstock is melted as they are being deposited. Unlike PBF techniques, in the powder form of DED, the feedstock is delivered from a multi-axis nozzle directly into a molten metal pool. This process utilizes different kinds of energy sources such as lasers, electrons and plasma arcs, to create the concentrated heat necessary to melt the feedstock. Therefore, several other names, such as laser engineered net shaping (LENS), directed light fabrication (DLF), electron beam direct manufacturing (EBDM), direct laser deposition (DLD) and wire arc additive manufacturing (WAAM), are associated with DED [55,111]. All processes are usually carried out with a shield of inert gas to prevent any kind of contamination [112]. Like other AM methods, parts are built layer-by-layer, and the nozzle moves up after a layer is deposited [113].

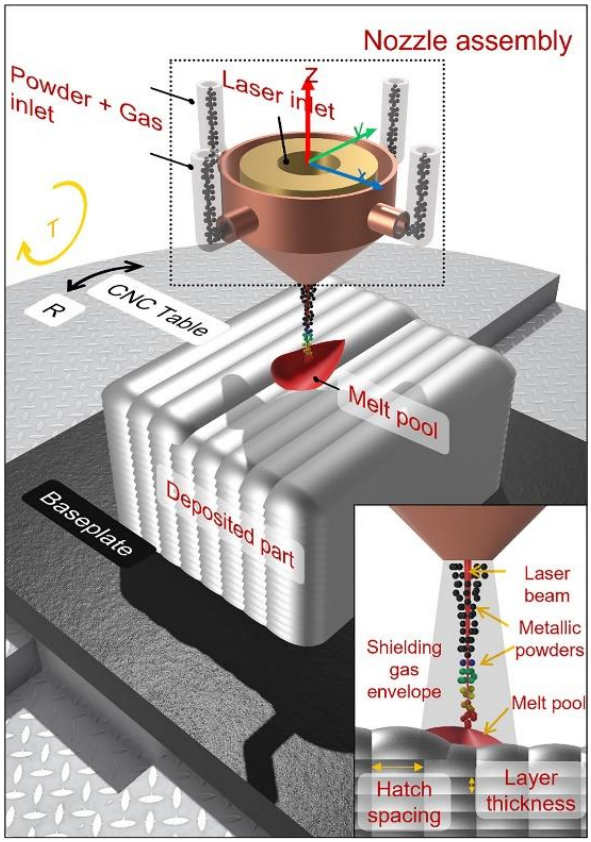

Figure 2.15 Schematic representation of the DED process [114].

Laser power, scan speed, laser beam spot size and powder feed rate are prominent parameters in DED that influence the process outcomes. A unique microstructure can be obtained based on the specific combination of these parameters. Parameter optimization by using a process window is essential in DED, as with PBF techniques, to control deposition and produce high-quality parts. In the as-built (AB) state, superalloys typically show a columnar dendritic microstructure with either planar or equiaxed grains. Due to the non-equilibrium cooling process and high-temperature gradients, columnar grains usually have a strong texture along the building direction (BD). Besides, the weldability of the superalloy is a critical parameter for a proper application in DED studies [55,114–117]. Generally, aluminum and titanium content primarily govern the weldability of the alloy, as susceptibility to crack formation increases with the amount of γ′ precipitates at high temperatures. The plot of weldability of some superalloys according to their aluminum and titanium content is demonstrated in Fig. 2.16 [97,106,110].

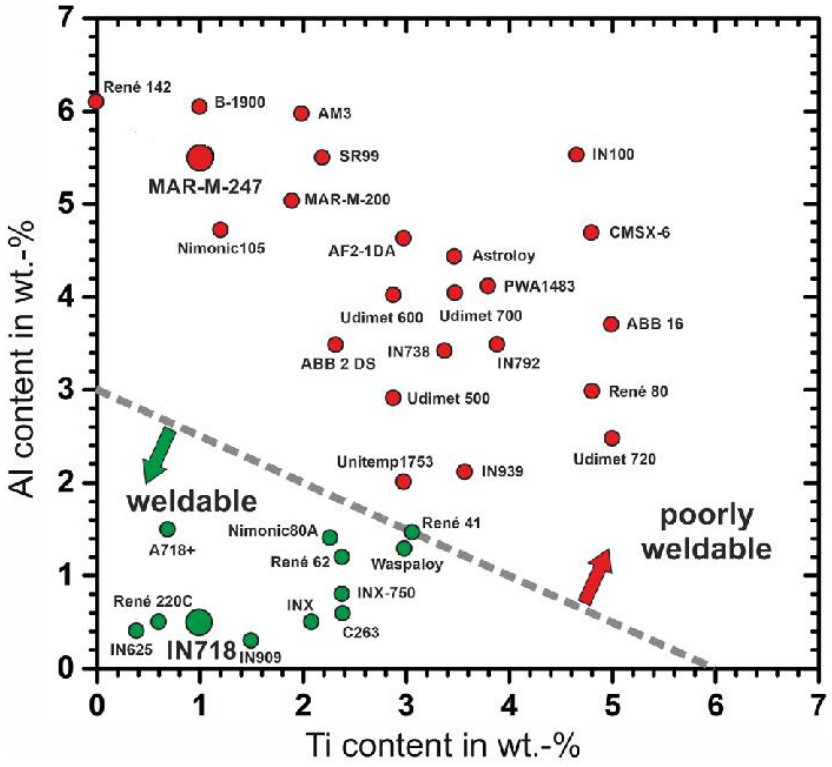

Figure 2.16 Weldability assessment diagram for superalloys (adapted from [106]).

The number of studies on the DED of superalloys is comparable to those on EBM. The outcomes demonstrated on DED for several superalloys in the literature are diverse. Nevertheless, DED has been successfully implemented for specific applications and shows significant potential in developing graded materials [115]. The main characteristics of L-PBF, EBM and DED are summarized in Table 2.4.

Table 2.4 Main features of three common AM methods for superalloys [97].

	L-PBF	**EBM**	**DED**
Heat Source	Laser beam	Electron beam	Laser beam
Key Parameters	Laser power Scan speed Hatch spacing Layer thickness Scan strategy	Beam power Scan speed Hatch spacing Layer thickness Pre-heat temperature	Scan speed Hatch spacing Layer thickness Powder feed rate
Power (W)	50-1000	500-3000	1000-3000
Scan speed (mm/s)	10-1000	10-8000	6-60
Spot size (mm)	0.04-0.5	0.1-2	1-3
Powder size (μm)	15-53	50-120	53-105
Surface roughness (μm)	7-30	20-50	15-60
Melt-pool size (μm)	~100	~100	~500
Cooling rate (K/s)	10^5-10^7	10^3-10^5	10^2-10^4
Temp. gradient (K/s)	10^6-10^7	10^5-10^6	10^5-10^7
Environment	Inert gas	Vacuum	Air/inert gas

2.3.3 Challenges in the Additive Manufacturing of Superalloys

Although the advent of AM has revolutionized the production of advanced materials with intricate shapes, the technology still faces practical and technical challenges that must be taken into consideration for AM to reach its full potential. The key

challenges in the AM industry can be classified as defect formation (i.e., porosity and cracking), residual stresses and anisotropy in the final product. Poor surface finish and unwanted inclusions in the microstructure often necessitate post-processing, especially for superalloys. Very high cooling rates in AM processes lead to remarkable residual stresses, which affect the final shape and cause anisotropy in mechanical properties. Specifically, residual stresses result in warpage, cracking and substandard mechanical properties, when parameters are not optimally selected. Stress relief treatments are typically implemented in AB parts to alleviate residual stresses. Pores and rough surfaces, which act as stress concentrating sites, are formed during the processes. Due to the nature of heat loss during melting and solidification, grains tend to grow epitaxially. This leads to a strong texture along the BD which reinforces the anisotropy. Within the context of superalloys, undesired secondary phases such as Laves, are found in AB parts. In γ″-strengthened alloys, it has been found that the formation kinetics of the deleterious δ phase significantly accelerated in additively manufactured parts compared to the wrought components, in which the δ forms after tens of hours of thermal exposure. Literature on mitigating these factors has been growing. Despite this growth, global standards and certifications on AM of superalloys have yet to be established. Furthermore, parameter optimizations are still performed in the studies to have a complete understanding of the underlying mechanisms [110,118,119].

2.4 Inconel 625

Inconel 625 (hereafter referred to as IN625) is one of the most common nickel-base superalloys in use. In industry and literature, it is also denoted as Alloy 625. IN625 is essentially a solid solution strengthened superalloy by virtue of various refractory elements such as Cr, Mo and Nb. However, it is also capable of forming strengthening intermetallics such as γ″ and carbides by applying suitable heat treatments [120–122]. This enables IN625 to achieve an optimal combination of yield strength, fatigue resistance, as well as oxidation, corrosion and wear resistance

under harsh environments. Moreover, it has excellent weldability, making it widely used in crucial parts of aerospace, chemical, nuclear and marine components [123]. The composition of IN625, as per the standard ASTM-B443, is listed in Table 2.5.

Table 2.5 The chemical composition of IN625 (in wt%) [124].

Element	Ni	Cr	Fe	Mo	Nb+Ta	C	Mn	Si	Al	Ti
Amount	58.0 min.	20.0-23.0	5.0 max	8.0-10.0	3.15-4.15	0.10 max	0.50 max	0.50 max	0.40 max	0.40 max

2.4.1 Phases and Heat Treatments

As briefly mentioned above, IN625 forms several phases at elevated temperatures. Between 650 and 950 °C, γ″ and δ phases, as well as MC, M_6C and $M_{23}C_6$-type carbides and Laves phases, are found in the microstructure. Additionally, $Ni_2(Cr,Mo)$ phases can be observed in IN625 after long thermal exposures less than 600 °C. The $Ni_2(Cr,Mo)$ phase has a Pt_2Mo-type lattice structure (body-centered orthorhombic) mostly seen in Ni-Cr-Mo base alloys. The inferior mechanical properties of IN625 under prolonged thermal exposure have been attributed to the presence of this phase [123,125]. The thermal stability of this phase varies depending on the molybdenum and chromium content, as well as the presence of additive elements [126]. However, $Ni_2(Cr,Mo)$ phase in IN625 is observed to become unstable at temperatures above 600 °C [127]. It has rather ellipsoidal or snowflake morphology [51].

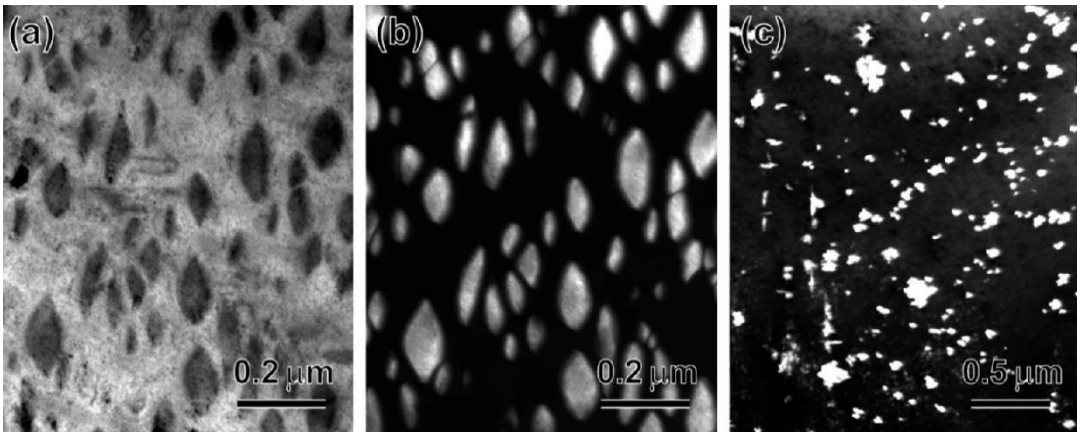

Figure 2.17 (a) Bright field and (b) dark field TEM images of $Ni_2(Cr,Mo)$ phase with ellipsoidal morphology and (c) snowflake morphology [51].

2.4.2 Heat Treatments and Mechanical Properties

Numerous studies to date have shown that the mechanical properties of IN625 depend significantly on the type, size, distribution and orientation of the secondary phases. Thus, the application and duration of thermal processes, as well as phase transformations, are crucial for achieving desired properties in specific applications. In IN625, the control of microstructure is generally implemented by solutionizing and age hardening heat treatments. The former refers to heating the alloy to temperatures below the incipient melting temperature to dissolve secondary particles into the matrix, followed by rapid quenching to retain the dissolved elements within the matrix. The latter is employed to facilitate the precipitation of strengthening phases and to control the carbide phases at moderate temperatures [86,128–130]. Additionally, stress relief annealing to reduce residual stresses and HIP to reduce porosity and homogenization are employed in AM IN625 [131]. Solutionizing treatment for wrought IN625 is recommended at 1150°C for 2 hours, followed by rapid quenching [132]. However, phase control becomes more complicated at moderate temperatures (i.e., between 600 and 800 °C). Therefore, the utilization of the time-temperature-transformation (TTT) diagram for IN625 is essential to design

a successful heat treatment strategy. The TTT diagram for IN625, including $Ni_2(Cr, Mo)$ phases, is shown in Fig. 2.18.

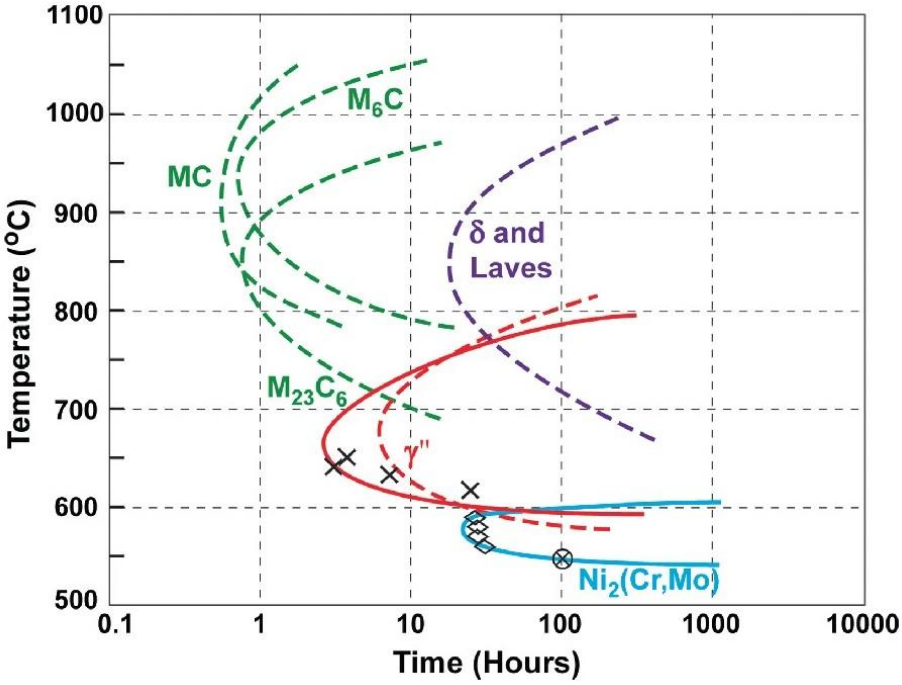

Figure 2.18 TTT diagram of IN625 (adapted from [51]).

There are several studies on the heat treatment of IN625 that investigate different procedures and detail specific outcomes. Hu et al., for example, applied different heat treatments around solutionizing temperature to investigate the change in the microstructure and mechanical properties with respect to the amount of Laves phases in laser solid formed IN625 [133]. Wang et al. found solutionizing on gas metal arc welded (GMAW) IN625 at 1140 °C resulted in removing all Laves phases in the as-weld sample, while two-step age hardening yielded MC-type carbides and γ″ phases in the microstructure [134]. Similarly, Hu et al. report that solutionizing DED IN625 at 1200°C for 30 minutes removed all Laves phases in as-deposited samples, while subsequent age hardening provided the greatest strength at the expense of ductility [135]. However, Safarzade et al. argued that solutionizing GMAW IN625 does not improve mechanical properties, and in fact, ductility deteriorated [136]. About age hardening, variables and results are rather dispersed. Donachie claims that direct

aging of wrought samples may result in a more uniform distribution of γ″ particles compared to traditional two-step aging processes [82]. This case has indeed been confirmed by recent studies. Marchese et al. found that direct aging on L-PBF IN625 at 700 °C resulted in the greatest strength compared to other heat treatment techniques [137]. Similarly, it has been found in another work that direct aging at 700 °C yields better mechanical properties than 900 °C and 1050 °C [138]. In these studies, an improvement in strength has been attributed to the γ″ and $M_{23}C_6$-type carbides [137,138]. Liu [64] followed a different approach, called short-term stress-aging treatment, to achieve an improved balance of strength and ductility which is attributed to the formation of nano-scale δ phases.

2.4.3 The Microstructure of Additively Manufactured Inconel 625

Unique microstructure characteristics are achieved in AM IN625, since they experience various and different thermal histories, along with the complex elemental composition of the alloy. In all AM processes involving IN625, melt pools containing dendritic and cellular structures are formed depending on the process parameters [139]. In PBF-based methods, smaller track sizes, melt pools and cellular structures are achieved compared to DED, due to the use of finer laser beams and thinner layer thicknesses. This results in superior mechanical properties in AB L-PBF parts [140,141]. Microstructures of the AB L-PBF and DED IN625 are demonstrated in Fig. 2.19.

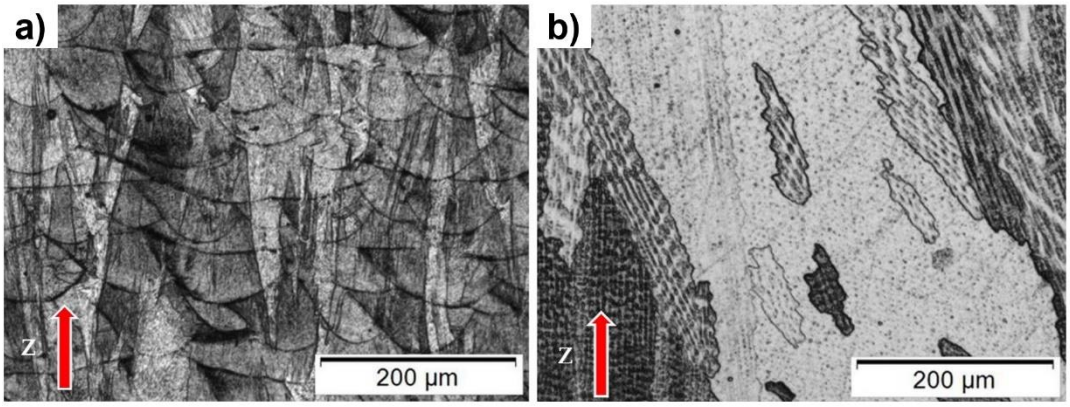

Figure 2.19 Microstructures of a) L-PBF and b) DED IN625 in AB condition (adapted from [131]).

As discussed in section 2.3.3, due to the rapid cooling rates and high thermal gradients, a strong texture with columnar grains along the BD is generally obtained in AM parts, which results in anisotropic characteristics. Specifically, γ grains with a <100> orientation tend to undergo epitaxial columnar growth during solidification in both PBF and DED. Despite this anisotropy, the mechanical properties of AB parts have exceeded the wrought and as-cast counterparts [114,135,142]. Moreover, solid solution elements such as Nb and Mo remain in a quenched state and segregate into interdendritic regions along with the buildup of high residual stresses [99,139]. In this regard, recent studies demonstrated that precipitation of the δ phase in AM IN625 takes place much faster than that of the wrought product [143–145]. Similar accelerated precipitation kinetics have also been observed in IN625 weldments [146]. As a result, the TTT diagram for conventionally produced IN625 (Fig. 2.18) may be misleading in terms of γ″ and δ transformations and determining a heat treatment route. To this end, Stoudt et al. [147] restructured the TTT curve to better represent the formation of the 1% volume fraction δ phase with respect to the curve of wrought IN625. This phenomenon is also investigated with computational simulations and it is confirmed that segregation of Nb and Mo segregations in the AB states accelerate the precipitation of γ″, δ and MC-type carbides [148].

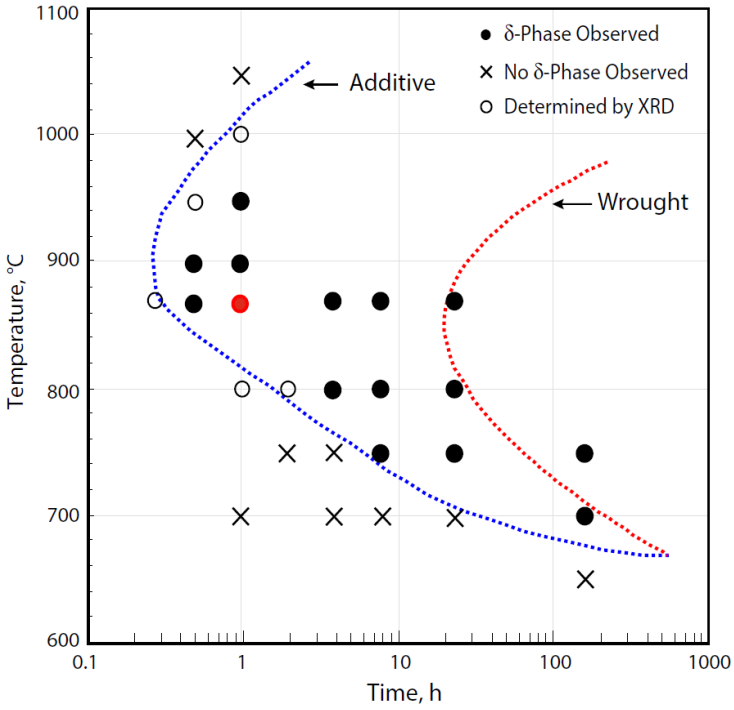

Figure 2.20 The TTT diagram depicting the formation curves of AM IN625 and wrought alloy [147].

2.5 Oxide Dispersion Strengthening

At temperatures above 700°C, the strengthening phases in IN625 tend to coarsen or dissolve into the matrix, which limits their effectiveness in hostile environments. ODS holds significant potential for maintaining the stability of these phases and further enhancing the material′s properties for high-temperature applications, as well as improving its corrosion and radiation resistance.

2.5.1 Oxide Dispersion Strengthening Principles

ODS is a method where insoluble ceramic oxides and/or oxide formers are inserted into the alloy. The strengthening effect is obtained by the high-density dispersion of nano-oxides within the metallic matrix. It essentially works in a similar way as precipitation hardening. However, nano-oxides do not precipitate from the

supersaturated matrix and are usually incoherent with the matrix [71,149]. In all ODS applications, Y_2O_3 (i.e., yttria) in varying amounts are added to the composition. Yttria, then, reacts with the specific elements at higher temperatures to form nano-size oxides. In the case of stainless steel and nickel-base superalloys, yttria usually reacts with aluminum and titanium to form Y-Ti-O and Y-Al-O oxides [150,151]. The nano-oxides effectively pin the dislocations and grain boundaries, thereby impeding the dislocation motion and stabilizing the grain boundaries during recrystallization. Specifically, dislocation motion is hindered through Orowan and Hall-Petch mechanisms, and grain growth is suppressed by Zener pinning [152,153]. Moreover, the nano oxides enhance radiation resistance by acting as sinks for vacancies and helium atoms, thereby hindering irradiation-induced void swelling. Nano-oxides within the matrix are known to remain thermally stable up to 1100°C, and they also maintain stability under both neutron and ion irradiation at temperatures exceeding 300°C [154–158].

2.5.2 Production Methods

The production of ODS alloys is not a straightforward process. Firstly, liquid-phase methods, such as casting, are unsuitable for ODS alloy production because the density of the nano-oxides is lower than that of the base alloy, causing them to float in the melt and leading to inevitable agglomeration [151,159]. Conventional ODS alloy preparation involves multiple stages of powder metallurgy, including mechanical alloying (MA), canning, HIP, and hot extrusion. Depending on the application, these processes are often followed by further sintering or heat treatment [160–162]. MA is a solid-state powder metallurgy technique in which powders undergo repeated deformation by mechanical forces. This is obtained by the interaction of powders with grinding balls in a process called ball milling. During the process, metal powders are mixed, fractured and cold welded with nano-oxides. Usually, hard vials and grinding balls such as WC, hardened steels and tool steels are used in ball milling. A uniform distribution of oxides is obtained when the metal

powders and nano-oxides are sufficiently interacted under either an inert or reducing atmosphere [163–166]. However, ball milling involves several process parameters that must be controlled which makes the production and development of ODS alloys a very demanding process from MA to end-use [167,168]. AM, in this regard, offers a faster route for fabricating ODS components with intricate geometries and reduced material waste (Fig. 2.21). The rapid melting and solidification in AM processes are also beneficial in retaining the nano-oxides [151,161,169,170]. L-PBF and DED are the most studied AM techniques in developing ODS alloys. Nevertheless, it is important to account for the fact that most powders lose their shape due to plastic deformation during milling, as irregularly shaped powders are unsuitable for AM processes. Conserving the sphericity while equally distributing the nano-oxides is required to have a fully dense structure without any defect, and process parameters should be designed accordingly [171–174].

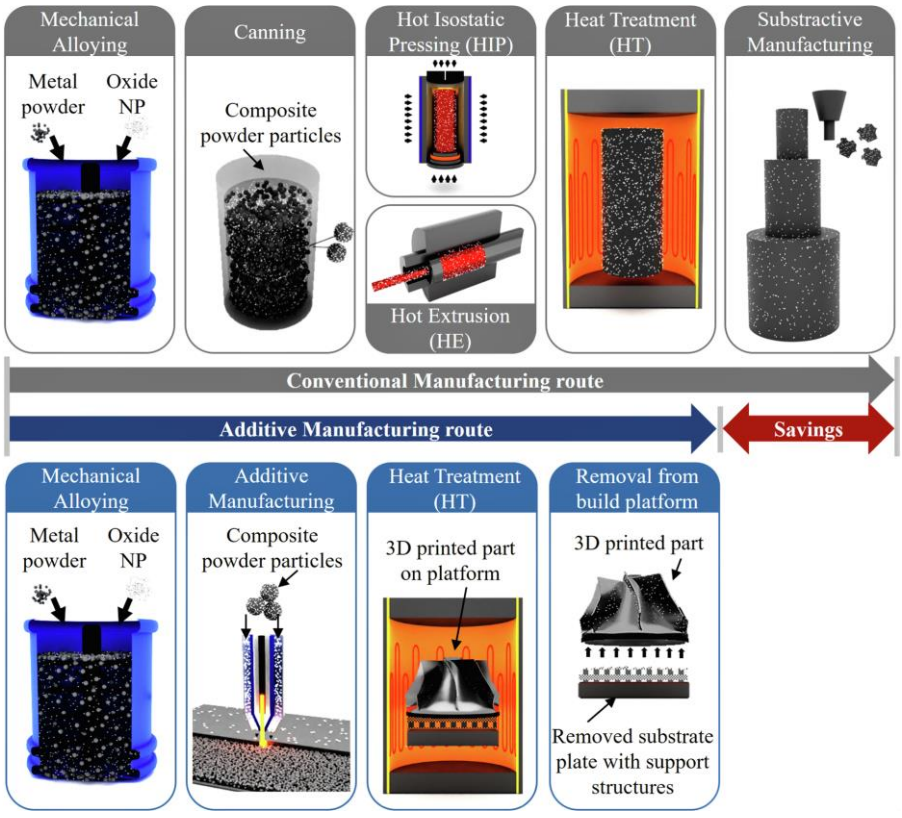

Figure 2.21 Flow charts comparing the steps of conventional production of ODS alloys and AM [161].

2.5.3 Nano-Oxide Systems

The strengthening in ODS alloys strongly depends on the size, number density and distribution of the nano-oxides. In this regard, complex Y-Al-O oxides are found to be coarser than other oxide systems, and they have a propensity for coarsening during subsequent processes [175,176]. Recent studies demonstrate that adding oxide-forming elements can refine the oxides. For instance, the preferential formation of Y-Ti-O oxides by the addition of Ti in a nickel matrix has led to finer oxides and increased mechanical properties, with an increased number density of nano-oxides [150]. Dou et al. reported that a 0.03 wt.% increment of titanium in aluminum containing ODS steel raised the Y-Ti-O oxides by almost 30% [177]. Lu et al. studied the effect of the Y/Ti ratio to observe the oxide distribution behavior [178]. Furthermore, the addition of Zr and Hf resulted in the formation of even more refined nano-oxides, contributing to superior mechanical properties. Specifically, oxides, including Zr and Hf, are observed as $Y_4Zr_3O_{12}$ and $Y_2Hf_2O_7$ compounds, respectively [177,179–181]. Gao et al. showed that Zr addition suppresses the formation of Y-Al-O oxides and promotes the formation of finer $Y_4Zr_3O_{12}$ oxides in ODS ferritic steel [182]. Xu et al. compared two kinds of ODS steel, with and without Zr addition, and demonstrated the exceptionally improved mechanical properties with ultrahigh number densities of nano-oxides in the Zr-containing variant [183]. Similar to Zr addition, Hf addition to ODS steel effectively suppressed the formation of Y-Al-O oxides and refined the grain size [184]. TEM and HRTEM study on $Y_2Hf_2O_7$ indicates that an excellent improvement in the coherency of nano-oxides is achieved with Hf addition [185]. Tang and Kang state that $Y_2Hf_2O_7$ particles are found to be finer than $Y_4Zr_3O_{12}$ particles, which leads to better mechanical properties [186,187]. Additionally, Huang et al. showed that Hf is more potent in refining the oxides than Ti [188]. Common yttrium-based nano-oxide compounds are listed in Table 2.6.

Table 2.6 Common nano-oxide compounds based on yttrium with their crystallographic structure (adapted from [161]).

Alloying Element	Oxide Compound(s)	Lattice Structure
Yttrium	Y_2O_3	Cubic
Titanium	Y_2TiO_5	Orthorhombic
	$Y_2Ti_2O_7$	Cubic
Aluminum	$Y_4Al_2O_9$	Monoclinic
	$Y_3Al_5O_{12}$	Cubic
	$YAlO_3$	Hexagonal
Zirconium	$Y_4Zr_3O_{12}$	Trigonal
	$Y_2Zr_2O_7$	Cubic
Hafnium	$Y_2Hf_2O_7$	Cubic

2.5.4 Studies Pertaining to Inconel 625

The available literature on ODS IN625 is scarce, with most studies concentrating on the addition of yttria. Within the scope of metal matrix composites, Ghodsi et al. investigated various L-PBF parameters for IN625 reinforced with yttria-stabilized zirconia to monitor porosity and mechanical properties [189]. Spierings et al. demonstrated that AM of irregularly shaped ODS IN625 powders is possible, although it requires significant alterations to the process window [190]. A remarkable increase in strength in AM ODS IN625 in the study of Li et al, at room temperature, 800 °C and 1100 °C, compared to the non-ODS variant [191]. In terms of corrosion resistance, Arnold et al. reported that the oxidation rate of ODS IN625 produced via spark plasma sintering was reduced 40-fold compared to the wrought component [192]. Moreover, Zou et al., successfully incorporated La_2O_3 into IN625 to produce nano-sized $La_2Ti_2O_7$ oxides using wire arc DED and achieved an excellent oxidation resistance at elevated temperatures [193].

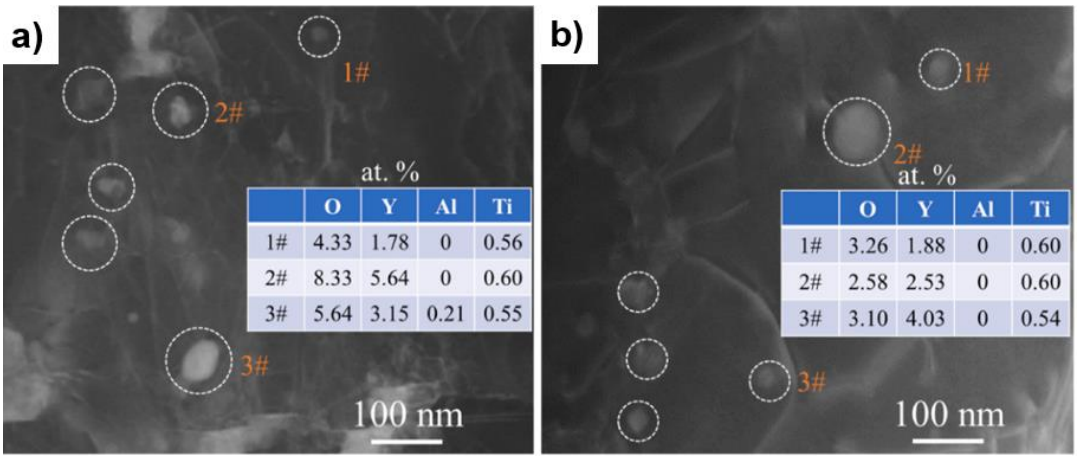

Figure 2.22 STEM image showing the nano-oxides in a) AB and b) heat-treated ODS IN625, with their atomic fraction [191].

CHAPTER 3

EXPERIMENTAL PROCEDURE

3.1 Starting Materials and Alloy Design

In this study, a new grade of ODS IN625 was intended to be developed. For the production of ODS IN625 via AM, gas atomized IN625 powders with particle sizes ranging from 24 to 52 μm was supplied from Oerlikon Metco Europe GmbH as shown in the SEM micrographs in Fig. 3.1. In order to see the effect of production method on the final properties of the IN625, a wrought IN625 rod, which had been heat-treated at 951 °C for 30 minutes and then water cooled, was purchased from VDM Metals International GmbH. The elemental composition of the IN625 powders and the wrought component as provided by their manufacturers are listed in Table 3.1, along with the nominal IN625 composition prescribed in ASTM-B443 standard [124].

Table 3.1 Elemental composition of the IN625 powders and rod with respect to the ASTM-B443 standard specified for wrought IN625 (in wt%).

	IN625 Powder	**IN625 Rod**	**ASTM-B443**
Nickel	65.4	59.9	58.0 min.
Chromium	20.9	22.3	20.0-23.0
Iron	0.20	4.36	5.0 max.
Molybdenum	8.75	9.12	8.0-10.0
Niobium + Tantalum	3.60	3.39	3.15-4.15
Manganese	0.41	0.06	0.50 max.
Aluminum	0.02	0.24	0.40 max.
Titanium	0.02	0.32	0.40 max.
Carbon	0.03	0.02	0.10 max.
Silicon	0.48	0.16	0.50 max.

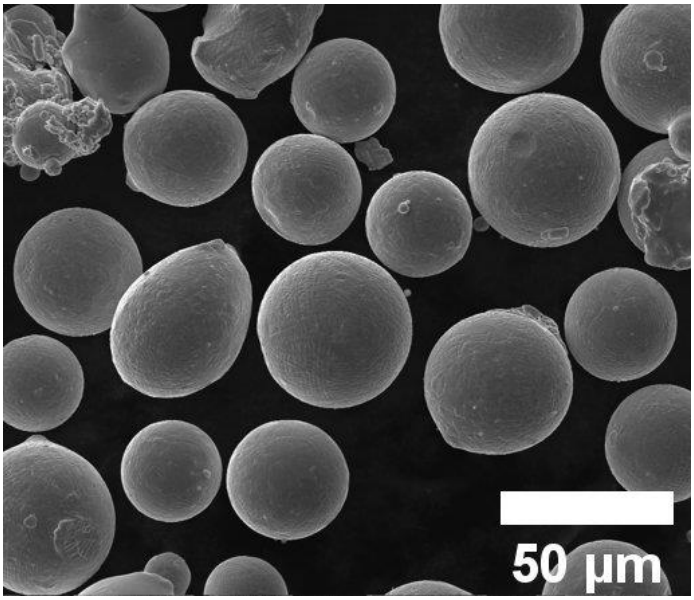

Figure 3.1 SEM micrograph of IN625 powders.

Y_2O_3 is the most commonly used additive for studies regarding ODS of metals. This preference is attributed to the fact that Y_2O_3 and Y_2O_3-based nano-oxides have the greatest thermodynamic stability, making them resistant to coarsening effects at temperatures higher than 1200 °C [161,176]. However, Y_2O_3 is added to alloys that contain oxide-forming elements such as Al and Ti in their composition, which are not sufficiently present in IN625. Additionally, Hf is shown in several studies to produce the finest nano-oxides, due to its effectiveness in refining the other oxides [179,185,186,188]. Consequently, powder forms of Y_2O_3 and Hf were selected as starting materials in this study, along with IN625 powders. High-purity Y_2O_3 and Hf powders were obtained from Nanografi Nanotechnology Co., with particle sizes of 15-44 μm and 18-38 nm, respectively. Both powders have irregular morphology, as shown in the SEM micrographs in Fig. 3.2.

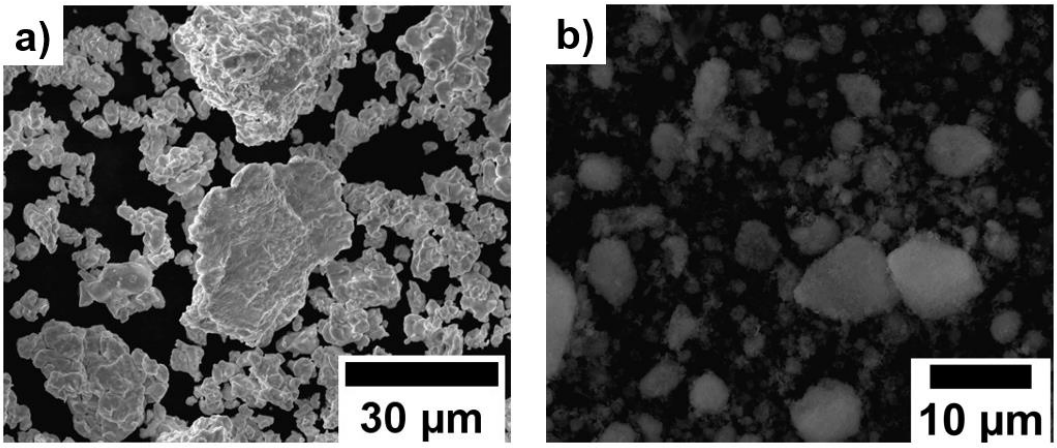

Figure 3.2 SEM micrographs of a) Hf and b) Y_2O_3 powders.

3.2 Mechanical Mixing of Powders

To achieve a homogeneous dispersion of nano-sized Y_2O_3 on the surface of the IN625 powders without losing their sphericity, ball milling was performed using a zirconia (i.e., ZrO_2) vial with zirconia balls of varying diameters (5 mm, 1 mm and 0.5 mm). Mixing of the powders was carried out using the Fritsch Pulverisette P6 classic line planetary mono mill high-energy ball milling machine under Ar atmosphere to prevent contamination. To optimize the mixing parameters (i.e., mixing time and rotation speed), mixing times were set at 2, 5, 10, 30, 60 and 120 minutes, while rotation speeds ranged from 200 to 500 rpm. For comparison, powders were also mixed by hand. It was found that Y_2O_3 powders were effectively dispersed onto the IN625 powders with minimal agglomeration when using the rotation speed of 200 rpm with ZrO_2 balls with diameters of 0.5 mm and 1 mm. The ball milling machine, zirconia vial and balls used in mechanical alloying are shown in Fig. 3.3.

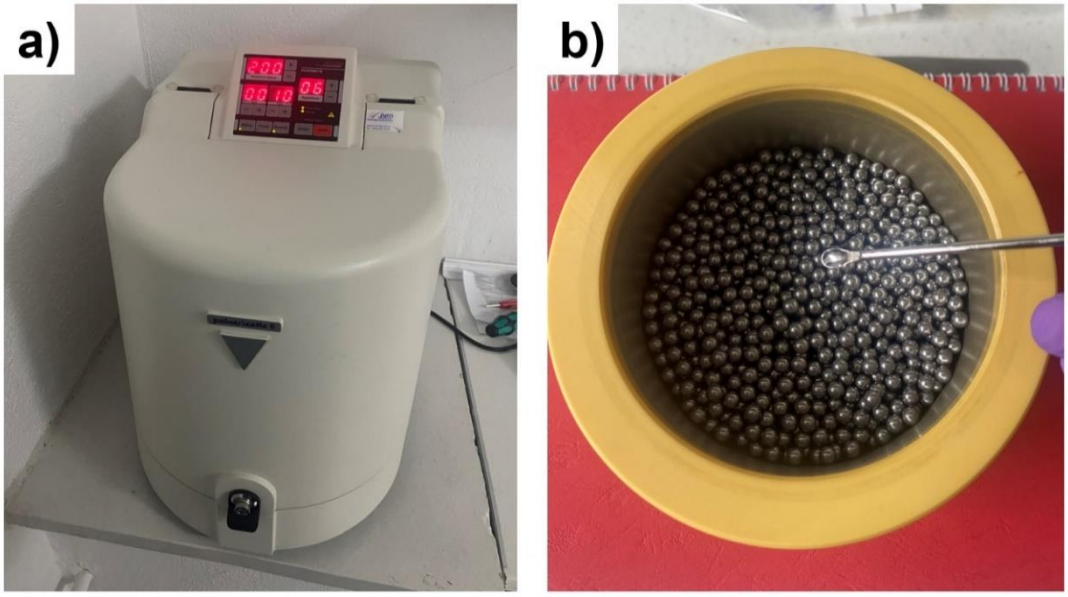

Figure 3.3 a) Ball milling machine and b) zirconia vial with balls inside.

3.3 Laser Powder Bed Fusion of Standard and ODS IN625 Powders

The AM of ODS IN625 and non-ODS variant (hereafter referred to as “STD”) was performed using an EOS M290 Selective Laser Melting machine equipped with a 400 W ytterbium-fiber laser with a spot size of 110 μm. A total of 25 different combinations of scan speed (mm/s) and laser power (W) were tested to determine the optimal combination of parameters utilizing the parameter matrix shown in Fig. 3.4. For each set of parameters, a batch of cube-shaped samples with a dimension of 15x15x15 mm were produced and used for porosity and hardness measurements. In other words, two batches of the parameter matrix cubes for STD and ODS IN625 has been produced for the parameter optimization. The layer thickness and hatch spacing were kept constant at 40 μm and 110 μm, respectively. A bi-directional scanning strategy with a rotation angle of 67° was deployed during the production of cubes. After a thorough metallographic investigation, 4 parameter sets in each variant were selected for further microstructural analysis to make a final decision on the optimum parameters. For both alloys, scanning power of 285 W and scanning speed of 960 mm/s were determined to be the optimal parameter set for L-PBF production.

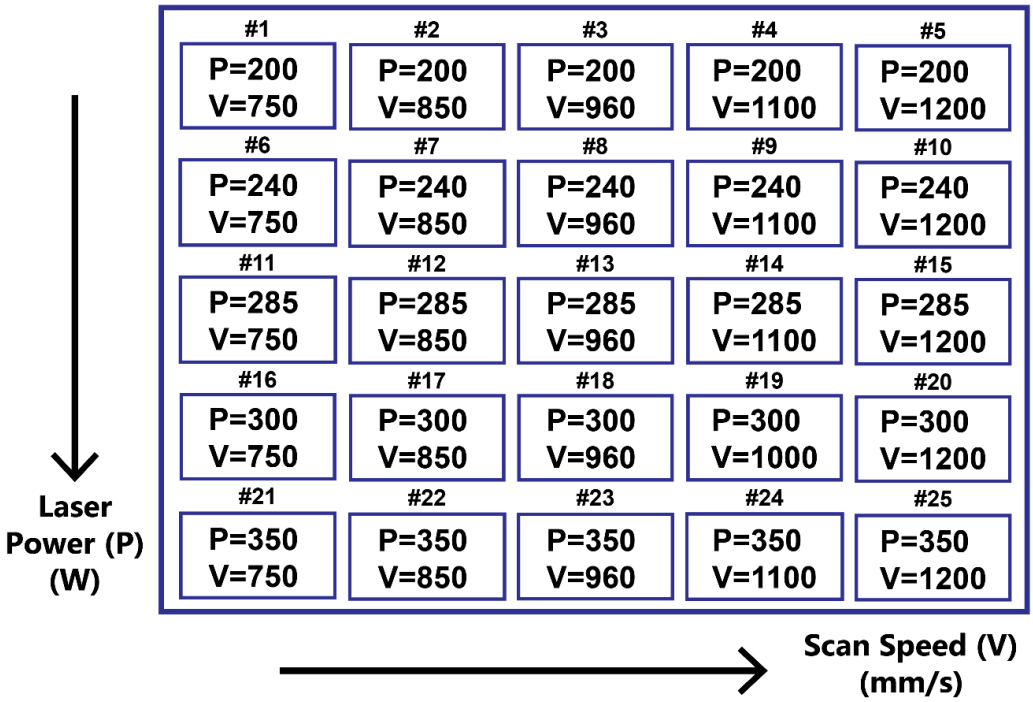

Figure 3.4 Production matrix for the L-PBF of powders.

Using the selected optimal parameter set, cylindrical samples with a diameter of 10 mm and a length of 60 mm were produced vertically on a stainless steel build plate in an Ar atmosphere to prevent cross-contamination. A cylindrical sample produced by L-PBF method and a dog-bone shaped tensile testing specimen machined from that sample are shown in Fig. 3.9.

3.4 Heat Treatments

The heat treatments of all alloys were carried out using a Protherm MOS 180/4 chamber furnace shown in Fig. 3.5, with a heating rate of 10 °C/min. The samples were placed in alumina crucibles and a protective Ar purge was applied during heat treatment to prevent contamination. During the study, two different heat treatments were applied to the samples. Namely, additively manufactured AB alloys were directly aged at the selected aging temperature and also AB alloys along with

conventionally produced rod were solutionized and aged according to the selected solutionizing and aging temperature.

Figure 3.5 The chamber furnace used for the heat treatments.

3.4.1 Solutionizing of the Alloys

Solutionizing of the IN625 takes place at temperatures exceeding 1000 °C. However, the solutionizing temperature and the duration plays an important role in determining the final microstructure as well as mechanical properties. The recommended solutionizing temperature for IN625 is 1150 °C for 2 hours [137]. In the current study, three solutionizing temperatures ranging from 1100 °C to 1200 °C were tested with durations varying from 10 to 120 minutes to optimize the solutionizing process. Specifically, a parameter matrix similar to that used in L-PBF production, comprising 15 different temperature-time combinations, was evaluated to identify the optimal solutionizing temperature. For the best mechanical properties, 15 AB

ODS IN625 samples were sectioned and solutionized according to the matrix shown in Fig. 3.6. To prevent unwanted phase formation during cooling, all samples were water-quenched right after heat treatment.

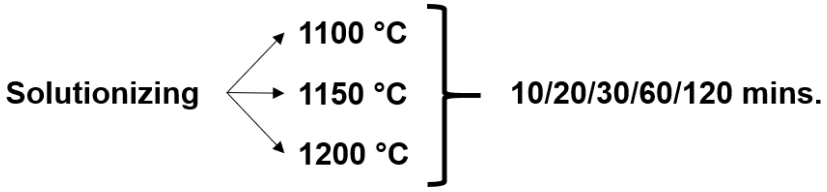

Figure 3.6 Heat treatment routes to select optimal solutionizing conditions.

After metallographical investigations and hardness tests on solutionized samples, the optimal solutionizing temperature was determined to be 1150 °C for 60 minutes. STD, ODS IN625 and conventionally produced rod were then sectioned and solutionized for microstructural analysis using this parameter set and subsequently water quenched. Moreover, tensile test specimens from aforementioned samples were also subjected to the same procedures prior to their tensile testing.

3.4.2 Aging Temperature

Similar to the solutionizing, aging heat treatment is also applied to IN625 samples to promote strengthening phases and enhance the mechanical properties at elevated temperatures. Aging temperatures for IN625 are between 600 and 900 °C [194]. Due to the number and complexity of phase transformations within this temperature range, selecting the appropriate aging temperature is crucial for achieving optimal mechanical properties. Aging treatments have been applied on two different conditions such as AB and solutionized samples. The aging temperature was determined based on the mechanical property changes on AB ODS IN625 after their direct aging (DA). DA, a relatively novel heat treatment for additively manufactured IN625 samples, was conducted at temperatures between 700 °C and 800 °C [138].

To optimize the aging process, these two temperatures were tested with durations ranging from 2 to 36 hours, resulting in a parameter matrix of 12 different temperature-time combinations, as shown in Fig. 3.7. The aging treatment on samples was followed by air cooling.

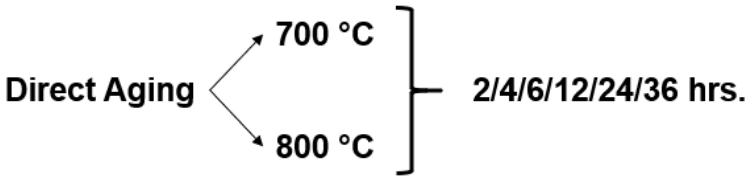

Figure 3.7 Heat treatment routes to select optimal DA conditions.

Based on metallographic examinations and hardness tests on AB ODS IN625 alloys, the optimal aging treatment parameters were selected as 700 °C for 24 hours. These parameters were subsequently applied to the solutionizing and aging heat treatments, resulting in a combination of solutionizing at 1150 °C for 60 minutes followed by aging at 700 °C for 24 hours.

3.5 Microstructure Characterizations

The cubes produced for the parameter study and cylindrical samples were separated from the build plate using electrical discharge machining (EDM) by the manufacturer. Each cube was metallographically prepared for porosity measurements in the as-polished condition. The sample surfaces were ground using SiC abrasive papers with grits of 220, 400, 800, 1200 and 2000. Final polishing of the samples was carried out using diamond suspensions of 6 μm and 1 μm particle sizes, followed by colloidal silica suspension with a particle size of 0.25 μm. After cleaning the polished surfaces with ethanol, the samples were electrolytically etched to reveal the microstructural features by means of a solution of 5 g oxalic acid and 95 ml of HCl at 3 V for 10-15 seconds. In the case where electro-etching was found to be too aggressive, the samples were immersed in a Kalling's No.2 Reagent (100

ml ethanol, 100 HCl and 5 g $CuCl_2$) etchant for 30 to 60 seconds for chemical etching.

3.5.1 Optical Microscopy

3.5.1.1 Porosity Measurements

For pore analysis, surfaces of the cubes produced with different parameters from the production matrix were examined in as-polished condition using optical microscopy (OM) under Huvitz Digital Microscope (HDS-5800). Low-magnification images were captured from five different locations on each sample, and ImageJ 1.49v digital processing software was utilized for the quantification of the pore content. Using the global thresholding method, the area percentage of the porosities were calculated and averaged for each sample. Samples having the lowest porosity and standard deviation were identified.

3.5.1.2 Microstructural Investigations

Micrographs of etched samples were captured at various magnifications using OM to study the shape and distribution of the melt pools. Melt pool length and depth for the cubes from the production matrix were calculated analyzing their microstructural images using ImageJ 1.49v digital processing software. For each sample, measurements were taken from 10 different melt pools across two low-magnification OM micrographs and averaged. Grain morphologies in as-built (AB), direct aged (DA), and solutionized and aged (SA) conditions were analyzed, where semi-quantitative grain size measurements were conducted in the SA condition using the same software. Excluding edge grains and twin boundaries, at least three measurements were taken for each grain, and average grain sizes, along with their number fractions, were plotted. Additionally, the columnar and dendritic structures in the AB alloys were characterized, while microstructural investigations of heat-

treated samples focused on melt pool boundaries, secondary phases, and grain structures.

3.5.2 Scanning Electron Microscopy

3.5.2.1 Microstructural and Compositional Analysis

The morphology of the virgin and ball-milled powders, melt-pools in AB, SA, and DA alloys, as well as the secondary phases and local compositional differences, were analyzed using scanning electron microscopy (SEM). FEI-430 NanoSEM scanning electron microscope equipped with EDAX SSDD Apollo10 Energy Dispersive Spectroscopy (EDX) detector was used, operating at an acceleration voltage of 20 kV. Similarly, a Hitachi SU5000 Field Emission Scanning Electron Microscope, equipped with an Oxford X-MaxN 80 EDX detector, was utilized for chemical composition analysis of the secondary phases and elemental mapping of selected regions at an acceleration voltage of 20 kV.

3.5.2.2 Texture and Grain Boundary Analysis

The textures and grain structures of the AB and heat-treated IN625 samples were analyzed using the Electron Backscatter Diffraction (EBSD) technique. Sample preparation for EBSD involved grinding 300 mm-thick samples with SiC abrasive paper up to 2000 grit followed by electro-polishing. Electro-etching was conducted using a Struers TenuPol-5 twin jet electro polisher at -40 °C and 15 V in a solution of 5 vol% perchloric acid and 95 vol% methanol. EBSD was implemented on a 1000 μm × 1000 μm region, with a step size of 1 μm for all samples, using the SEM equipped with a TSL EBSD detector. Data refinement was carried out using OIM 5.31 software to generate inverse pole figure (IPF) maps, grain boundary maps, Kernel average misorientation (KAM) maps and pole figures.

3.5.3 Transmission Electron Microscopy

The presence of the nano-oxides and their composition in AB condition were examined through TEM. A JEOL JEM-ARM200CFEG UHR-TEM equipped with EDAX EDX detector at 200 kV and JEOL JEM 2100 HRTEM equipped with Gatan Model 833 Orius SC200D CCD camera were used for these investigations. Sample preparation for TEM analysis involved grinding the samples to a thickness of 100 nm using SiC abrasive paper (2000 and 4000 grit) and punching them into 3 mm diameter discs. The final thinning of the samples was achieved by electro-polishing with the same procedure for the EBSD sample preparation.

3.6 Mechanical Properties

The preliminary evaluation of the mechanical behavior of the samples at room temperature was conducted via microhardness measurements, followed by room temperature tensile testing. Microhardness measurements were performed using a Shimadzu HMV-2 E machine, applying 0.5 kg of load for 10 seconds. A total of 21 measurements were taken at various points on each sample surface. For tensile testing, vertically-built cylinders have been machined as per the ASTM E8M standard, which requires a dog-bone shape with threaded ends with gauge length five times the diameter. Fig. 3.8 and Table 3.2 specifies the dimensions of the tensile test specimen, and in Fig. 3.9 the manufactured cylinder and machined tensile specimen is shown.

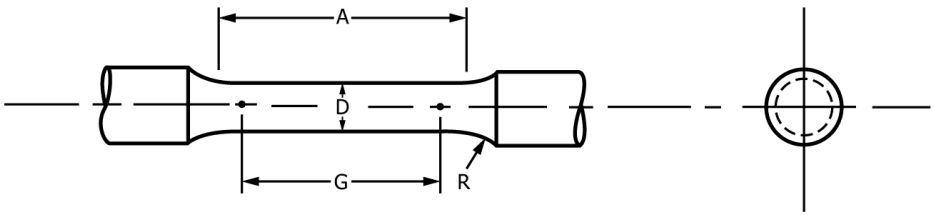

Figure 3.8 Cylindrical tensile testing specimen machined according to the ASTM E8M standard [195].

Table 3.2 The dimensions of specimens (small-size) used in this study.

Component	**Dimension (mm)**
Gauge Length (G)	20.0 ± 0.1
Diameter (D)	4.0 ± 0.1
Radius of Fillet, min. (R)	4
Length of Reduced Parallel Section, min. (A)	24

Room temperature tensile testing of the AB and heat-treated samples was conducted according to ISO 6892 – 1 standard, using the BESMAK BMT-E series universal testing machine. The initial strain rate up to the yield point was $3x10^{-4}$ s^{-1}, while it is $2.4x10^{-4}$ s^{-1} from the yield point to the fracture. On the other hand, tensile tests at 700 °C have been carried out using an Instron 5582 universal testing machine equipped with a tubular furnace. The initial strain rate of the high temperature tensile testing was $1.5x10^{-4}$ s^{-1}, as per ISO 6892-2 standard. To have thorough and reliable results, each tensile test was performed three times along the z-direction (i.e., BD), and the values including yield strength and elastic modulus, were determined from the stress-strain curves.

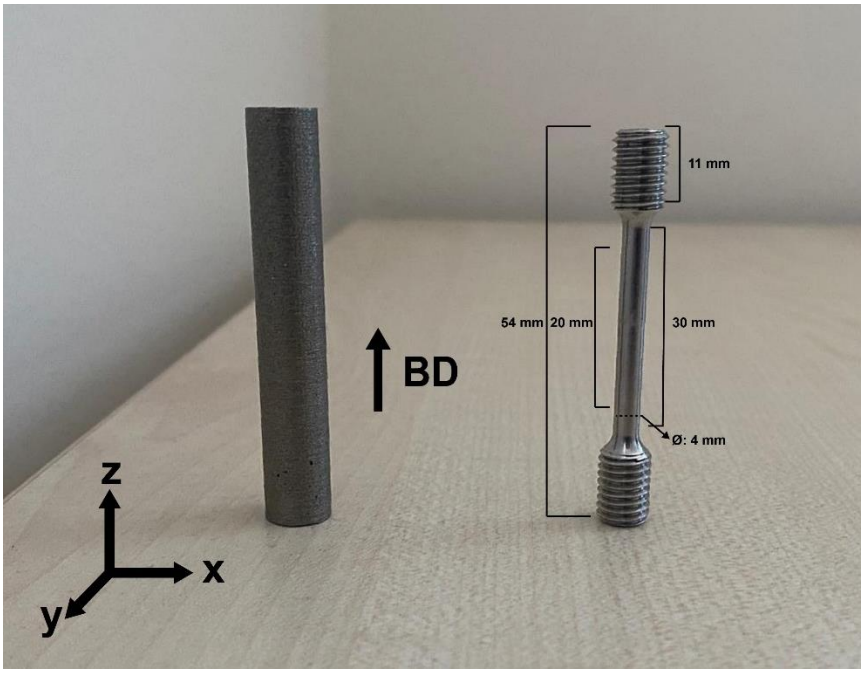

Figure 3.9 Cylindric sample after L-PBF production and tensile test specimen.

CHAPTER 4

RESULTS AND DISCUSSION

4.1 Ball Milling Parameter Determination

Mechanical alloying via ball milling for ODS applications often results in deformed powders, which decreases the flowability and affects the quality of L-PBF production [196]. An optimal combination of parameter selection is essential for satellite formation, indicating a proper spread of nano-oxides on micron-sized powders. In this study, mechanical mixing of powders was performed at different durations and rotation speeds using different sizes of zirconia balls. It was found that ball milling with 5 mm diameter media severely disfigures the shape of the IN625 powders usually after 5 minutes of rotation, regardless of the rotation speed. This is illustrated in Fig. 4.1.

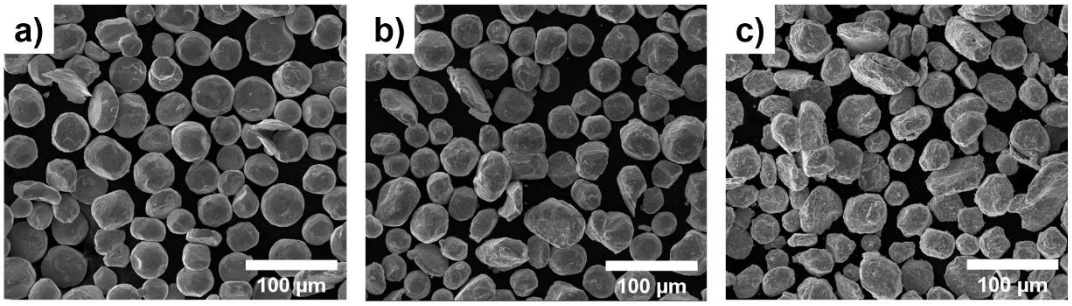

Figure 4.1 SEM micrographs showing the morphology of ball-milled IN625 with 5 mm balls for 10 minutes at a) 300 rpm b) 400 rpm c) 500 rpm.

On the other hand, reducing the size of ball milling media as well as the rotation speed has been shown to effectively distribute nano-oxides evenly without distorting the shape of the powders. Therefore, a mixture of balls with 0.5 mm and 1 mm diameters was selected, and speed was set to 200 rpm. After determination of the dimensions of the milling media and the rotation speed during mixing, mechanical mixing was carried out for durations ranging from 2 minutes to 120 minutes to gain

thorough insights into the powder distribution and agglomeration. Prior to mechanical mixing, hand mixing was also carried out to observe the satellite formation of the nano-oxides. Fig. 4.2. shows the SEM micrographs of IN625, Y_2O_3 and Hf powders mixed either by hand mixing or ball milling for different times. As shown in this figure, hand mixing does not yield proper satellite formation, whereas the fraction of the Y_2O_3 nano-powders in mechanically-mixed samples remarkably increases up to 30 minutes after which agglomeration of nano-oxides begins to occur at 60 minutes. Powders appear to break apart in the case of 100 minutes, then start re-agglomerating at 120 minutes. Consequently, ball milling for 100 minutes at 200 rpm has been found to produce the best satellite structures.

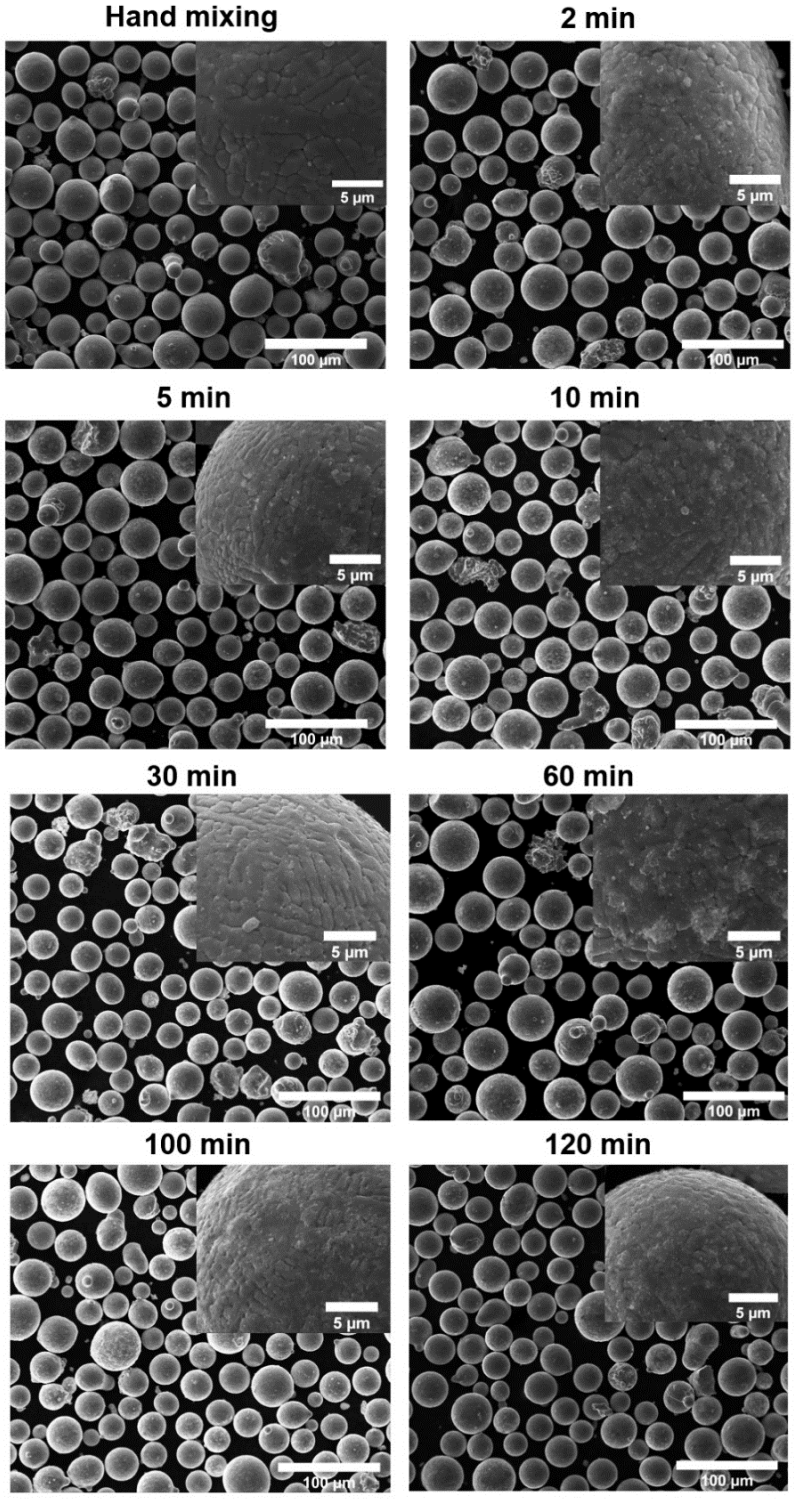

Figure 4.2 SEM micrographs of mechanically alloyed IN625-0.3Y_2O_3-0.4Hf powders with the mixture of 0.5 mm and 1 mm diameter media at 200 rpm, showing yttria coating and morphology with respect to the milling time.

4.2 Parameter Optimization for Laser Powder Bed Fusion

Two batches, including standard (STD) and ODS IN625, and 25 different samples, according to the production matrix given in Fig. 3.4., are produced via L-PBF.

4.2.1 Standard IN625

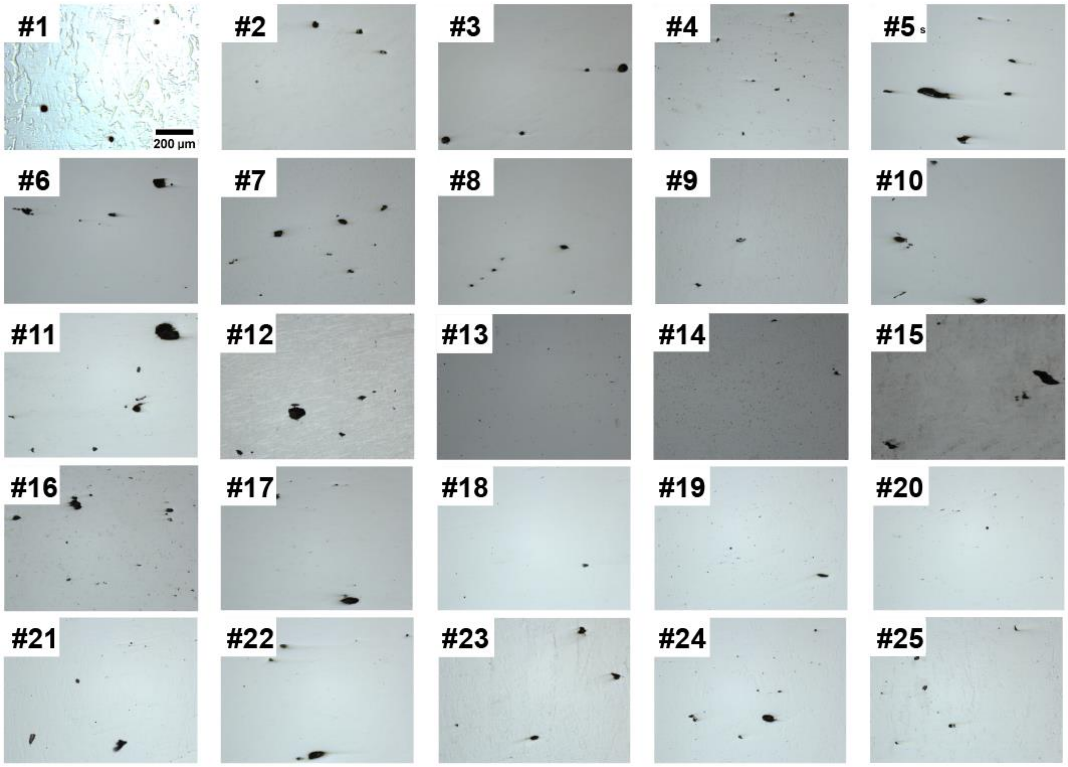

Figure 4.3 OM micrographs of STD IN625 samples in as-polished condition, with numbers corresponding to those specified in the parameter set of the production matrix.

The as-polished optical microscope (OM) micrographs of standard IN625 are shown in Fig. 4.3 above. Both scan speed and laser power have a considerable effect on porosity formation in samples. From Fig. 4.3, an increase in the porosity is apparent at lower scan speeds and higher laser powers. Specifically, gas porosities are observed at moderate scan speeds and laser powers, while lack of fusion porosities (i.e., keyhole porosity) starts to form at higher scan speeds and laser powers, all of

which is consistent with the findings reported in the literature [197–201]. Lack of fusion is a result of insufficient melting between the layers or convective flows due to higher laser powers [202]. Such porosities are considered very detrimental, especially when they are accumulated in a specific region. In contrast, gas pores, are observed as spherical and remarkably smaller than lack of fusion porosities. They result from the hydrogen encapsulation due to the moisture on the surface of the powders [203,204]. Fig. 4.4 shows the amount of porosity and hardness values with respect to the sample number. It is clear from this figure that while hardness values among the samples are relatively similar, porosities as high as 1% have been observed at the extremes of the parameter matrix. On the other hand, porosity amount decreases to around 0.1% with the combination of moderate parameters. This low porosity content has been achieved in several other studies, following the similar strategies for the L-PBF of IN625 [205,206]. Among all, four samples (#9, #13, #18 and #20) were found to have the minimum porosity with the lowest standard deviation, and were selected for the melt pool analysis. The quantitative values of porosity percentages and hardness values of selected samples, along with their parameter sets are listed in Table 4.1.

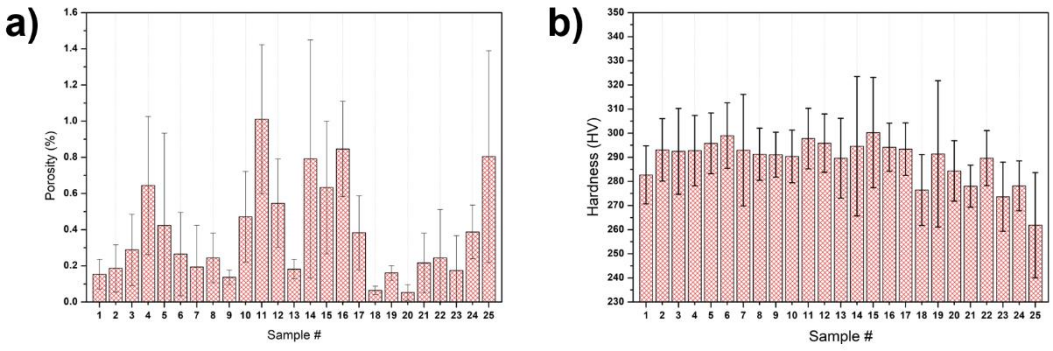

Figure 4.4 a) Porosity amount and b) hardness values vs. sample number for the STD IN625.

Table 4.1 Porosity percent and hardness values of the selected STD IN625 samples from the production matrix.

Sample #	Parameter Set	Porosity (%)	Hardness (HV)
9	P=300 W V=750 mm/s	0.14 ± 0.04	291 ± 9
13	P=285 W V=960 mm/s	0.18 ± 0.05	290 ± 16
18	P=240 W V=960 mm/s	0.07 ± 0.02	276 ± 15
20	P=240 W V=1200 mm/s	0.05 ± 0.04	284 ± 13

As demonstrated in Table 4.1, Samples #18 and #20 have the minimum porosity content. However, their hardness values are lower than those of Samples #9 and #13, which also show higher standard deviations. Conversely, Samples #9 and #13 have slightly higher porosity percentages than the other samples, but they possess higher hardness values. Melt pool analyses of Samples #9, #13, #18 and #20 were conducted based on the OM micrographs of STD samples in etched condition (Fig. 4.5), and their melt pool dimensions are listed in Table 4.2. The melt pools in Sample #9 appear slightly shallow and wide, as they have the minimum depth and the greatest width among the samples, with a melt pool depth and width of 61.5 μm and 159.6 μm, respectively. Moreover, keyhole porosities were also observed in that sample. On the other hand, deeper melt pools, which infer higher energy inputs are found in Samples #18 and #20. Both samples exhibit wider melt pools, along with the highest standard variation, which is resulted from a combination of high laser power and lower scan speeds [206]. Eventually, Sample #13 (285 W, 960 mm/s) shows the most properly-formed melt pools among the final samples, and therefore, has been chosen as the optimal parameter set.

Table 4.2 Average melt pool dimensions of the selected STD samples.

Sample #	Melt Pool Depth (µm)	Melt Pool Width (µm)	Melt Pool Aspect Ratio
9	61.5 ± 13.5	159.6 ± 41.8	2.60
13	62.1 ± 9.7	124.5 ± 19.0	2.00
18	68.1 ± 10.8	154.6 ± 44.2	2.27
20	71.4 ± 10.0	145.7 ± 24.0	2.04

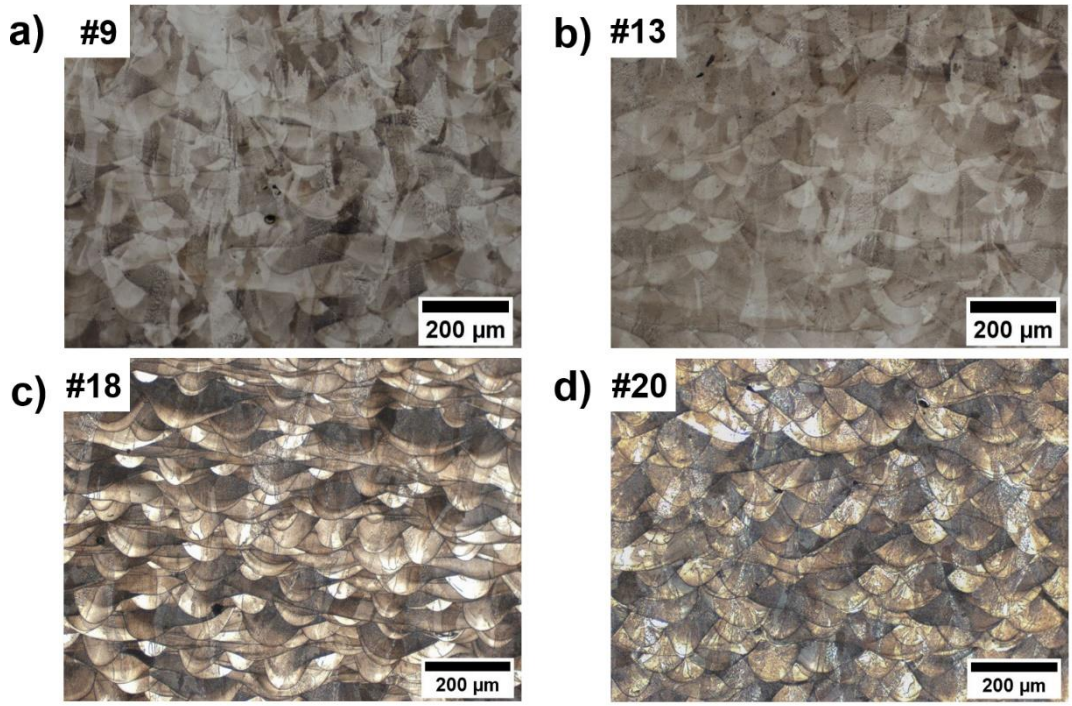

Figure 4.5 Melt pool micrographs of a) Sample #9, b) Sample #13, c) Sample #18 and d) Sample #20 in etched condition.

4.2.2 Oxide Dispersion Strengthened IN625

The same procedures in determining the optimum processing parameters used for STD IN625 were also applied for ODS IN625. OM micrographs in the as-polished condition for each parameter set, along with corresponding hardness values and

porosity amounts are shown in the following figures (Fig. 4.6 and 4.7). The behavior of the ODS powders exhibits a similar pattern to that of STD IN625, with a slightly improved porosity at moderate laser powers and scan speeds. It was observed that the ODS samples produced at moderate scan speeds and low powers contain approximately 0.1%, porosity while parameters at the extremes in the matrix results in a considerable porosity reaching up to 1.4%. Moreover, Sample #23 exhibited solidification cracking, which is likely owing to residual stresses or the presence of semisolid second-phase particles during solidification [207]. Based on the hardness values coupled with porosity percentages, Samples #1, #7, #13 and #21 were selected for further microstructural investigation. The quantitative values of porosity percentages and hardness for the selected samples are shown in Table 4.3.

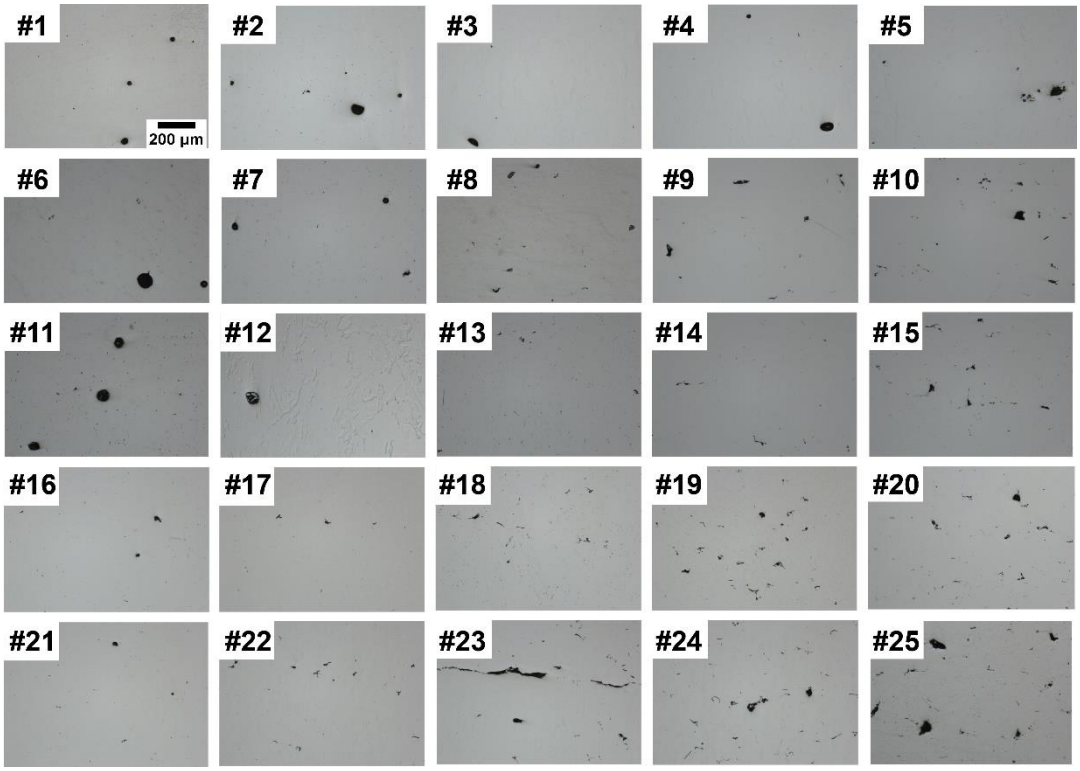

Figure 4.6 OM micrographs of ODS IN625 samples in as-polished condition, with numbers corresponding to those specified in the parameter set of production matrix.

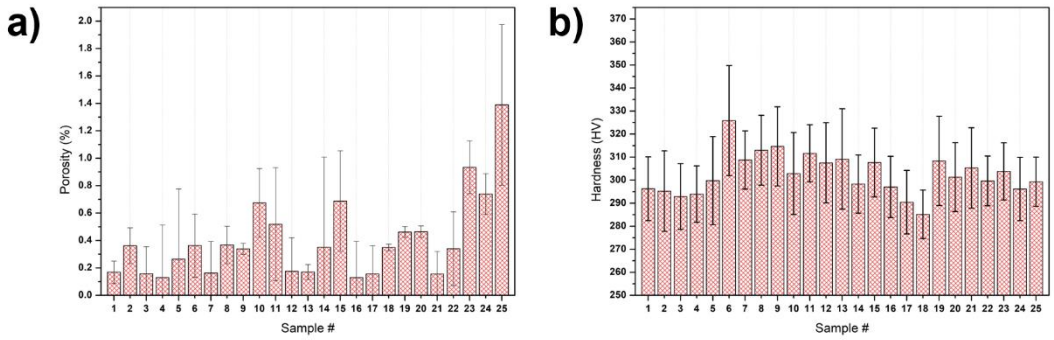

Figure 4.7 a) Porosity amount and b) hardness values vs. sample number for the ODS IN625.

Table 4.3 Porosity percentage and hardness values of the selected ODS IN625 samples.

Sample #	Parameter Set	Porosity (%)	Hardness (HV)
1	P=350 W V=750 mm/s	0.17 ± 0.07	296 ± 14
7	P=300 W V=850 mm/s	0.16 ± 0.19	309 ± 13
13	P=285 W V=960 mm/s	0.18 ± 0.05	309 ± 21
21	P=200 W V=750 mm/s	0.16 ± 0.05	305 ± 17

The porosity percentages and hardness values of the selected samples are somewhat similar to each other. Therefore, microstructures in etched conditions play a more predominant role in the selection of the optimal parameter set in this case. Melt pool configurations of the selected samples are shown in Fig. 4.8, and the melt pool dimensions of the selected samples are listed in Table 4.4. The melt pools in samples #1 and #7 are relatively deeper but larger in width, indicating a lower energy input [208]. In contrast, sample #21 exhibits relatively shallow melt pools. Quantitatively, samples #13 and #21 have the least standard variation in their melt pool depth and

width, inferring more stable melt pool structures. However, keyhole porosities associated with the lack of fusion are visible in samples #1, #7 and #21. Consequently, the parameter set of Sample #13 has, once again, has been identified as the optimal choice for the ODS IN625 production. Note that using the same L-PBF parameters resulted in different melt pool aspect ratios, with the STD alloy exhibiting an aspect ratio of 2 and the ODS alloy showing 1.61. This indicates that the addition of Hf and Y_2O_3 altered the laser absorptivity of IN625 powders which can be seen from their larger melt pool depths.

Table 4.4 Average melt pool dimensions of the selected ODS samples.

Sample #	Melt Pool Depth (µm)	Melt Pool Width (µm)	Melt Pool Aspect Ratio
1	94.4 ± 12.9	174.4 ± 35.2	1.85
7	82.3 ± 9.9	159.0 ± 14.3	1.93
13	80.9 ± 10.8	130.1 ± 12.9	1.61
21	79.7 ± 11.2	155.9 ± 24.4	1.96

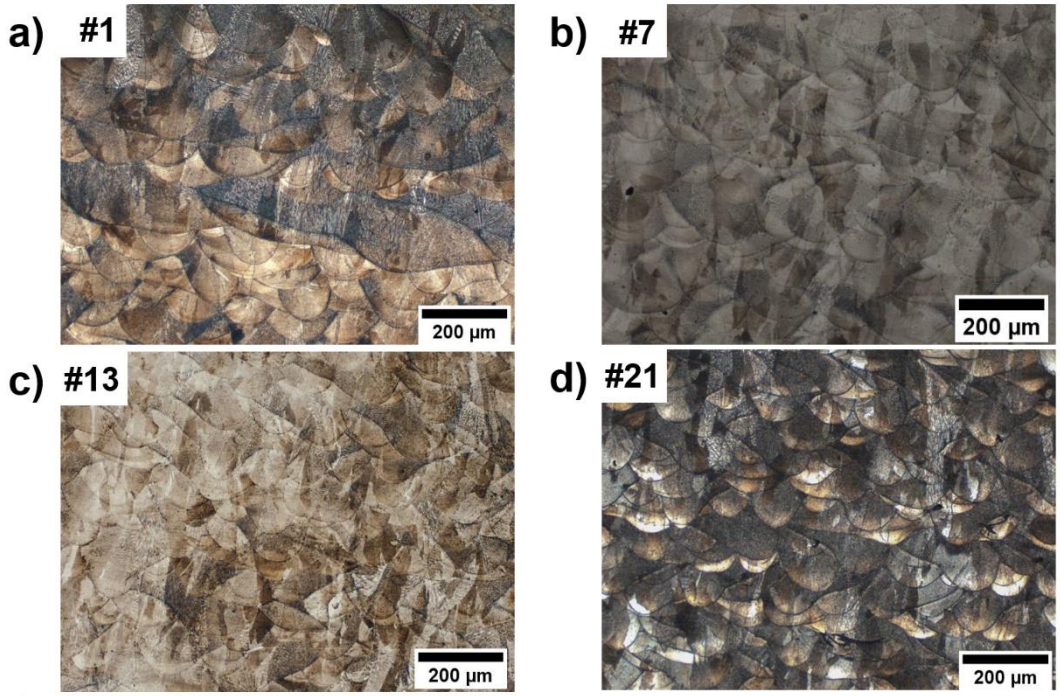

Figure 4.8 Melt pool micrographs of a) Sample #1, b) Sample #7, c) Sample #13 and d) Sample #21 in etched condition.

4.3 Selection of the Heat Treatment Route

There are several heat treatment methods to control microstructural features of IN625. As mentioned in the literature review, most of the heat treatments for conventional and AM IN625 include stress relieving or two step solutionizing followed by aging stages. Owing to the high number of parameters involved, hardness measurements were initially conducted on ODS samples to assess the changes in mechanical properties. This is followed by microstructure characterization for the final decision.

4.3.1 Solutionizing Temperature

To control the morphology, quantity, size, and distribution of secondary phases, as well as the grain structure, IN625 is usually subjected to solutionizing heat treatment

to fully dissolve the alloying elements into the nickel matrix. While various solutionizing temperatures have been tested to enhance the mechanical properties of the IN625 alloy, the specific role of the treatment temperature in microstructural evolution and mechanical performance remains ambiguous due to the numerous variables influencing the final microstructure and properties [209]. Fig. 4.9 illustrates the hardness evolution of ODS IN625 after the heat treatments according to the parameter matrix in Fig. 3.6.

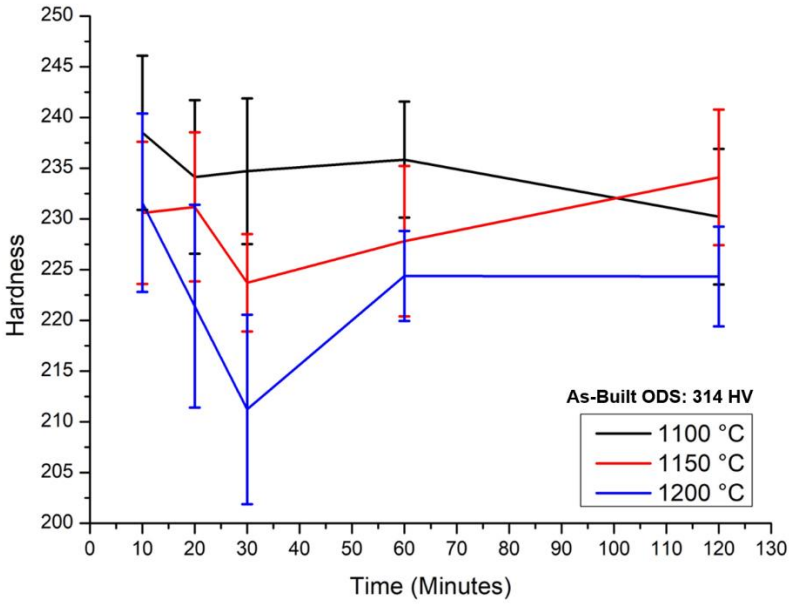

Figure 4.9 The hardness of ODS IN625 alloys solutionized at 1100, 1150 and 1200 °C from 10 to 120 minutes.

A notable and expected decrease in hardness is observed in all samples, with values ranging between 210 and 240 HV which are significantly lower than those of the AB alloy that is 314 HV. At 1100 °C, the hardness remains relatively stable compared to the treatments at 1150 and 1200 °C, ranging between 230 and 240 HV. This stability has been attributed to the slower dissolution of secondary phases, such as carbides. At or below 1100 °C, dissolution of the carbides has been reported to be sluggish, which impacts grain coarsening and the solid solution content during heat treatment [209]. Conversely, the dissolution of secondary phases seems to have accelerated significantly at temperatures above 1150 °C, leading to a noticeable drop

in hardness for samples treated at 1150 and 1200 °C within 30 minutes. Quantitatively, the hardness reduction is more apparent in the samples heat-treated at 1200 °C, with a decrease of 25 HV from the initially heat-treated state (i.e., for 10 minutes) to the sample treated for 30 minutes. OM micrographs of each sample are presented in Fig. 4.10.

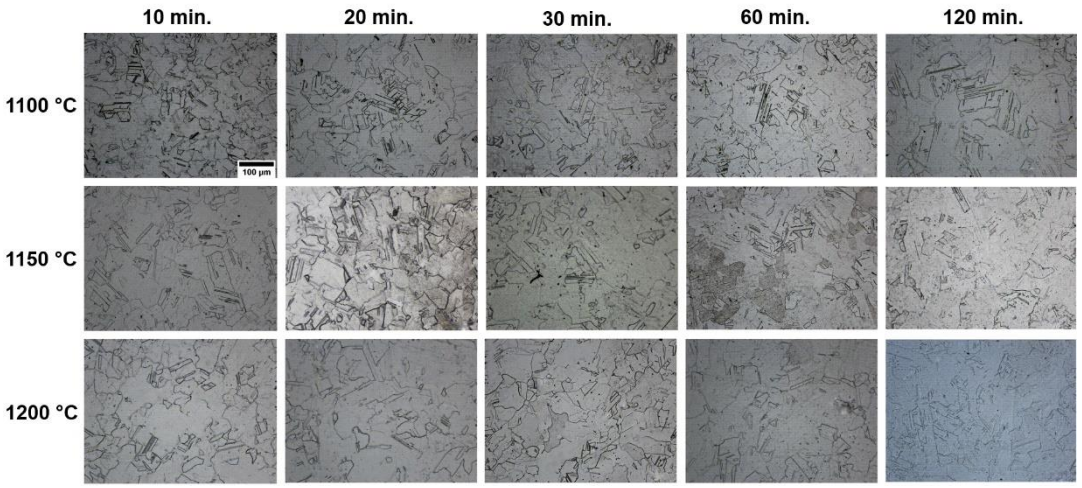

Figure 4.10 OM micrographs of heat-treated and etched ODS IN625 samples, with each row corresponding to temperature and each column corresponding to time.

Recrystallization is evident in all samples, regardless of the heat treatment temperature and duration. An abundance of twin boundaries is observed in each sample, though their prevalence decreases with increasing temperature and time. Grain size increases progressively with extended heat exposure, with the most significant growth occurring in the 1200 °C samples. Inadequate dissolution of secondary phases for the samples heat-treated at 1100 °C restricted the grain growth to a certain extent by grain boundary pinning, leading to a stable hardness change during the heat treatment. The initial decrease in hardness observed between 10 and 30 minutes in the 1150 °C and 1200 °C samples indicates dislocation annihilation, internal stress relief and secondary phase dissolution. This occurs while the solid solution strengthening effect remains absent since the alloy has not yet achieved a uniform solid solution state. Beyond this period, the subsequent increase in hardness suggests that the alloy transitions into a more homogeneous solid solution state, free

from residual stresses introduced by the L-PBF process. In other words, prolonged exposure at these temperatures allows the microstructure to stabilize, overcoming transient softening effects. As the material approaches uniformity, its mechanical properties begin to improve. Additionally, formation of new nano-oxides at elevated temperatures helps hindering grains from further coarsening. Pu et al. stated that the grain coarsening after 1150 °C is due to the complete dissolution of secondary phases and enhanced diffusion of the solute atoms, facilitating the grain growth [210]. Therefore, to promote an effective strengthening without much grain coarsening, a heat-treatment route of 1150 °C for 60 minutes has been chosen for further characterization. Fig. 4.11 shows the SEM micrograph of the ODS alloy solutionized at 1150 °C for 60 minutes. The micron-scale secondary phases correspond to the primary carbides of Hf and Nb, which have greater stability where they dissolve in the matrix at much higher temperatures (i.e., temperatures exceeding 1200 °C) [135].

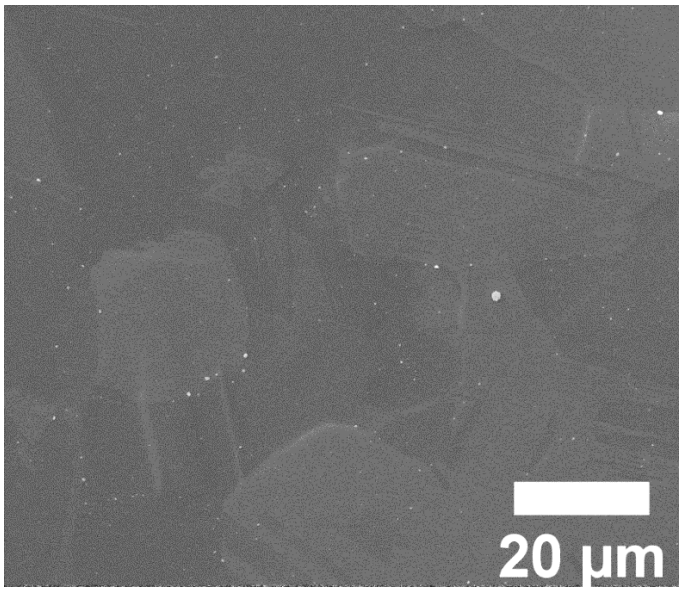

Figure 4.11 SEM micrograph of the ODS sample solutionized at 1150 °C for 60 minutes.

4.3.2 Direct Aging Temperature

Recent studies have shown that DA of AM IN625 results in a significant increase in the mechanical properties compared to conventional heat treatment routes. In one study, Keya et al. used 700, 900 and 1050 °C as DA temperatures for 2, 5 and 10 hours to monitor hardness changes in L-PBF produced IN625, finding a notable increase in hardness at 700 °C for 10 hours [138]. Similarly, Marchese's research selected DA temperatures between 600 and 900 °C, with treatment durations of 2, 8 and 24 hours. The hardness of the AB samples peaked at 700 and 800 °C after 24 hours, although the formation of the deleterious δ phase was observed at 800 °C [137]. Both studies demonstrate that mechanical properties improve with extended DA treatment durations, regardless of the temperature. Ferraresi et al., on the other hand, conducted DA only at 720 °C for 8 hours and achieved superior properties compared to the other heat treatments such as stress relieving, solutionizing alone, or solutionizing followed by aging [211]. According to the recent information, DA temperatures are selected as 700 and 800 °C, while the duration ranges between 2 to 36 hours, as illustrated in Fig. 3.7. The hardness values of the DA alloys, with respect to the duration of the heat treatment is shown in Fig. 4.12.

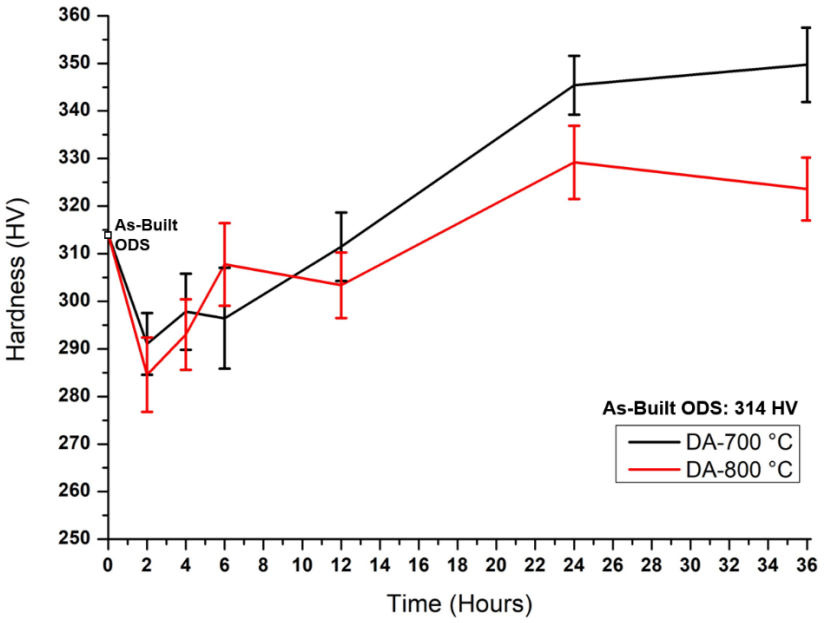

Figure 4.12 The hardness of the AB ODS alloy and DA ODS IN625 from 2 to 36 hours at 700 and 800 °C.

As can be seen from Fig. 4.12, short-term DA at both temperatures leads to a notable decrease in the hardness, probably because of the relief of the residual stresses generated during L-PBF production. Further heat treatment subsequently promotes the formation of strengthening γ″ phase, resulting in an increase in hardness, although it has not yet reached the value of the AB alloy. Between the 4 to 12 hours range, a competitive trend in hardness is observed between samples. However, a decrease in hardness is observed at 700 °C between 4 and 6 hours and at 800 °C between 6 and 12 hours which potentially indicates the onset of phase transformations, as shown in the micrographs in Fig. 4.13. The subsequent increase in hardness after prolonged thermal exposure (i.e., beyond 6 hours at 700 °C and 12 hours at 800 °C) can be attributed to the transformation of initially formed nano-scale γ″ phases into δ phases, decomposition of MC carbides into $M_{23}C_6$-type carbides, and the continued formation of γ″ phases.

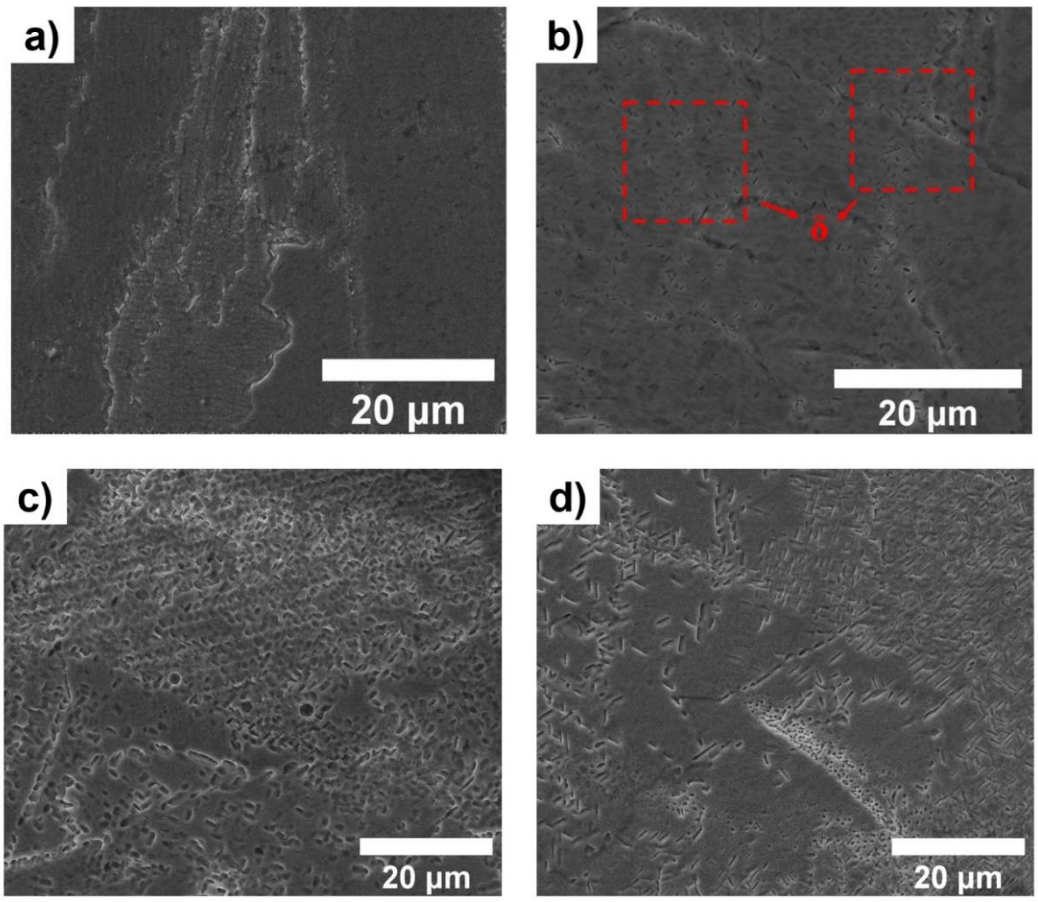

Figure 4.13 SEM Micrographs of DA ODS IN625 at a) 700 °C – 4 h, b) 700 °C – 6h and c) 800 °C – 6 h, d) 800 °C – 12 h.

For samples treated at 800 °C, the initially homogeneous distribution of the secondary-phase networks appears disrupted between 6 and 12 hours. Interestingly, the TTT diagram of AM IN625 does not indicate rapid formation δ phase formation and even Laves phase after around 30 hours. Conversely, the TTT diagram of conventional IN625 indicates δ and even Laves phase formation after around 30 hours. Given the shift of the formation of the δ phase curve in TTT for AM IN625, formation of the Laves phase may have taken place in samples treated at 800 °C, over 24 hours.

An exceptional increase in the hardness is observed after 12 hours at 700 °C and 800 °C, which is consistent with the findings of Marchese et al. However, at 36 hours, hardness decreases at 800 °C, while showing a slight increase at 700 °C [137]. This

limited increase in hardness followed by a decrease at 800 °C, is likely due to the coarsening of the δ and Laves phases. Indeed, high-magnification OM micrographs of the samples, shown in Fig. 4.14, reveal the presence of the interpenetrated δ phase, along grain boundaries and within grains.

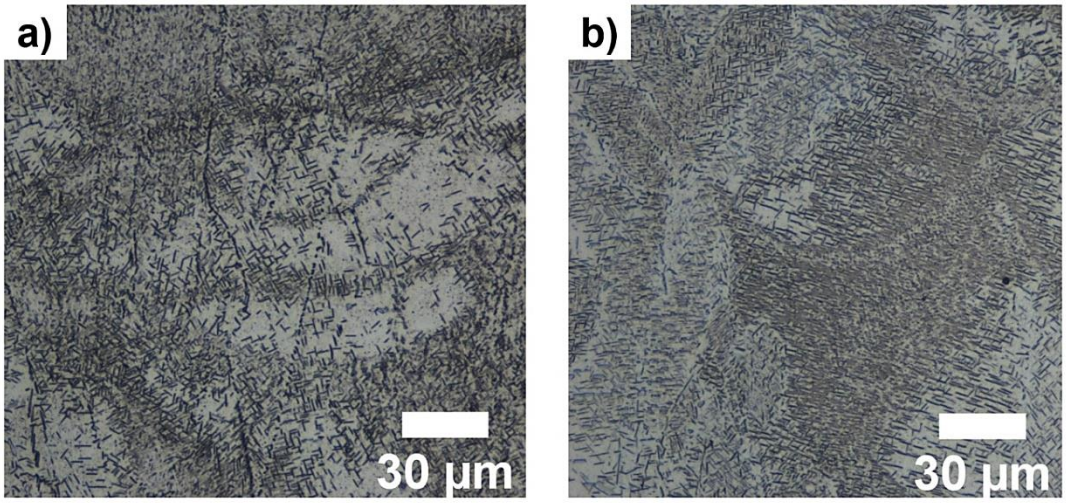

Figure 4.14 OM Micrographs of DA ODS IN625 at a) 800 °C – 24 h and b) 800 °C – 36h.

For 700 °C, 12-, 24- and 36-hour samples come to the forefront due to their relatively higher hardness compared to the other samples. Since δ phase is generally considered detrimental to the properties, a microstructure devoid of this phase is preferable. However, the formation of δ phase is already observed after just 4 hours of DA at 700 °C. To make a well-supported decision on the DA temperature, both OM and SEM micrographs of 12-, 24- and 36-hour samples are shown in Fig. 4.15. In the 12-hour OM micrograph, melt pool boundaries are clearly visible, while they become obscure in the 24- and 36-hour samples. Furthermore, no significant change in the morphology of the grain boundaries is observed throughout these durations.

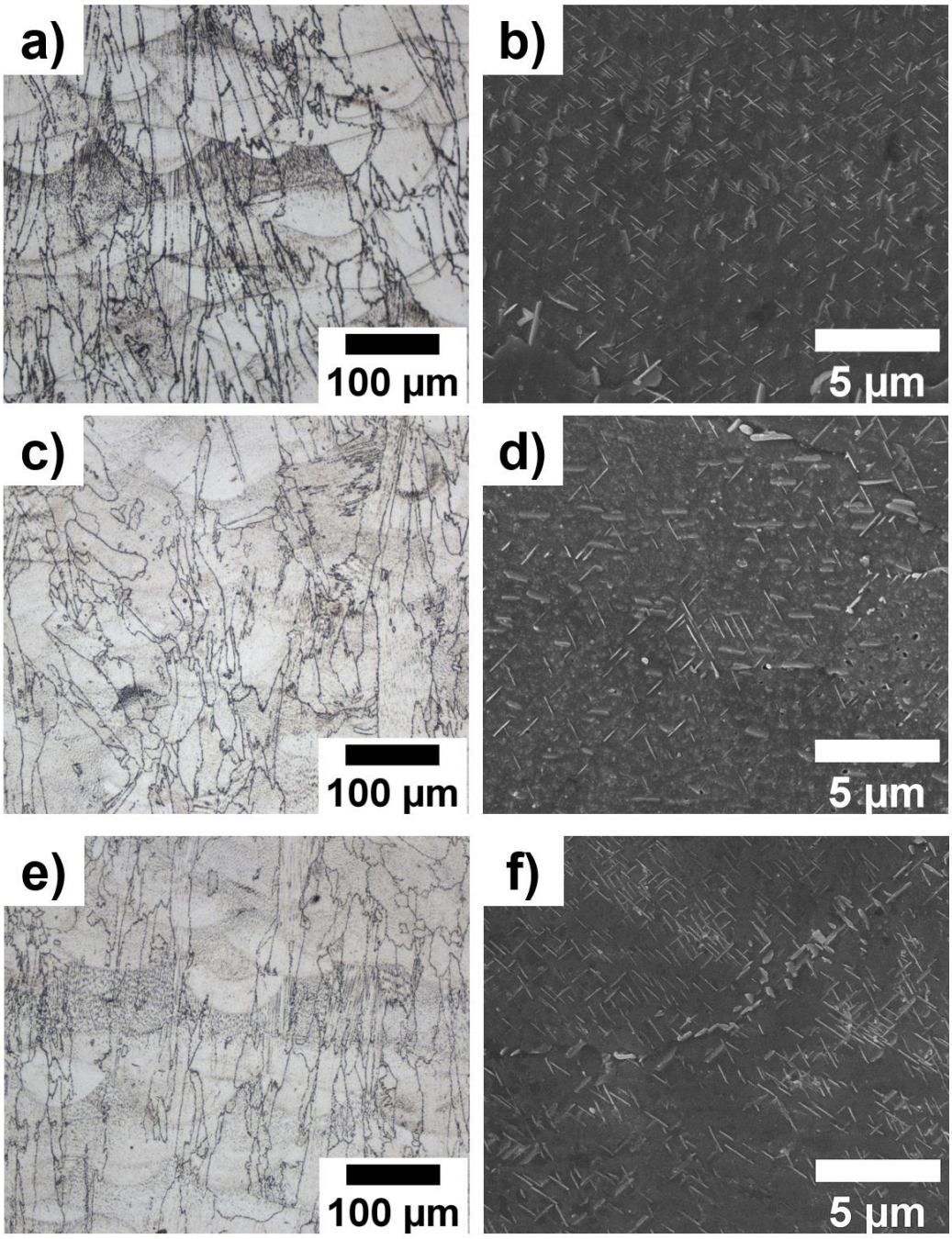

Figure 4.15 OM and SEM Micrographs of DA ODS IN625 at a) and b) 700 °C – 12 h, c) and d) 700 °C – 24 h, e) and f) 700 °C – 36 h.

The SEM micrographs clearly reveal secondary phases formed during the DA. In all samples, micron-sized δ are evident. Surprisingly, the size of δ phases remained fairly consistent across the samples, while mechanical properties improved over

time. Additionally, blocky particles appear in the 24- and 36-hours samples. According to the TTT diagram and existing studies, these particles are likely MC and $M_{23}C_6$ type carbides. Ultimately, following hardness measurements and microstructural analysis, 700 °C for 24 hours was selected as the optimal DA temperature for both STD and ODS alloys. Moreover, solutionizing and aging (SA) temperature for the IN625 alloy has been chosen based on the aforementioned parameters (i.e., 1150 °C for 1h and 700 °C for 24h).

4.4 Microstructural Analysis

4.4.1 Microstructure of As-Built Alloys

SEM micrographs of both STD IN625 and ODS IN625 in as-built (AB) condition, where the BD is specified with an arrow, are shown in Fig. 4.16.

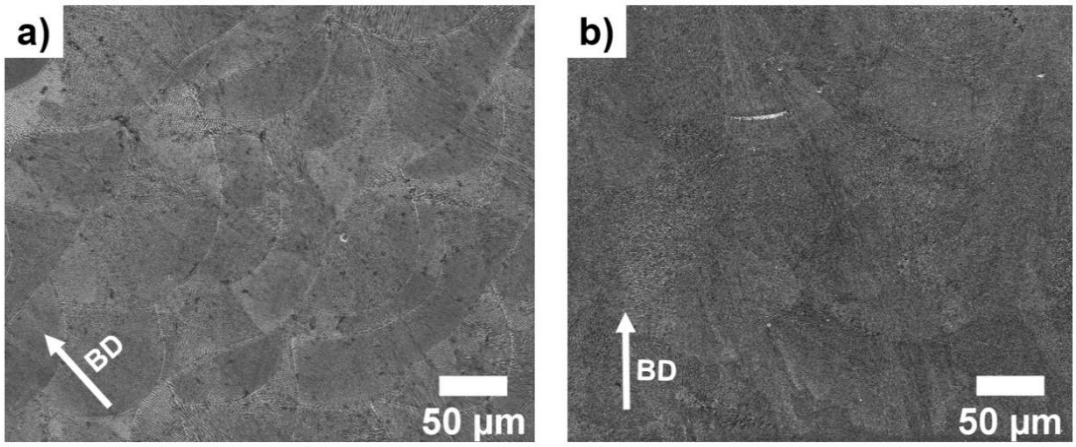

Figure 4.16 SEM micrographs of a) STD and b) ODS IN625 under low magnification.

Both microstructures are characterized by a combination of fine cellular and columnar structures, a common phenomenon in alloys produced by L-PBF. The rapid cooling rates and steep gradients during L-PBF drive the formation of these structures. Sub-micron primary dendrites, along with carbides and Laves phases can also be observed within the cellular regions [99,212]. Moreover, significant Nb and

Mo segregation into the cell boundaries takes place after the L-PBF production of IN625 parts [128,144,145,148,213]. The cell structures of the AB STD and ODS IN625 are depicted in Fig. 4.17. In the micrograph of STD alloy, columnar and cellular structures are apparent and specified in Fig. 4.17a. Besides, melt pool boundaries are highlighted with dotted red lines in the same micrograph.

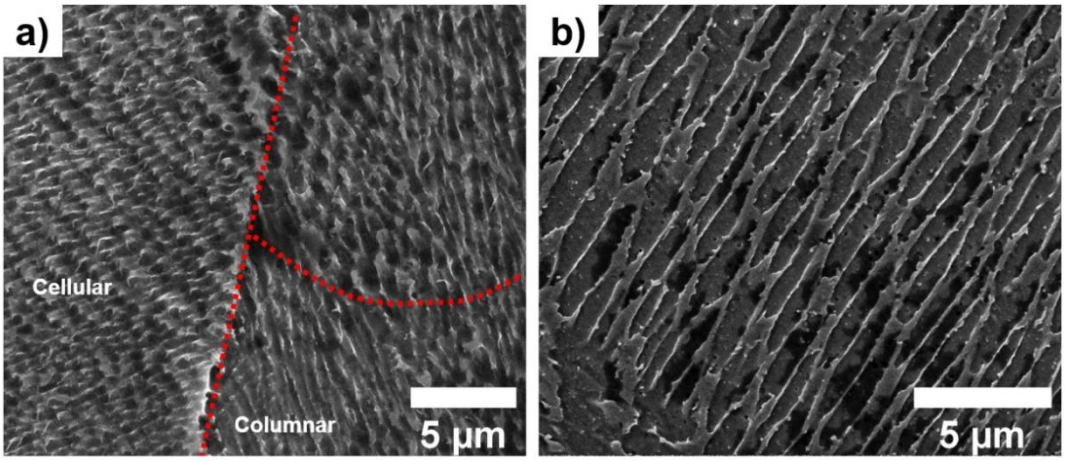

Figure 4.17 SEM micrographs of a) STD and b) ODS IN625 under high magnification, showing cellular and columnar structures.

The micrograph in Fig. 4.18 illustrates the interdendritic sub-micron precipitates in ODS IN625. Distinguishing these precipitates using standard SEM techniques is challenging, as the use of non-conductive bakelite for mounting causes charging effects at higher magnifications during EDX analysis. Nevertheless, they can easily be seen using backscattered electron (BSE) mode in SEM at higher magnifications, provided in Fig. 4.18. The available literature indicates that these features correspond to MC carbides and Laves phases formed during solidification [214,215]. In ODS

IN625, Y-Hf-O oxides are also present, but their definitive identification requires advanced TEM techniques.

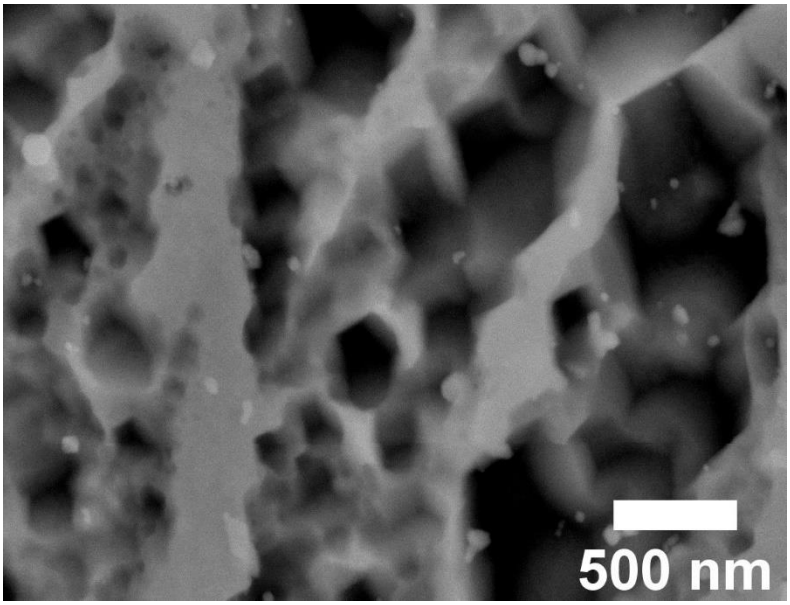

Figure 4.18 BSE SEM micrographs of the ODS IN625 under high magnification, showing interdendritic precipitates.

Fig. 4.19 presents the inverse pole figure (IPF) maps of the AB STD and ODS IN625, with BD indicated by an arrow for both samples. In the AB STD alloy, no obvious preferred orientation is observed, which contradicts with the literature, where most alloys produced by L-PBF show a strong texture along the <100> direction [135,139,145,202]. On the other hand, a slight dominance of the red hues in the IPF map of ODS IN625 infers that there may be a preferred orientation along the {001} plane. This can be confirmed by the pole figures of the alloys for {001}, {101} and {111} planes, respectively (Fig. 4.20). The texture strength of the alloys is quantified as multiple of uniform density (MUD), shown at the top of the color bars. Relatively low MUD values indicate weak grain alignment in the microstructures, and

therefore, it can be inferred that no strong preferred orientation was shown by both alloys.

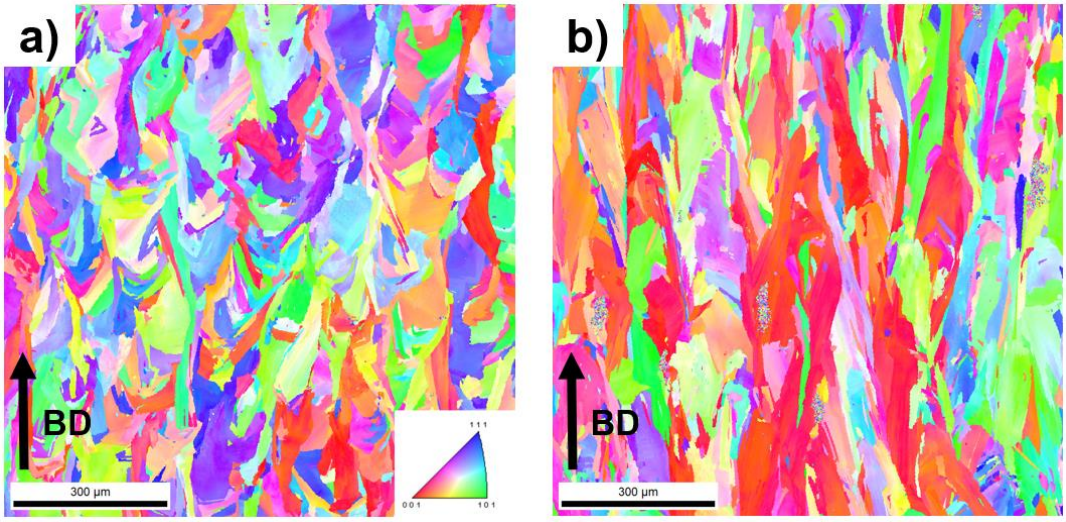

Figure 4.19 IPF maps of AB a) STD and b) ODS IN625.

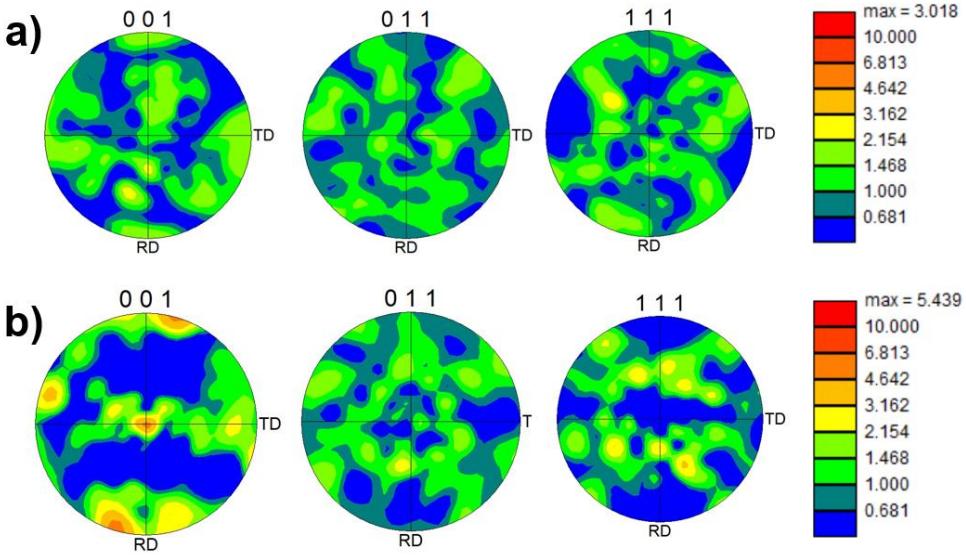

Figure 4.20 Pole figures of AB a) STD and b) ODS IN625 for {001}, {011} and {111} planes.

According to the inlets within the EBSD grain boundary maps shown in Fig. 4.21, both alloys contain a remarkable amount of low angle grain boundaries (LAGB), which are between 2 and 15 degrees. This well aligns with the literature since LAGB are formed by the dislocations, which are generated during rapid solidification in L-

PBF [216]. Besides, a high amount of LAGB also indicates the presence of large residual stresses in the AB samples [217]. Based on these maps, the average grain sizes of the AB STD and ODS alloys, excluding edge grains, were found to be 12.1 μm and 10.9 μm, respectively. This suggests a slight grain refinement effect attributable to the insertion of nano-oxides.

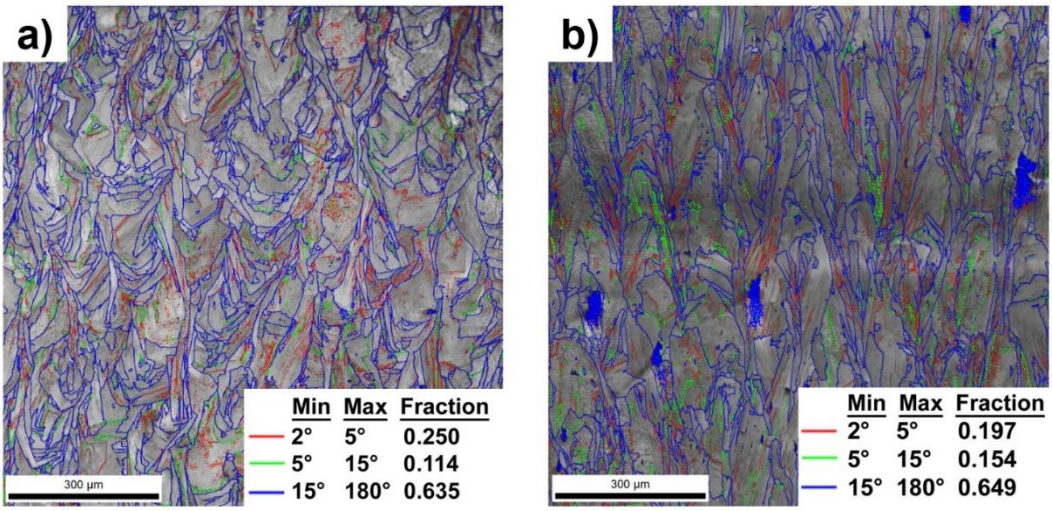

Figure 4.21 EBSD grain boundary maps of AB a) STD and b) ODS IN625, with the frequency of low and high-angle grain boundaries.

The high amount of residual stresses in both samples can also be examined by the Kernel average misorientation (KAM) maps, where dislocation substructure and stored energy in the samples can be observed [218]. As can be seen from the inlets of Fig. 4.22a and 4.22b, ODS IN625 has a slightly lower KAM value, as the fraction between zero and one is higher than that of STD alloy. In other words, the dominance of the green color corresponds to larger KAM values in the STD alloy, which indicates that strain energy and dislocation density are higher.

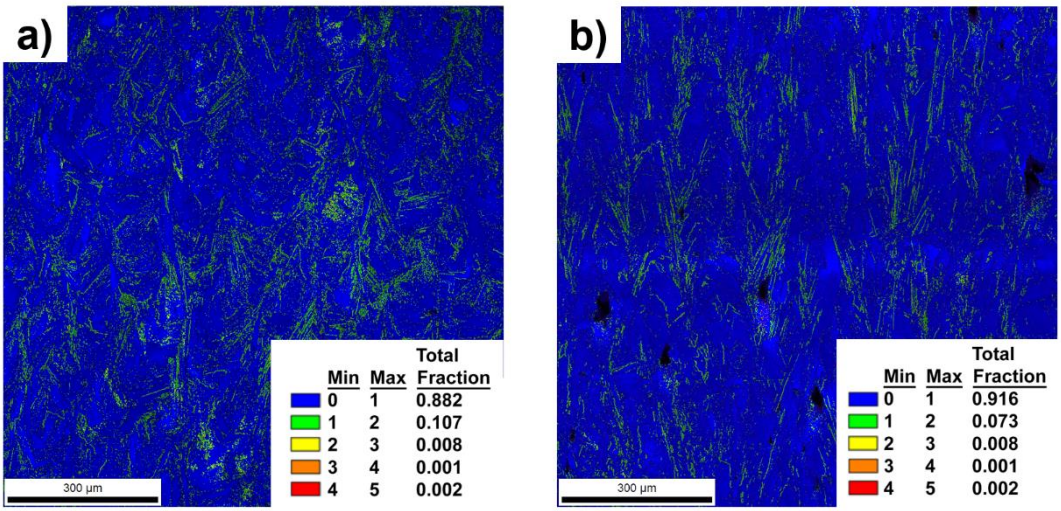

Figure 4.22 KAM maps of AB a) STD and b) ODS IN625 alloys.

Fig. 4.23 provides the SEM micrographs of the coarse second-phase particles in the ODS IN625, with their chemical composition from point EDX. The particle sizes of these second-phase particles are around 2 µm, and their shape is almost spherical. The elemental percentage of the precipitates corresponds to the non-stoichiometric Y-Hf-O compounds.

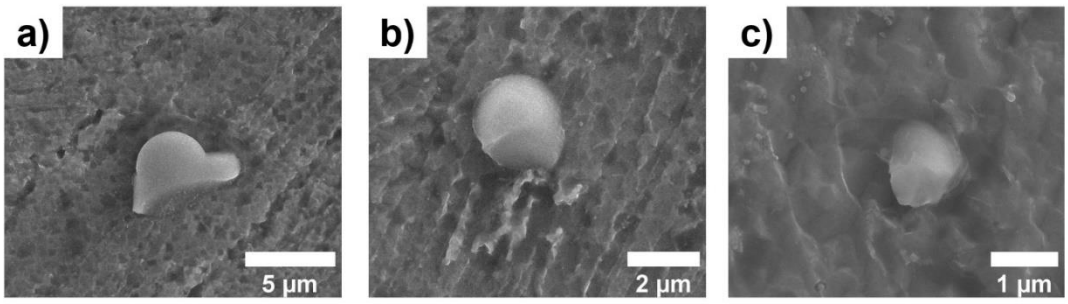

Element	Wt%
C	9.65
O	7.86
Nb	1.11
Mo	2.13
Cr	8.50
Ni	25.9
Hf	10.1
Y	34.8

Element	Wt%
C	4.19
O	8.26
Nb	2.96
Mo	2.82
Cr	8.46
Ni	22.8
Hf	11.6
Y	38.9

Element	Wt%
C	6.02
O	3.63
Nb	3.56
Mo	5.71
Cr	16
Ni	45.1
Hf	4.5
Y	15.5

Figure 4.23 SEM micrographs showing the presence and chemical composition of AB ODS IN625 alloy.

To monitor the presence of the nano-oxides, several TEM micrographs of the AB ODS IN625 are captured. Fig. 4.24 presents the bright-field transmission electron microscopy (BFTEM) micrograph of the AB ODS alloy, where the microstructure is characterized by cellular dislocation formations near nanoparticles. Quantitative analysis indicates that the average particle size of the nano-oxides was found to be 30 ± 18 nm, with particle size distribution skewed toward the range between 10 and 30 nm, as illustrated in Fig. 4.25.

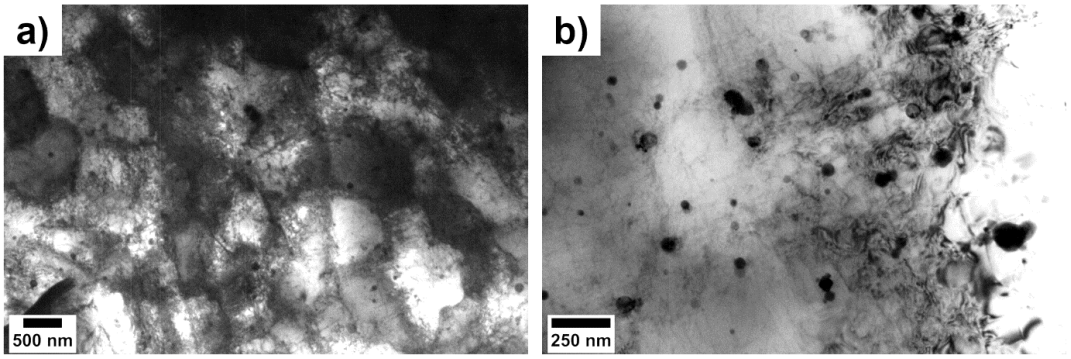

Figure 4.24 BFTEM micrographs of ODS IN625 in AB condition, demonstrating the presence of nano-oxides around a) dislocation cells and b) the matrix.

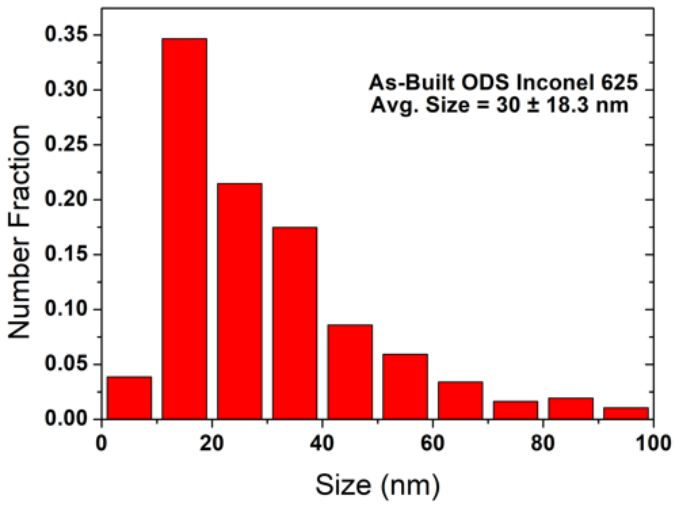

Figure 4.25 Histogram of the particle sizes of nano-oxides with their number fraction and average size.

The compositional analysis of the ODS IN625 was carried out on a bigger scale via high-angle annular dark-field scanning transmission electron microscopy (HAADF-STEM) and EDX. A HAADF-STEM micrograph was taken and four different sections were selected for compositional analysis, as shown in Fig. 4.26. The nano particles were determined to be Y-Hf-O and Y-Hf-(Ti)-O, while the composition of the no particle containing area is compatible with that of the matrix of the IN625. A detailed information of the elemental compositions of the selected sections have been provided at the Table 4.5.

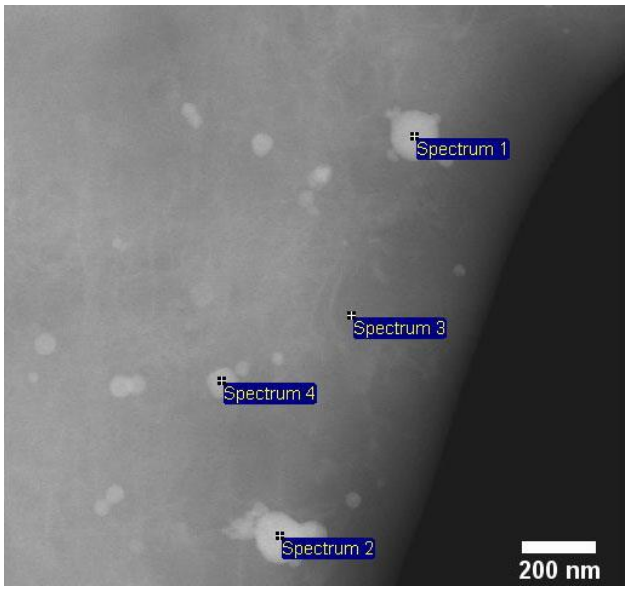

Figure 4.26 HAADF-STEM micrograph of the ODS IN625 in AB condition, with points to be analyzed.

Table 4.5 STEM and point EDX analysis of the selected spectrums with their elemental amount in wt%.

Spectrum	Y	Hf	O	Ni	Ti	Cr	Mo	Nb
1	15.7	4.5	13.5	38.5	-	13.7	7.1	3.0
2	9.1	11.9	10.3	42.1	-	12.9	7.9	4.2
3	-	-	3.9	62.2	0.6	17.9	8.0	6.2
4	9.7	6.1	9.2	43.8	0.3	15.9	9.4	4.3

4.4.2 Microstructure of the Direct Aged Alloys

High-magnification OM micrographs of DA ODS IN625 are shown in Fig. 4.27. The remnants of the melt pool boundaries near the grain boundaries are somehow visible in Fig. 4.27a, while discontinuous grain boundaries are apparent in Fig. 4.27b. The discontinuity in the grain boundaries could indicate the presence of second-phase particles at these locations.

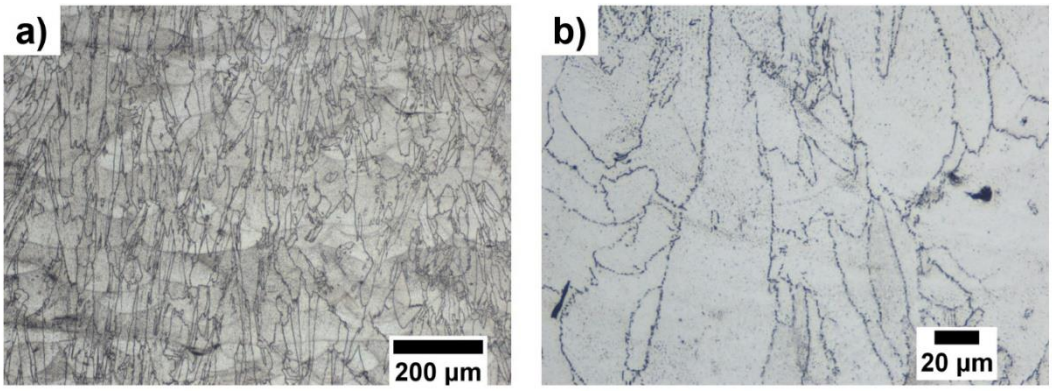

Figure 4.27 a) Low and b) high magnification OM micrograph of ODS IN625 in DA condition at 700 °C for 24 hours.

The melt pool boundaries from the L-PBF process are more clearly visible in the SEM micrographs provided in Fig. 4.28, where they are highlighted with dotted red lines in Fig. 4.28b.

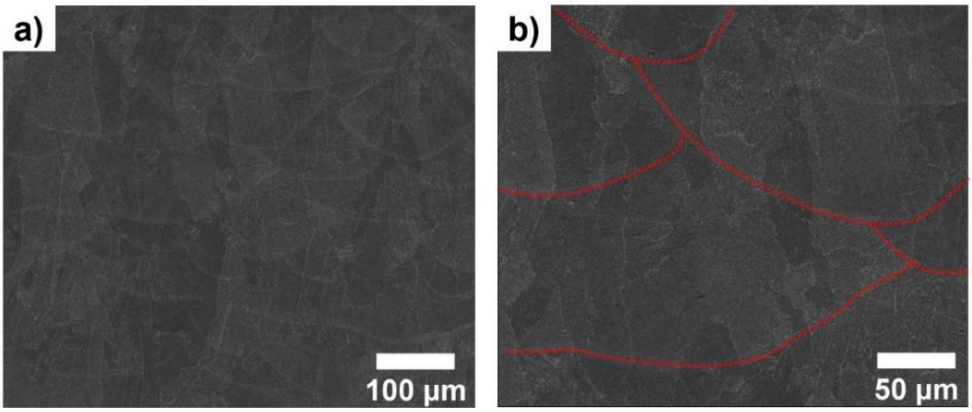

Figure 4.28 SEM micrograph of DA ODS IN625, showing the melt pool boundaries.

At higher magnifications, SEM images reveal the presence of the second phase particles, both intergranular and transgranular in both STD and ODS alloys. SEM micrographs showing those particles for both direct-aged alloys are provided in Fig. 4.29.

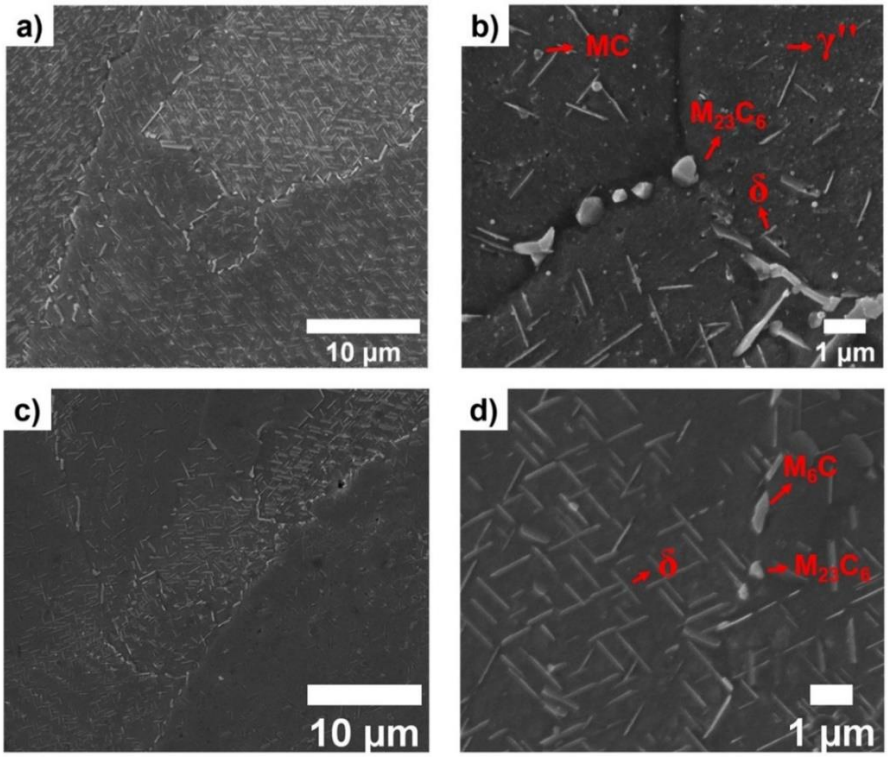

Figure 4.29 SEM micrograph of DA a), b) ODS IN625 and c), d) STD IN625 alloys, showing the second-phase particles and their distribution.

In both alloys, the particles within the grains could be micron-sized, platelet-shaped δ phases. As discussed in the section 2.4.3 briefly, the formation of δ phase is quite peculiar under such conditions due to the fact that δ phase formation is generally observed after hundreds of hours in wrought components. This oddity has been reported in several L-PBF studies of IN625, where the formation of δ phases in shorter times is observed, and it is attributed to the severe segregation of Nb and Mo [143,145,194]. Local increases in Nb concentration facilitate and accelerate the formation of δ phases, and a new TTT diagram is used to observe this process (Fig.

2.20) [147,148]. The segregation of the Mo and Nb to certain regions of the AB ODS alloy is demonstrated by the EDX mapping, shown in Fig. 4.30.

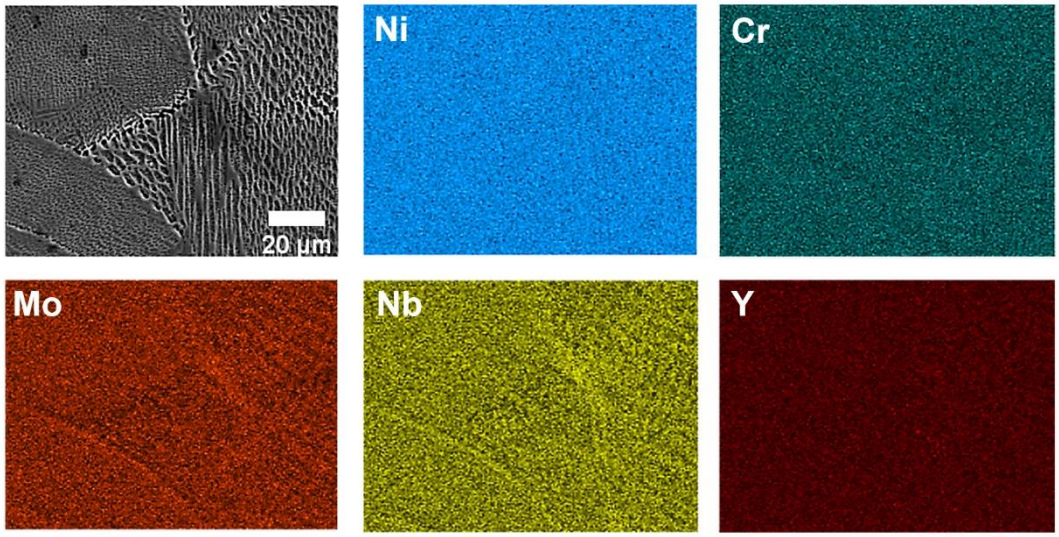

Figure 4.30 SEM - EDX map of the ODS alloy in AB condition.

The presence of irregularly-shaped second-phase particles with a chain-like formation is a commonly observed behavior of IN625 aged at intermediate temperatures and these particles are $M_{23}C_6$ carbides, transformed from primary MC carbides according to the following equations [64,130,219].

$$MC + \gamma \rightarrow M_{23}C_6 \quad \text{(Eq. 4.1)}$$

$$MC + \gamma \rightarrow M_{23}C_6 + \delta \quad \text{(Eq. 4.2)}$$

In Fig. 4.31, such formations as well as severe Nb and Mo segregation can clearly be seen.

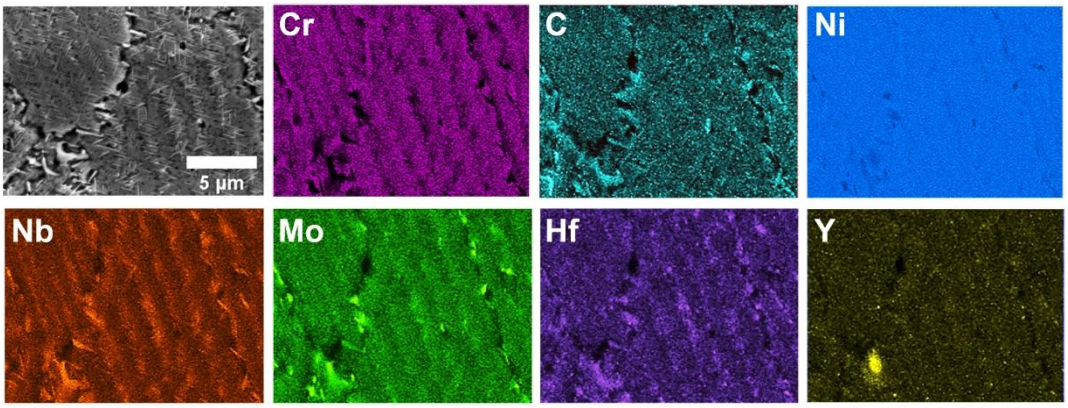

Figure 4.31 SEM - EDX map of the DA ODS alloy.

4.4.3 Microstructure of the Solutionized and Aged Alloys

The OM images of the as-received and SA heat-treated conventionally produced rod is shown in Fig. 4.32. Since it is in hot rolled and heat-treated condition, as-received microstructure is characterized by micron-size grains.

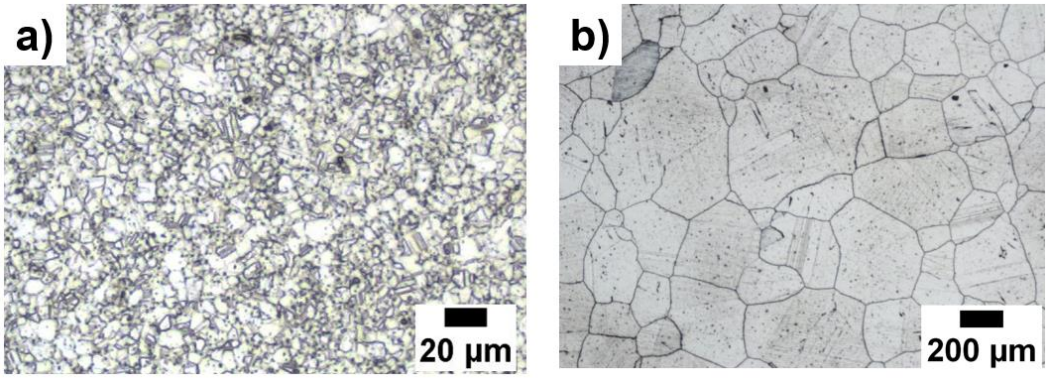

Figure 4.32 a) High magnification OM image of as-received IN625 rod and b) low-magnification OM image of SA IN625 rod.

Solutionizing at 1150 °C led to significant grain growth, with the SA IN625 rod showing an average grain size of 208 µm, the largest among the alloys. As shown in Fig. 4.33c, the grain size distribution in this alloy appears to be relatively bimodal,

featuring some fine grains beside larger ones. In hot-rolled IN625, grain growth becomes faster at solutionizing temperatures exceeding 1100 °C, below which it is sluggish and the initial grain size does not change considerably [209]. This is attributed to the fact that dissolution of carbide phases within the microstructure is slow and they hinder the growth of grains during solutionizing heat treatment [220]. On the other hand, dissolution of these phases took place above 1100 °C and facilitate the grain growth. In addition, small grain size and high interfacial area in as-received state (Fig. 4.32a) drove the accelerated nucleation.

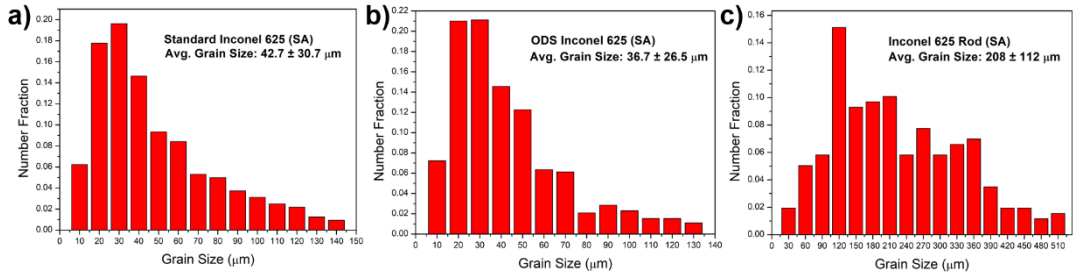

Figure 4.33 Histogram of the grain sizes with their number fraction and average grain size for a) STD IN625, b) ODS IN625 and c) IN625 rod.

EDX mapping, combined with the SEM micrograph of the IN625 rod in SA condition shown in Fig. 4.34, reveals secondary particles both at grain boundaries and within grains. At the grain boundaries, chains of blocky carbides are evident, with higher Cr content indicating the presence of $M_{23}C_6$ carbides. On the other hand, EDX mapping highlights blocky TiC and NbC particles within the grains. The absence of Laves phase and M_6C type carbides is confirmed by the lack of significant Mo and Fe accumulation in the microstructure. SEM micrographs of the SA rod at high magnification also revealed nano-sized γ″ precipitates (Fig. 4.35b).

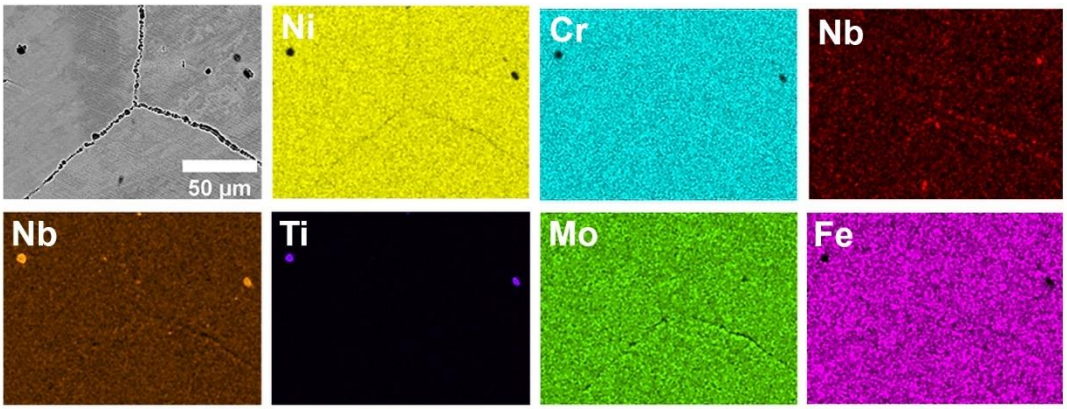

Figure 4.34 SEM - EDX map of the SA IN625 rod.

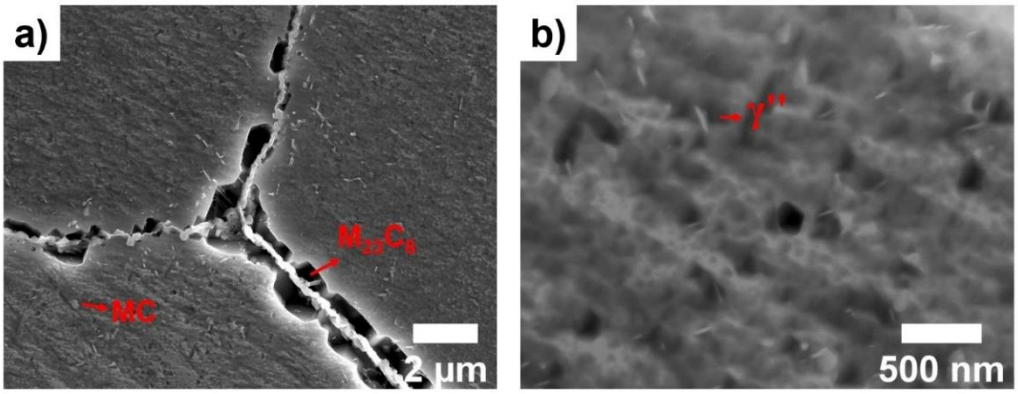

Figure 4.35 High magnification SEM micrographs of IN625 rod from a) grain boundary junction and b) within grain.

The OM images of the SA heat-treated STD and ODS alloys produced by L-PBF are shown in Fig. 4.36. In both alloys, the grain size is much smaller than that of the SA rod, as confirmed by the plots in Fig. 4.33a and 4.33b. The grain size distribution in both the STD and ODS alloys appears to be unimodal. While larger grains are present, smaller grains dominate in both alloys and play a decisive role in determining the average grain size. Quantitatively, the average grain size was measured as 42.7 µm for the STD alloy and 36.7 µm for the ODS alloy. The smaller average grain size in the ODS alloy is attributed to the grain refinement effect of the nano-oxide dispersion within the microstructure. In IN625 alloys produced by AM methods, the primary driving force for static recrystallization is the residual stresses

built-up during the manufacturing process. Since these residual stresses vary depending on the specific locations within the material, such as in melt pools and within cellular structures, a uniform grain size has not been achieved in either alloy [135].

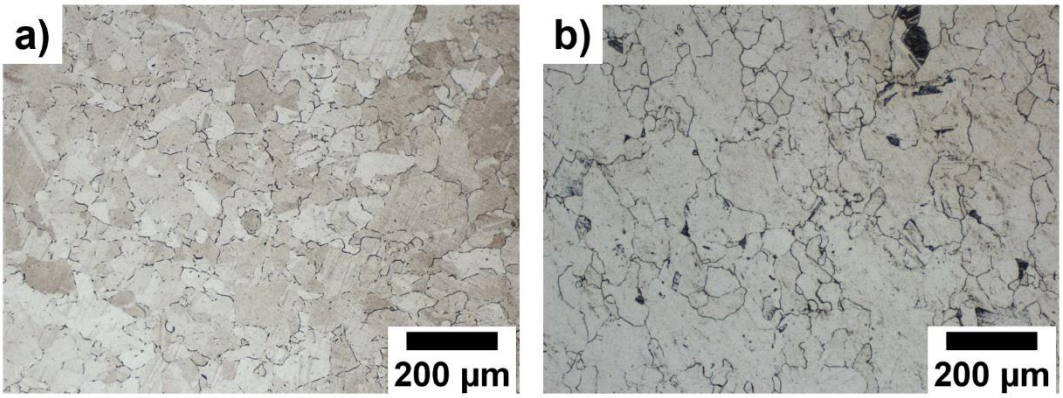

Figure 4.36 OM micrographs of SA a) STD and b) ODS IN625.

In SA STD and ODS IN625 alloys, a mixture of carbides, including MC, M_6C and $M_{23}C_6$ types, is observed at grain boundaries. Specifically, the higher Mo content corresponds to M_6C carbides, while high Nb contents indicate the presence of MC-type carbides. At the grain boundaries and around M_6C-type carbides, presence of Cr indicates the formation of $M_{23}C_6$-type carbides, as it can take place from the dissolution of MC and M_6C type carbides. EDX mapping of the ODS alloy reveals the presence of the δ phase at grain boundaries, as shown in Fig. 4.37. This indicates that Nb and Mo segregation persists despite the solutionizing heat treatment, which facilitates the formation of δ phases. Moreover, the presence of M_6C type carbide and HfC could be concluded from the accumulation of Mo and Hf at certain regions.

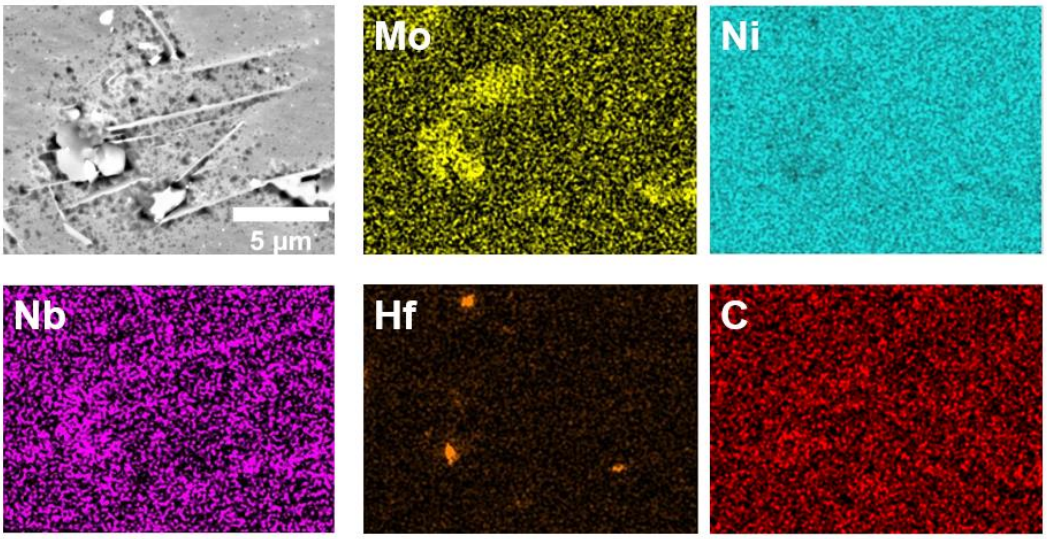

Figure 4.37 SEM - EDX map of the SA IN625 rod.

4.5 Mechanical Properties

4.5.1 Hardness Values

Prior to conducting tensile tests at room temperature (RT), the hardness of the AB, DA and SA alloys has been measured using the $HV_{0.5}$ scale. The hardness values of STD and ODS IN625 alloys in AB condition were found to be 298 ± 6 and 314 ±8 HV, respectively. An increase in hardness by 5% has been observed in the ODS alloy. This infers that the formation of nano-oxides within the matrix is effective in increasing the mechanical properties. The hardness of the STD and ODS IN625 alloys in DA condition were found to be 315 ± 10 and 345 ± 6 HV, respectively. DA has resulted in a significant increase in the hardness of both alloys with respect to the AB condition, by 6% in the STD alloy and by 10% in the ODS alloy. Moreover, the hardness difference between DA STD alloy and ODS alloy is 10%, proving the positive effect of the presence of second phases and nano-oxides in the mechanical properties.

SA, on the other hand, leads to a decrease in the hardness in both alloys, especially in the IN625 rod. The hardness of the as-received rod was 283 ± 6 HV, while the hardness of SA rod was measured as 239 ± 12 HV. The significant drop in hardness has been attributed to the remarkable grain coarsening after SA treatment. On the other hand, the hardness of the SA STD and ODS IN625 alloys were found to be 283 ± 8 and 302 ± 7 HV, respectively, despite the presence of δ phase. Although the elimination of detrimental phases and the formation of γ″ phase is associated with improved hardness in IN625 alloys, the hardness of the conventionally produced IN625 rod was observed to be lower than that of the L-PBF produced samples. This discrepancy can be attributed to the finer microstructural features, as well as the existence of different phases. Although the grain size was preserved to a certain extent, SA treatment in both additively manufactured alloys resulted in inferior hardness values compared to the AB and DA conditions. Nevertheless, ODS has led to an increase in hardness by 7% in this condition, similar to the other treatments. The hardness values of all specimens were summarized in Fig. 4.38.

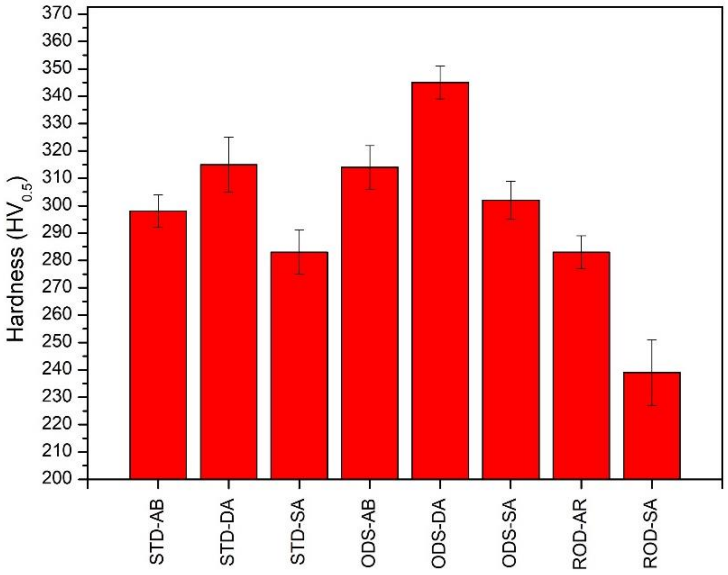

Figure 4.38 The hardness values measured for alloys in AB, DA and SA conditions, as well as conventionally-produced as-received (AR) rod.

4.5.2 Tensile Test Results at Room Temperature

Table 4.6 lists the averaged values of yield strength, tensile strength, elastic modulus and strain at rupture along with the hardness values of the AB alloys after the RT tensile testing. At RT, ODS leads to a slight enhancement in the mechanical properties, as the observed differences are relatively small. Quantitatively, the increase in each mechanical property in ODS IN625 were around 2%. Furthermore, the measured hardness values and mechanical properties at RT are parallel to the standard hardness-strength conversion chart [217]. Since as-received rod has undergone a specific heat treatment and hot rolling, it has a distinct microstructure and different mechanical properties compared to AB IN625, which are not reflective for this study. Thus, their tensile properties were omitted in this case and will only be discussed in the SA condition.

Table 4.6 The average values of the mechanical properties for STD and ODS IN625 in AB condition at RT.

Property	**STD IN625**	**ODS IN625**
Elastic Modulus (GPa)	167.0 ± 4	175.3 ± 10
Yield Strength (MPa)	630.1 ± 15	638.0 ± 6
Tensile Strength (MPa)	871.4 ± 10	896.4 ± 9
Strain at Rupture (%)	41.9 ± 3	43.3 ± 3
Hardness ($HV_{0.5}$)	298 ± 6	314 ± 8

For DA, the averaged tensile properties determined from after tensile tests along with the hardness values are listed in Table 4.7. Analogous with the hardness measurements, a remarkable increase in strength was observed for both DA alloys, which aligns well with the previous studies pertaining to the DA of L-PBF produced IN625 alloys [211]. However, except the hardness values, the mechanical properties of both alloys remain nearly identical at RT. Somehow lower values in tensile and yield strength, compared to the available literature, may be linked to the formation

of the δ phases in both conditions, which has not been reported in previous works [137,138,211].

Table 4.7 The average mechanical properties of STD and ODS IN625 in DA condition at RT.

Property	**DA STD IN625**	**DA ODS IN625**
Elastic Modulus (GPa)	192 ± 2	192 ± 3
Yield Strength (MPa)	701 ± 3	705 ± 9
Tensile Strength (MPa)	1003 ± 10	1005 ± 11
Strain at Rupture (%)	39.3 ± 1	37.8 ± 2
Hardness ($HV_{0.5}$)	315 ± 9	345 ± 6

Lastly, the tensile properties of the SA conventionally produced rod and SA additively manufactured alloys, along with their hardness values, are presented in Table 4.8. The impact of ODS is particularly apparent in this case, as the yield strength of the SA ODS alloy surpasses that of the SA STD alloy and SA rod by 75% and 90%, respectively. Additionally, ODS IN625 has 32% higher tensile strength compared to the rod, while the improvement relative to the STD alloy is not so pronounced, by 5%. Similar to the hardness measurements, the conventionally produced rod demonstrated inferior mechanical properties, which can be attributed to its coarse-grained structure and insufficient strengthening by secondary precipitates. Moreover, despite their fine-grained structure, the ductility of the STD alloy is superior to that of the rod and ODS alloy. This can be attributed to the fact that strengthening by Orowan mechanism at RT is operative in the ODS alloy, resulting in a decrease in the ductility [221]. Overall, mechanical properties of each alloy at RT, along with their representative stress vs. strain curves, are demonstrated in Fig. 4.39 and Fig. 4.40, respectively.

Table 4.8 The average mechanical properties of STD, ODS IN625 and IN625 ROD in SA condition, at RT.

Property	**SA STD IN625**	**SA ODS IN625**	**SA IN625 ROD**
Elastic Modulus (GPa)	211.6 ± 3	200.8 ± 1	200.8 ± 3
Yield Strength (MPa)	401.4 ± 4	703 ± 14	333.8 ± 3
Tensile Strength (MPa)	879.3 ± 6	930 ± 28	699.1 ± 11
Strain at Rupture (%)	60.0 ± 3	41.9 ± 3	37.2 ± 3
Hardness ($HV_{0.5}$)	283 ± 8	302 ± 7	239 ± 12

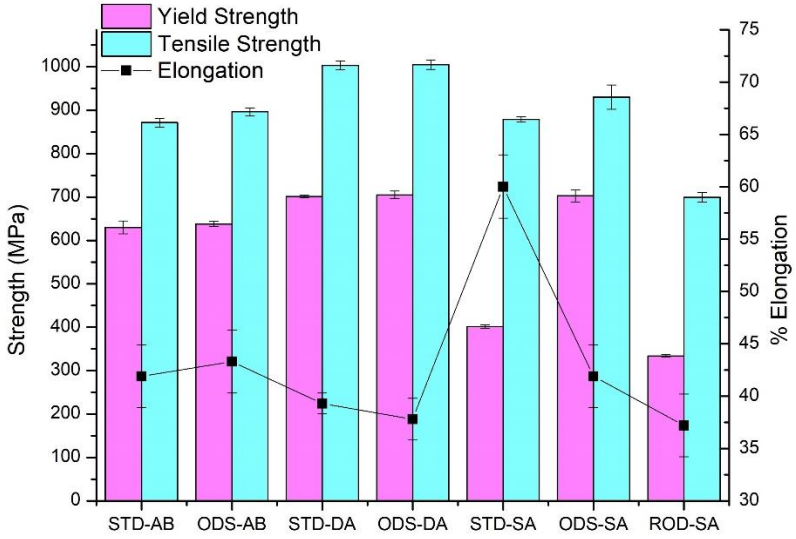

Figure 4.39 Mechanical properties of STD and ODS IN625, in AB, DA and SA conditions, and conventionally produced rod in SA condition, at RT.

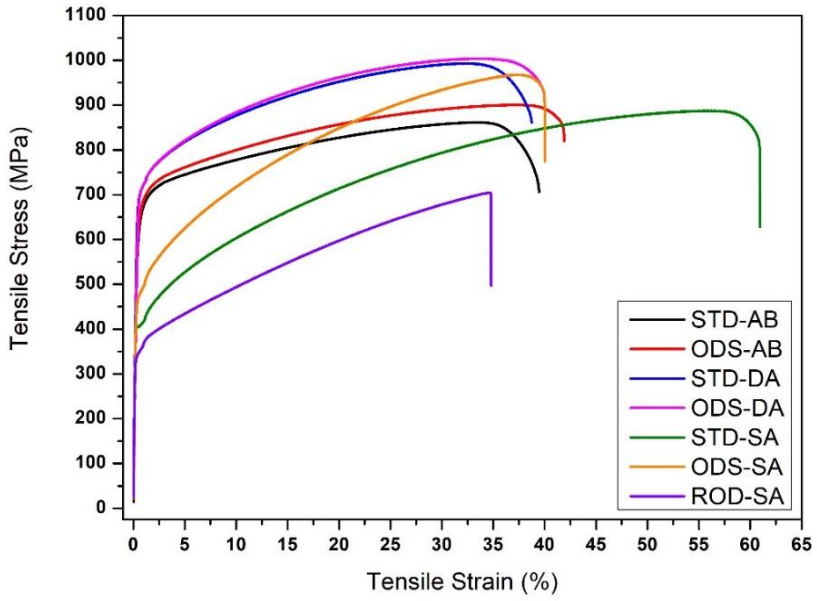

Figure 4.40 Stress vs. strain diagram for STD and ODS IN625, in AB, DA and SA conditions, and conventionally produced rod in SA condition, at RT.

4.5.3 Tensile Test Results at Elevated Temperature

Table 4.9 lists the averaged values of yield strength, tensile strength, elastic modulus and strain at rupture along with the hardness values of the AB alloys after the tensile test at 700 °C.

Table 4.9 The average values of the mechanical properties for STD and ODS IN625 in AB condition at 700 °C.

Property	**STD IN625**	**ODS IN625**
Elastic Modulus (GPa)	119.6 ± 6	113.4 ± 11
Yield Strength (MPa)	501.6 ± 4	517.5 ± 6
Tensile Strength (MPa)	560.9 ± 20	621.4 ± 20
Strain at Rupture (%)	12.1 ± 2	21.8 ± 2

A decrease in mechanical properties as compared to RT values was observed, as expected. Specifically, the tensile strength of STD and ODS IN625 decreased by

36% and 30%, respectively. Moreover, a ductility loss of around 70% was observed for STD alloy, while ODS IN625 experienced a 49% reduction in ductility. However, the effect of ODS on strength and ductility improvement was more prominent at 700 °C, as compared to RT, especially ductility is almost doubling that of STD IN625. In fact, ODS IN625 defies the traditional strength and ductility tradeoff, where the increase in strength is often compensated by a decrease in ductility. This phenomenon can be partially explained by the addition of Hf to the microstructure [184]. Yu et al. attributed this simultaneous increase in both strength and ductility to the high oxygen affinity of Hf, in which oxygen enrichment at the grain boundaries is decreased through the formation of nano-oxides [222]. The depletion of oxygen at grain boundaries improves the grain boundary adhesion and results in enhanced ductility at elevated temperatures [223].

Table 4.10 lists the high temperature average mechanical properties of DA STD and ODS IN625 alloys at 700 °C. A slight improvement in mechanical properties have been observed for both alloys. Specifically, a simultaneous increase in the tensile strength and ductility is seen for both STD and ODS alloys as compared to their AB counterparts. The tensile strength of the DA STD alloy is 8% greater than that of the AB STD alloy, while the tensile strength of DA ODS IN625 alloy exceeds that of the AB ODS alloy only by 4%. On the other hand, the yield and tensile strengths of STD and ODS IN625 is very close as in the case of the tests performed at RT.

Table 4.10 The average mechanical properties of STD and ODS IN625 in DA condition at 700 °C.

Property	**DA STD IN625**	**DA ODS IN625**
Elastic Modulus (GPa)	109.9 ± 8	106.1 ± 15
Yield Strength (MPa)	546.8 ± 3	560.1 ± 10
Tensile Strength (MPa)	632.2 ± 20	654.8 ± 26
Strain at Rupture (%)	15.0 ± 1	23.9 ± 2

Table 4.11 lists the high temperature average mechanical properties of the SA rod, along with those of the STD and ODS IN625 alloys, highlighting the pronounced effect of ODS as in the case of the RT tests. The ODS alloy demonstrates a significant improvement, with tensile and yield strengths reaching 565 MPa and 307 MPa, respectively. Specifically, the tensile strength of the ODS alloy is 55% higher than that of the SA rod and 15% higher than the STD alloy. Furthermore, the ODS alloy achieves improved strength and ductility compared to the STD alloy, confirming the beneficial impact of nano-oxide additions on the microstructure. The SA rod, however, shows the highest elongation at rupture, attributed to its larger grain size, which also contributes to its lower yield strength.

Table 4.11 The average mechanical properties of STD, ODS IN625 and IN625 ROD in SA condition at 700 °C.

Property	**SA STD IN625**	**SA ODS IN625**	**SA IN625 ROD**
Elastic Modulus (GPa)	120.4 ± 3	124.9 ± 6	114.9 ± 5
Yield Strength (MPa)	266.2 ± 3	306.9 ± 1	197.8 ± 3
Tensile Strength (MPa)	509.8 ± 26	565.2 ± 25	492.3 ± 29
Strain at Rupture (%)	26.2 ± 2	34.8 ± 3	67.1 ± 3

The stress-strain curve of the SA alloys at 700 °C, shown in Fig. 4.41, attracts special interest due to the observed serrated flow which is a common unstable plastic deformation behavior referred to as the Portevin-Le Chatelier (PLC) effect and caused by dynamic strain aging (DSA) [224]. This phenomenon occurs due to the repeated pinning and unpinning of mobile dislocations by diffusing solute atoms, the formation and shearing of precipitates, the development of shear bands, and the occurrence of stacking faults [225]. Depending on the fluctuation pattern in the stress vs. strain curve, serrations are classified as different types from A to E. While serration types A, B and C are typically observed in many alloy systems, type D and E are specific to a limited number of alloys [226,227]. Type A serrations manifest themselves as abrupt rise and drop below the regular flow curve pattern. This is

attributed to the repeated formation of deformation bands from one and the movement along the gauge length. While the stress rise corresponds to the propagation of the bands, the stress drop means the nucleation of a new band [228]. Type B serrations are characterized by small oscillations along the overall flow curve, resulting from the dynamic strain aging (DSA) of moving dislocations within deformation bands. Type C serrations, on the other hand, are marked by abrupt drops in stress from the steady flow curve. These typically occur at elevated temperatures and are attributed to dislocation unlocking [226,228]. As shown in Fig. 4.41, all the alloys exhibit Type B and C serrations, a behavior commonly observed in IN625 variants [229]. The amplitude of the serrations for SA alloy is approximately 10 MPa, while in AB and DA conditions it is around 20 MPa.

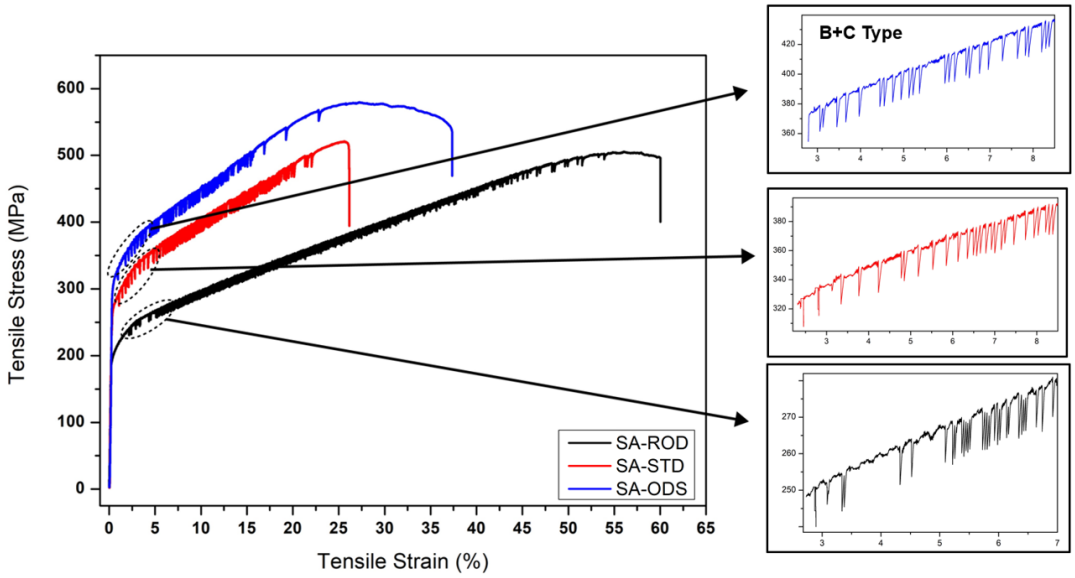

Figure 4.41 Stress vs. strain diagram for conventionally produced rod, STD and ODS IN625 in SA condition at 700 °C.

Serrated flow due to DSA is known to affect metals adversely, leading to reduced ductility and shorter fatigue life [230]. In conventionally manufactured alloys, this behavior is attributed to their equiaxed microstructure and the relatively uniform distribution of elements throughout the matrix. In contrast, the complex microstructures of the AB and DA alloys result in a more stable plastic flow, with no serrated behavior observed in these samples. Beese et al. highlighted the absence

of DSA in AM IN625 and attribute this to its unique dendritic structure, which features microsegregation, sub-micron carbides, and Laves phases [214]. On the atomistic scale, DSA involves the temporary pinning and depinning of mobile dislocations by the diffused solute elements (e.g., Mo and C) [231]. Despite showing better flow characteristics, SA heat-treated and additively manufactured IN625 also tends to exhibit DSA due to the dissolution of second phases, with the activation energy for DSA being influenced by the diffusion of carbon atoms at elevated temperatures [214,230]. Overall, mechanical properties of each alloy at 700 °C, along with their representative stress vs. strain curves, are shown in Fig. 4.42 and Fig. 4.43, respectively. Among them, ODS IN625 in all conditions demonstrates superior strength and ductility at 700 °C, compared to its STD counterparts.

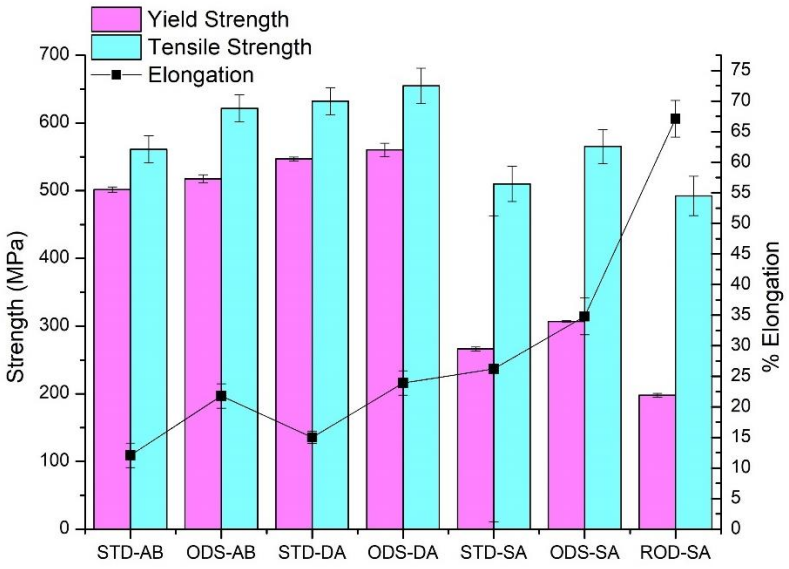

Figure 4.42 Mechanical properties of STD and ODS IN625, in AB, DA and SA conditions, and conventionally produced rod in SA condition, at 700 °C.

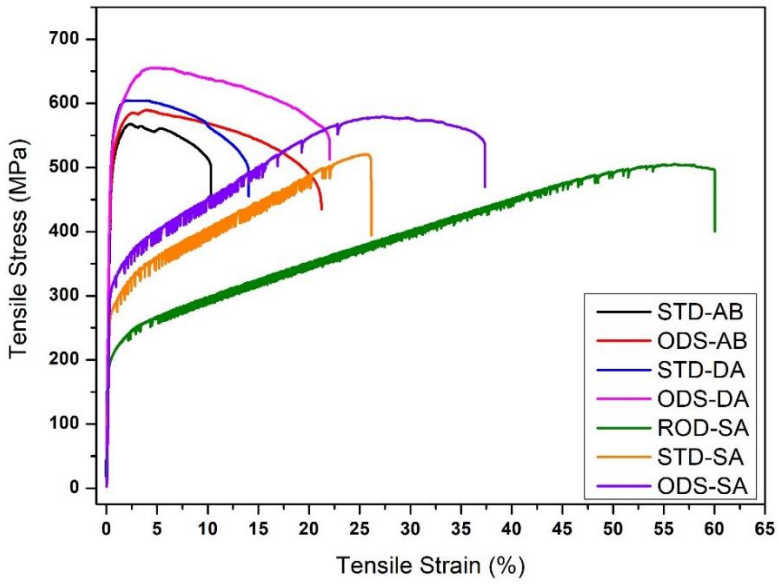

Figure 4.43 Stress vs. strain diagram for STD and ODS IN625, in AB, DA and SA conditions, and conventionally produced rod in SA condition, at 700 °C.

CHAPTER 5

CONCLUSION

In this study, it is aimed to design an alloy with enhanced strength by adding yttria and hafnium to the IN625 composition. Standard (STD) and oxide dispersion strengthened (ODS) IN625 alloys were produced using L-PBF. By the addition of yttria and Hf into the IN625 composition, an alloy superior in strength was intended to be achieved. Parameter matrices were designed both for alloy production and heat treatments, with the goal of optimizing mechanical properties at both RT and elevated temperatures. Solutionizing and aging (SA), as well as direct aging (DA), heat treatments have been applied to the as-built (AB) samples to increase the number of nano-oxides and to promote the formation of reinforcing γ'' and arguably, δ phases. Based on the experimental results obtained in this study following conclusions can be drawn:

- An effective mechanical mixing of the yttria, Hf and IN625 powders has been achieved via ball milling. It was found that 5 mm diameter balls deformed the IN625 powders in short durations which makes them inapplicable for L-PBF due to reduced flow properties. Thus, mechanical mixing was successfully obtained using the mixture of 0.5 and 1 mm diameter balls at 200 rpm for 100 minutes, without changing the sphericity of the IN625 powders.

- The parameter matrix for L-PBF has revealed that higher densities are obtained at moderate scan speed and laser power, while gas and keyhole porosities become more prominent at extreme values of these parameters. The optimal parameter set, consisting of 285 W laser power and 960 mm/s scan speed, resulted in over 99.9% densification for both STD and ODS IN625 alloys.

- Microstructural characterization studies have been carried out using SEM equipped with EDX detector. Common features of L-PBF, such as columnar and cellular structures, along with sub-micron carbides and Laves phases were observed. Coarse Y-Hf-O precipitates have been detected in the ODS IN625 alloy. EDX elemental mapping and point analysis have further confirmed the presence of mentioned phases.

- Both alloys showed a somewhat random texture in the AB condition, demonstrated by the EBSD analyses. From their IPF maps, grain sizes of the STD and ODS IN625 were found to be 12.1 μm 10.9 μm and, respectively. The slight grain size decrease has been attributed to the grain refinement effect induced by the nano-oxides. The assessment on the grain boundaries, along with the residual stress evaluation were carried out using grain boundary maps and KAM maps.

- The formation of the nano-oxides and their particle size distribution have been displayed and quantified using BFTEM micrographs of the AB ODS IN625. The average particle size of the Y-Hf-O oxides was found to be ~30 nm. The composition of the nano-oxides were quantified using STEM-HAADF. Nano-oxides were identified mostly as Y-Hf-O, although formations of Y-Hf-(Ti)-O were also observed.

- Mechanical properties of the AB alloys were properly assessed by tensile testing parallel to the building direction (BD). At room temperature (RT), mechanical properties of the AB alloys were found to be competitive, while ODS IN625 has shown far better mechanical properties, with increased ductility at 700 °C. Additional determination of mechanical properties was performed via hardness measurements at RT and results were compatible with the hardness and strength conversions.

- DA heat treatment of the AB samples have been carried out at 700 °C, for 24 hours. Melt-pool boundaries were preseverved with no grain coarsening, indicating the thermal stability of IN625 at 700 °C. Microstructural

investigation revelad the formation of the deleterious δ phase as well as grain boundary carbides at a micron scale. Nevertheless, their presence did not significantly affect the mechanical properties. In fact, tensile tests at 700 °C have shown that ODS IN625 has superior strength, as well as improved ductility, defying the traditional strength and ductility tradeoff.

Consequently, achieved mechanical performance and microstructural stability at elevated temperatures has been shown to be a good first step for developing novel materials for the next-generation nuclear reactors, especially MSRs. The improvement of toughness in the ODS IN625 at 700 °C makes it possibly a promising candidate for such applications. However, further studies on the long-term radiation exposure of the ODS alloy along with its corrosion resistance are necessary to fully confirm its suitability for MSR environments.

5.1 Future Work Suggestions

- As stated in the previous section, long-term radiation exposure testing must be conducted at elevated temperatures. This can be done by means of proton and neutron irradiation over an extended period of time.
- Assessment of the formation of radiation-induced defects along with their effect on the mechanical properties and nano-particles must be carried out focusing on dislocation loops, voids and phase stability under irradiation.
- Corrosion tests of the ODS IN625 in molten salt environments such as FLiNaK and FLiBe should be performed to determine the corrosion resistance, especially for MSR applications.
- A comprehensive mechanical property assessment should be conducted to fully understand the alloy’s long-term performance. This includes creep testing at elevated temperatures, as well as high-cycle and low-cycle fatigue testing, to evaluate the durability of the ODS IN625 under cyclic loading conditions.

- Nanoindentation studies can be applied to assess local variations in the mechanical properties, especially near grain boundaries and nano oxides.
- Further optimization of ODS can be attained by attempting other mixing strategies, such as resonant acoustic mixing or cryogenic ball milling, to improve oxide dispersion and homogeneity.
- The addition of alternative oxide formers, such as titanium and zirconium, known for refining nano-oxides, should be explored to enhance particle size distribution and overall mechanical properties.
- In terms of additive manufacturing, parameters such as hatch spacing and layer thickness can be varied to evaluate their effect on the production of ODS IN625. Larger components should also be produced to evaluate scalability of the L-PBF of ODS alloys.

REFERENCES

[1] Y. Huang, Drivers of rising global energy demand: The importance of spatial lag and error dependence, Energy 76 (2014) 254–263. https://doi.org/10.1016/j.energy.2014.07.093.

[2] M. Tvaronavičienė, J. Baublys, J. Raudeliūnienė, D. Jatautaitė, Global energy consumption peculiarities and energy sources, in: Energy Transformation Towards Sustainability, Elsevier, 2020: pp. 1–49. https://doi.org/10.1016/B978-0-12-817688-7.00001-X.

[3] H. Khatib, IEA World Energy Outlook 2011—A comment, Energy Policy 48 (2012) 737–743. https://doi.org/10.1016/j.enpol.2012.06.007.

[4] H.-W. Schiffer, WEC energy policy scenarios to 2050, Energy Policy 36 (2008) 2464–2470. https://doi.org/10.1016/j.enpol.2008.02.045.

[5] S. Ghasemian, A. Faridzad, P. Abbaszadeh, A. Taklif, A. Ghasemi, R. Hafezi, An overview of global energy scenarios by 2040: identifying the driving forces using cross-impact analysis method, International Journal of Environmental Science and Technology 21 (2024) 7749–7772. https://doi.org/10.1007/s13762-020-02738-5.

[6] C. Sun, Y. Wang, M.D. McMurtrey, N.D. Jerred, F. Liou, J. Li, Additive manufacturing for energy: A review, Applied Energy 282 (2021) 116041–116041. https://doi.org/10.1016/j.apenergy.2020.116041.

[7] J.J. Siirola, Speculations on global energy demand and supply going forward, Current Opinion in Chemical Engineering 5 (2014) 96–100. https://doi.org/10.1016/j.coche.2014.07.002.

[8] T. Kober, H.-W. Schiffer, M. Densing, E. Panos, Global energy perspectives to 2060 – WEC's World Energy Scenarios 2019, Energy Strategy Reviews 31 (2020) 100523–100523. https://doi.org/10.1016/j.esr.2020.100523.

[9] Z. Xue, Y. Xu, Y. Han, F. Gao, W. Jiang, Y. Zhu, K. Li, Q. Guo, J. Sun, Energy Internet: A Novel Green Roadmap for Meeting the Global Energy Demand, in: IEEE, 2021: pp. 3855–3860. https://doi.org/10.1109/EI252483.2021.9713467.

[10] D.J. Arent, A. Wise, R. Gelman, The status and prospects of renewable energy for combating global warming, Energy Economics 33 (2011) 584–593. https://doi.org/10.1016/j.eneco.2010.11.003.

[11] S. Sadekin, S. Zaman, M. Mahfuz, R. Sarkar, Nuclear power as foundation of a clean energy future: A review, Energy Procedia 160 (2019) 513–518. https://doi.org/10.1016/j.egypro.2019.02.200.

[12] D.S. Siqueira, J. de Almeida Meystre, M.Q. Hilário, D.H.D. Rocha, G.J. Menon, R.J. da Silva, Current perspectives on nuclear energy as a global climate change mitigation option, Mitigation and Adaptation Strategies for Global Change 24 (2019) 749–777. https://doi.org/10.1007/s11027-018-9829-5.

[13] R. Prăvălie, G. Bandoc, Nuclear energy: Between global electricity demand, worldwide decarbonisation imperativeness, and planetary environmental implications, Journal of Environmental Management 209 (2018) 81–92. https://doi.org/10.1016/j.jenvman.2017.12.043.

[14] I. Hore-Lacy, ELECTRICITY TODAY AND TOMORROW, in: Nuclear Energy in the 21st Century, Elsevier, 2007: pp. 21–36. https://doi.org/10.1016/B978-012373622-2/50005-2.

[15] M.D. Mathew, Nuclear energy: A pathway towards mitigation of global warming, Progress in Nuclear Energy 143 (2022) 104080–104080. https://doi.org/10.1016/j.pnucene.2021.104080.

[16] I. Hore-Lacy, ENERGY USE, in: Nuclear Energy in the 21st Century, Elsevier, 2007: pp. 11–19. https://doi.org/10.1016/B978-012373622-2/50004-0.

[17] B.W. Brook, A. Alonso, D.A. Meneley, J. Misak, T. Blees, J.B. van Erp, Why nuclear energy is sustainable and has to be part of the energy mix, Sustainable Materials and Technologies 1–2 (2014) 8–16. https://doi.org/10.1016/j.susmat.2014.11.001.

[18] V. Albino, L. Ardito, R.M. Dangelico, A. Messeni Petruzzelli, Understanding the development trends of low-carbon energy technologies: A patent analysis, Applied Energy 135 (2014) 836–854. https://doi.org/10.1016/j.apenergy.2014.08.012.

[19] G.P. Hammond, Nuclear energy into the twenty-first century, Applied Energy 54 (1996) 327–344. https://doi.org/10.1016/0306-2619(96)00003-7.

[20] A. Bersano, S. Segantin, History of nuclear power plants development, in: Nuclear Power Reactor Designs, Elsevier, 2024: pp. 3–40. https://doi.org/10.1016/B978-0-323-99880-2.00001-1.

[21] S.M. Goldberg, R. Rosner, Nuclear Reactors: Generation to Generation, (2011).

[22] D. Buckthorpe, Introduction to Generation IV nuclear reactors, in: Structural Materials for Generation IV Nuclear Reactors, Elsevier, 2017: pp. 1–22. https://doi.org/10.1016/B978-0-08-100906-2.00001-X.

[23] D. LeBlanc, Molten salt reactors: A new beginning for an old idea, Nuclear Engineering and Design 240 (2010) 1644–1656. https://doi.org/10.1016/j.nucengdes.2009.12.033.

[24] V.V. Ignatiev, O.S. Feynberg, A.V. Zagnitko, A.V. Merzlyakov, A.I. Surenkov, A.V. Panov, V.G. Subbotin, V.K. Afonichkin, V.A. Khokhlov, M.V. Kormilitsyn, Molten-salt reactors: new possibilities, problems and solutions, Atomic Energy 112 (2012) 157–165. https://doi.org/10.1007/s10512-012-9537-2.

[25] Y. Wang, C. Zhu, M. Zhang, W. Zhou, Molten salt reactors, in: Nuclear Power Reactor Designs, Elsevier, 2024: pp. 163–183. https://doi.org/10.1016/B978-0-323-99880-2.00009-6.

[26] B.M. Elsheikh, Safety assessment of molten salt reactors in comparison with light water reactors, Journal of Radiation Research and Applied Sciences 6 (2013) 63–70. https://doi.org/10.1016/j.jrras.2013.10.008.

[27] C. Le Brun, Molten salts and nuclear energy production, Journal of Nuclear Materials 360 (2007) 1–5. https://doi.org/10.1016/j.jnucmat.2006.08.017.

[28] J. Serp, M. Allibert, O. Beneš, S. Delpech, O. Feynberg, V. Ghetta, D. Heuer, D. Holcomb, V. Ignatiev, J.L. Kloosterman, L. Luzzi, E. Merle-Lucotte, J. Uhlíř, R. Yoshioka, D. Zhimin, The molten salt reactor (MSR) in generation IV: Overview and perspectives, Progress in Nuclear Energy 77 (2014) 308–319. https://doi.org/10.1016/j.pnucene.2014.02.014.

[29] G.S. Was, D. Petti, S. Ukai, S. Zinkle, Materials for future nuclear energy systems, Journal of Nuclear Materials 527 (2019) 151837–151837. https://doi.org/10.1016/j.jnucmat.2019.151837.

[30] K.L. Murty, I. Charit, Structural materials for Gen-IV nuclear reactors: Challenges and opportunities, Journal of Nuclear Materials 383 (2008) 189–195. https://doi.org/10.1016/j.jnucmat.2008.08.044.

[31] G. Locatelli, M. Mancini, N. Todeschini, Generation IV nuclear reactors: Current status and future prospects, Energy Policy 61 (2013) 1503–1520. https://doi.org/10.1016/j.enpol.2013.06.101.

[32] P. Calderoni, P. Sharpe, H. Nishimura, T. Terai, Control of molten salt corrosion of fusion structural materials by metallic beryllium, Journal of Nuclear Materials 386–388 (2009) 1102–1106. https://doi.org/10.1016/j.jnucmat.2008.12.292.

[33] L. Olson, K. Sridharan, M. Anderson, T. Allen, Nickel-plating for active metal dissolution resistance in molten fluoride salts, Journal of Nuclear Materials 411 (2011) 51–59. https://doi.org/10.1016/j.jnucmat.2011.01.032.

[34] X. Chen, Y. Li, Y. Zhu, B. Yang, Enhanced irradiation and corrosion resistance of 316LN stainless steel with high densities of dislocations and twins, Journal of Nuclear Materials 517 (2019) 234–240. https://doi.org/10.1016/j.jnucmat.2019.02.016.

[35] V. Ignatiev, A. Surenkov, Alloys compatibility in molten salt fluorides: Kurchatov Institute related experience, Journal of Nuclear Materials 441 (2013) 592–603. https://doi.org/10.1016/j.jnucmat.2013.05.007.

[36] N. Oono, S. Ukai, S. Kondo, O. Hashitomi, A. Kimura, Irradiation effects in oxide dispersion strengthened (ODS) Ni-base alloys for Gen. IV nuclear reactors, Journal of Nuclear Materials 465 (2015) 835–839. https://doi.org/10.1016/j.jnucmat.2015.06.057.

[37] A. Kollová, K. Pauerová, Superalloys - Characterization, Usage and Recycling, Manufacturing Technology 22 (2022) 550–557. https://doi.org/10.21062/mft.2022.070.

[38] M.J. Donachie, S.J. Donachie, Superalloys for High Temperatures—a Primer, in: Superalloys: A Technical Guide, ASM International, 2002: pp. 1–9. https://doi.org/10.31399/asm.tb.stg2.t61280001.

[39] H. Kitaguchi, Microstructure-Property Relationship in Advanced Ni-Based Superalloys, in: Metallurgy - Advances in Materials and Processes, InTech, 2012. https://doi.org/10.5772/52011.

[40] S. Gialanella, A. Malandruccolo, Aerospace Alloys, Springer International Publishing, Cham, 2020. https://doi.org/10.1007/978-3-030-24440-8.

[41] I.G. Akande, O.O. Oluwole, O.S.I. Fayomi, O.A. Odunlami, Overview of mechanical, microstructural, oxidation properties and high-temperature applications of superalloys, Materials Today: Proceedings 43 (2021) 2222–2231. https://doi.org/10.1016/j.matpr.2020.12.523.

[42] J.B. Singh, Introduction, in: Alloy 625, Springer, Singapore, 2022: pp. 1–27. https://doi.org/10.1007/978-981-19-1562-8_1.

[43] S.K. Selvaraj, G. Sundaramali, S. Jithin Dev, R. Srii Swathish, R. Karthikeyan, K.E. Vijay Vishaal, V. Paramasivam, Recent Advancements in the Field of Ni-Based Superalloys, Advances in Materials Science and Engineering 2021 (2021) 1–60. https://doi.org/10.1155/2021/9723450.

[44] D. Coutsouradis, A. Davin, M. Lamberigts, Cobalt-based superalloys for applications in gas turbines, Materials Science and Engineering 88 (1987) 11–19. https://doi.org/10.1016/0025-5416(87)90061-9.

[45] R.C. Reed, Introduction, in: The Superalloys, Cambridge University Press, 2006: pp. 1–32. https://doi.org/10.1017/CBO9780511541285.003.

[46] H. Wen, X. Tang, J. Jin, C. Cai, H. Yang, Q. Teng, Q. Wei, X. Wang, C. Zheng, Y. He, J. Guo, Effect of extrusion ratios on microstructure evolution and strengthening mechanisms of a novel P/M nickel-based superalloy, Materials Science and Engineering: A 847 (2022) 143356–143356. https://doi.org/10.1016/j.msea.2022.143356.

[47] B. Geddes, H. Leon, X. Huang, Phases and Microstructure of Superalloys, in: Superalloys: Alloying and Performance, ASM International, 2010: pp. 25–57. https://doi.org/10.31399/asm.tb.sap.t53000025.

[48] D.V.V. Satyanarayana, N. Eswara Prasad, Nickel-Based Superalloys, in: Aerospace Materials and Material Technologies, 2017: pp. 199–228. https://doi.org/10.1007/978-981-10-2134-3_9.

[49] M.J. Donachie, S.J. Donachie, Understanding Superalloy Metallurgy, in: Superalloys: A Technical Guide, ASM International, 2002: pp. 25–39. https://doi.org/10.31399/asm.tb.stg2.t61280025.

[50] A.P. Mouritz, Superalloys for gas turbine engines, in: Introduction to Aerospace Materials, Elsevier, 2012: pp. 251–267. https://doi.org/10.1533/9780857095152.251.

[51] J.B. Singh, Physical Metallurgy of Alloy 625, in: Alloy 625, Springer, Singapore, 2022: pp. 67–110. https://doi.org/10.1007/978-981-19-1562-8_3.

[52] R.C. Reed, The physical metallurgy of nickel and its alloys, in: The Superalloys, Cambridge University Press, 2006: pp. 33–120. https://doi.org/10.1017/CBO9780511541285.004.

[53] Z. Wang, O. Muránsky, H. Zhu, T. Wei, A. Sokolova, K. Short, R.N. Wright, On the kinetics of gamma prime (γ') precipitation and its strengthening mechanism in Alloy 617 during a long-term thermal aging, Materialia 11 (2020) 100682–100682. https://doi.org/10.1016/j.mtla.2020.100682.

[54] L. Finet, L. Nazé, V. Maurel, V.A. Esin, In Situ Study of Temperature Stability and Precipitation Kinetics of $$\delta $$ and $$\eta $$ Phases in Nickel Base Superalloys, Metallurgical and Materials Transactions A 53 (2022) 3627–3638. https://doi.org/10.1007/s11661-022-06771-6.

[55] A. Mostafaei, R. Ghiaasiaan, I.-T. Ho, S. Strayer, K.-C. Chang, N. Shamsaei, S. Shao, S. Paul, A.-C. Yeh, S. Tin, A.C. To, Additive manufacturing of nickel-based superalloys: A state-of-the-art review on process-structure-defect-property relationship, Progress in Materials Science 136 (2023) 101108–101108. https://doi.org/10.1016/j.pmatsci.2023.101108.

[56] J. Belan, GCP and TCP Phases Presented in Nickel-base Superalloys, Materials Today: Proceedings 3 (2016) 936–941. https://doi.org/10.1016/j.matpr.2016.03.024.

[57] W. Jiang, J. Lu, H. Guan, M. Wang, X. Cheng, L. Liu, X. Liu, J. Wang, Y. Zhang, Z. Zhang, W. Lin, J. Hu, Study of pre-precipitated δ phase promoting deformation twinning and recrystallization behavior of Inconel 718 superalloy during hot compression, Materials & Design 226 (2023) 111693–111693. https://doi.org/10.1016/j.matdes.2023.111693.

[58] S. Kobayashi, T. Otsuka, R. Watanabe, K. Sagitani, M. Okamoto, K. Tokutomi, Alloying Effects on the Competition Between Discontinuous Precipitation Versus Continuous Precipitation of δ/η Phases in Model Ni-Based Superalloys, in: Superalloys 2020, Springer, Cham, 2020: pp. 163–170. https://doi.org/10.1007/978-3-030-51834-9_16.

[59] G.H. Hessinger, Powder Metallurgy of Superalloys, Butterworth-Heinemann, 1984.

[60] R.C. Reed, C.M.F. Rae, Physical Metallurgy of the Nickel-Based Superalloys, in: Physical Metallurgy, Elsevier, 2014: pp. 2215–2290. https://doi.org/10.1016/B978-0-444-53770-6.00022-8.

[61] Ö. Özgün, H.Ö. Gülsoy, R. Yılmaz, F. Fındık, Microstructural and mechanical characterization of injection molded 718 superalloy powders, Journal of Alloys and Compounds 576 (2013) 140–153. https://doi.org/10.1016/j.jallcom.2013.04.042.

[62] O. Sifi, M.E.A. Djeghlal, Y. Mebdoua, S. Djeraf, F. Hadj-Larbi, The effect of the solution and aging treatments on the microstructures and microhardness of nickel-based superalloy, Applied Physics A 126 (2020) 345–345. https://doi.org/10.1007/s00339-020-03517-2.

[63] L.R. Liu, T. Jin, N.R. Zhao, X.F. Sun, H.R. Guan, Z.Q. Hu, Formation of carbides and their effects on stress rupture of a Ni-base single crystal superalloy, Materials Science and Engineering: A 361 (2003) 191–197. https://doi.org/10.1016/S0921-5093(03)00517-3.

[64] X. Liu, J. Fan, D. Jiao, B. Tang, H. Kou, G. Sha, J. Li, Achieving excellent strength-ductility combination in an Inconel 625 superalloy via short-term stress-aging treatment, Scripta Materialia 231 (2023) 115458–115458. https://doi.org/10.1016/j.scriptamat.2023.115458.

[65] J. Li, J. Sun, J. Liu, X. Sun, The precipitation and effect of topologically close-packed phases in Ni-based single crystal superalloys, Journal of Materials Science & Technology 173 (2024) 149–169. https://doi.org/10.1016/j.jmst.2023.05.074.

[66] Z. Zhang, Z. Wen, Z. Yue, Effects of tensile/compressive creeps on microstructure evolution of nickel-based single crystal superalloys, Journal of Alloys and Compounds 851 (2021) 156767–156767. https://doi.org/10.1016/j.jallcom.2020.156767.

[67] A.S. Wilson, K.A. Christofidou, A. Evans, M.C. Hardy, H.J. Stone, Comparison of Methods for Quantification of Topologically Close-Packed Phases in Ni-Based Superalloys, Metallurgical and Materials Transactions A 50 (2019) 5925–5934. https://doi.org/10.1007/s11661-019-05442-3.

[68] T. Bhujangrao, F. Veiga, A. Suárez, E. Iriondo, F.G. Mata, High-Temperature Mechanical Properties of IN718 Alloy: Comparison of Additive Manufactured and Wrought Samples, Crystals 10 (2020) 689–689. https://doi.org/10.3390/cryst10080689.

[69] O.P. Sinha, M. Chatterjee, V.V.R.S. Sarma, S.N. Jha, Effect of residual elements on high performance nickel base superalloys for gas turbines and strategies for manufacture, Bulletin of Materials Science 28 (2005) 379–382. https://doi.org/10.1007/BF02704253.

[70] N.C. Ferreri, S.C. Vogel, M. Knezevic, Determining volume fractions of γ, γ′, γ″, δ, and MC-carbide phases in Inconel 718 as a function of its processing history using an advanced neutron diffraction procedure, Materials Science and Engineering: A 781 (2020) 139228–139228. https://doi.org/10.1016/j.msea.2020.139228.

[71] B. Geddes, H. Leon, X. Huang, Strengthening Mechanisms, in: Superalloys: Alloying and Performance, ASM International, 2010: pp. 17–24. https://doi.org/10.31399/asm.tb.sap.t53000017.

[72] H.A. Kishawy, A. Hosseini, Superalloys, in: Machining Difficult-to-Cut Materials, Springer, Cham, 2019: pp. 97–137. https://doi.org/10.1007/978-3-319-95966-5_4.

[73] J.B. Singh, Mechanical Behavior of Alloy 625, in: Alloy 625, 2022: pp. 111–174. https://doi.org/10.1007/978-981-19-1562-8_4.

[74] M. Ashby, H. Shercliff, D. Cebon, Beyond elasticity: plasticity, yielding and ductility, in: Materials, Elsevier, 2019: pp. 133–168. https://doi.org/10.1016/B978-0-08-102376-1.00006-8.

[75] A.J. Goodfellow, Strengthening mechanisms in polycrystalline nickel-based superalloys, Materials Science and Technology 34 (2018) 1793–1808. https://doi.org/10.1080/02670836.2018.1461594.

[76] M. Shih, J. Miao, M. Mills, M. Ghazisaeidi, Stacking fault energy in concentrated alloys, Nature Communications 12 (2021) 3590–3590. https://doi.org/10.1038/s41467-021-23860-z.

[77] R. Su, D. Neffati, Y. Zhang, J. Cho, J. Li, H. Wang, Y. Kulkarni, X. Zhang, The influence of stacking faults on mechanical behavior of advanced materials, Materials Science and Engineering: A 803 (2021) 140696–140696. https://doi.org/10.1016/j.msea.2020.140696.

[78] A.C. Yeh, S. Tin, Effects of Ru and Re additions on the high temperature flow stresses of Ni-base single crystal superalloys, Scripta Materialia 52 (2005) 519–524. https://doi.org/10.1016/j.scriptamat.2004.10.039.

[79] M. Pröbstle, S. Neumeier, P. Feldner, R. Rettig, H.E. Helmer, R.F. Singer, M. Göken, Improved creep strength of nickel-base superalloys by optimized γ/γ′ partitioning behavior of solid solution strengthening elements, Materials Science and Engineering: A 676 (2016) 411–420. https://doi.org/10.1016/j.msea.2016.08.121.

[80] A. Takahashi, M. Kawanabe, N.M. Ghoniem, γ-precipitate strengthening in nickel-based superalloys, Philosophical Magazine 90 (2010) 3767–3786. https://doi.org/10.1080/14786435.2010.497470.

[81] T. Gladman, Precipitation hardening in metals, Materials Science and Technology 15 (1999) 30–36. https://doi.org/10.1179/026708399773002782.

[82] M.J. Donachie, S.J. Donachie, Structure/Property Relationships, in: Superalloys: A Technical Guide, ASM International, 2002: pp. 211–286. https://doi.org/10.31399/asm.tb.stg2.t61280211.

[83] L. Thébaud, P. Villechaise, C. Crozet, A. Devaux, D. Béchet, J.-M. Franchet, A.-L. Rouffié, M. Mills, J. Cormier, Is there an optimal grain size for creep resistance in Ni-based disk superalloys?, Materials Science and Engineering: A 716 (2018) 274–283. https://doi.org/10.1016/j.msea.2017.12.104.

[84] F. Abe, Strengthening mechanisms in steel for creep and creep rupture, in: Creep-Resistant Steels, Elsevier, 2008: pp. 279–304. https://doi.org/10.1533/9781845694012.2.279.

[85] E. Akca, A. Gürsel, A Review on Superalloys and IN718 Nickel-Based INCONEL Superalloy, Periodicals of Engineering and Natural Sciences (PEN) 3 (2015). https://doi.org/10.21533/pen.v3i1.43.

[86] J.B. Singh, Fabrication, in: Alloy 625, 2022: pp. 189–239. https://doi.org/10.1007/978-981-19-1562-8_6.

[87] N. Blaes, D. Bokelmann, A. Diwo, B. Donth, Manufacture of Large Ni-Base Ingots and Forgings, in: The Minerals, Metals & Materials Society, 2016: pp. 601–608. https://doi.org/10.7449/Superalloys/2016/Superalloys_2016_601_608.

[88] Y. Zhang, J. Li, Characterization of the Microstructure Evolution and Microsegregation in a Ni-Based Superalloy under Super-High Thermal Gradient Directional Solidification, MATERIALS TRANSACTIONS 53 (2012) 1910–1914. https://doi.org/10.2320/matertrans.M2012173.

[89] X.G. Zheng, Y.-N. Shi, L.H. Lou, Healing Process of Casting Pores in a Ni-based Superalloy by Hot Isostatic Pressing, Journal of Materials Science & Technology 31 (2015) 1151–1157. https://doi.org/10.1016/j.jmst.2015.07.004.

[90] G. Sjöberg, Casting Superalloys for Structural Applications, in: Superalloy 718 and Derivatives, Wiley, 2010: pp. 116–130. https://doi.org/10.1002/9781118495223.ch8.

[91] M. Armstrong, H. Mehrabi, N. Naveed, An overview of modern metal additive manufacturing technology, Journal of Manufacturing Processes 84 (2022) 1001–1029. https://doi.org/10.1016/j.jmapro.2022.10.060.

[92] H. Soni, M. Gor, G. Singh Rajput, P. Sahlot, A comprehensive review on effect of process parameters and heat treatment on tensile strength of additively manufactured Inconel-625, Materials Today: Proceedings 47 (2021) 4866–4871. https://doi.org/10.1016/j.matpr.2021.06.126.

[93] Y.T. Tang, C. Panwisawas, J.N. Ghoussoub, Y. Gong, J.W.G. Clark, A.A.N. Németh, D.G. McCartney, R.C. Reed, Alloys-by-design: Application to new superalloys for additive manufacturing, Acta Materialia 202 (2021) 417–436. https://doi.org/10.1016/j.actamat.2020.09.023.

[94] M.P. Haines, V.V. Rielli, S. Primig, N. Haghdadi, Powder bed fusion additive manufacturing of Ni-based superalloys: a review of the main microstructural constituents and characterization techniques, Journal of Materials Science 57 (2022) 14135–14187. https://doi.org/10.1007/s10853-022-07501-4.

[95] B. Graybill, M. Li, D. Malawey, C. Ma, J.-M. Alvarado-Orozco, E. Martinez-Franco, Additive Manufacturing of Nickel-Based Superalloys, in: American Society of Mechanical Engineers, 2018. https://doi.org/10.1115/MSEC2018-6666.

[96] L. Hitzler, M. Merkel, W. Hall, A. Öchsner, A Review of Metal Fabricated with Laser- and Powder-Bed Based Additive Manufacturing Techniques: Process, Nomenclature, Materials, Achievable Properties, and its Utilization in the Medical Sector, Advanced Engineering Materials 20 (2018). https://doi.org/10.1002/adem.201700658.

[97] C. Guo, G. Li, S. Li, X. Hu, H. Lu, X. Li, Z. Xu, Y. Chen, Q. Li, J. Lu, Q. Zhu, Additive manufacturing of Ni-based superalloys: Residual stress, mechanisms of crack formation and strategies for crack inhibition, Nano Materials Science 5 (2023) 53–77. https://doi.org/10.1016/j.nanoms.2022.08.001.

[98] O. Adegoke, J. Andersson, H. Brodin, R. Pederson, Review of Laser Powder Bed Fusion of Gamma-Prime-Strengthened Nickel-Based Superalloys, Metals 10 (2020) 996–996. https://doi.org/10.3390/met10080996.

[99] S. Li, Q. Wei, Y. Shi, Z. Zhu, D. Zhang, Microstructure Characteristics of Inconel 625 Superalloy Manufactured by Selective Laser Melting, Journal of Materials Science & Technology 31 (2015) 946–952. https://doi.org/10.1016/j.jmst.2014.09.020.

[100] J. Wang, R. Zhu, Y. Liu, L. Zhang, Understanding melt pool characteristics in laser powder bed fusion: An overview of single- and multi-track melt pools for process optimization, Advanced Powder Materials 2 (2023) 100137–100137. https://doi.org/10.1016/j.apmate.2023.100137.

[101] O. Andreau, I. Koutiri, P. Peyre, J.-D. Penot, N. Saintier, E. Pessard, T. De Terris, C. Dupuy, T. Baudin, Texture control of 316L parts by modulation of the melt pool morphology in selective laser melting, Journal of Materials Processing Technology 264 (2019) 21–31. https://doi.org/10.1016/j.jmatprotec.2018.08.049.

[102] Q. Jia, D. Gu, Selective laser melting additive manufacturing of Inconel 718 superalloy parts: Densification, microstructure and properties, Journal of Alloys and Compounds 585 (2014) 713–721. https://doi.org/10.1016/j.jallcom.2013.09.171.

[103] B. Liu, G. Fang, L. Lei, X. Yan, Predicting the porosity defects in selective laser melting (SLM) by molten pool geometry, International Journal of Mechanical Sciences 228 (2022) 107478–107478. https://doi.org/10.1016/j.ijmecsci.2022.107478.

[104] I. Yadroitsev, I. Yadroitsava, A step-by-step guide to the L-PBF process, in: Fundamentals of Laser Powder Bed Fusion of Metals, Elsevier, 2021: pp. 39–77. https://doi.org/10.1016/B978-0-12-824090-8.00026-3.

[105] C.Y. Yap, C.K. Chua, Z.L. Dong, Z.H. Liu, D.Q. Zhang, L.E. Loh, S.L. Sing, Review of selective laser melting: Materials and applications, Applied Physics Reviews 2 (2015). https://doi.org/10.1063/1.4935926.

[106] M. Ramsperger, S. Eichler, Electron Beam Based Additive Manufacturing of Alloy 247 for Turbine Engine Application: From Research towards Industrialization,

Metallurgical and Materials Transactions A 54 (2023) 1730–1743. https://doi.org/10.1007/s11661-022-06955-0.

[107] J.A. Gonzalez, J. Mireles, S.W. Stafford, M.A. Perez, C.A. Terrazas, R.B. Wicker, Characterization of Inconel 625 fabricated using powder-bed-based additive manufacturing technologies, Journal of Materials Processing Technology 264 (2019) 200–210. https://doi.org/10.1016/j.jmatprotec.2018.08.031.

[108] P.K. Gokuldoss, S. Kolla, J. Eckert, Additive Manufacturing Processes: Selective Laser Melting, Electron Beam Melting and Binder Jetting—Selection Guidelines, Materials 10 (2017) 672–672. https://doi.org/10.3390/ma10060672.

[109] H.M. Alojaly, A. Hammouda, K.Y. Benyounis, Review of recent developments on metal matrix composites with particulate reinforcement, in: Comprehensive Materials Processing, Elsevier, 2024: pp. 350–373. https://doi.org/10.1016/B978-0-323-96020-5.00041-8.

[110] M.M. Attallah, R. Jennings, X. Wang, L.N. Carter, Additive manufacturing of Ni-based superalloys: The outstanding issues, MRS Bulletin 41 (2016) 758–764. https://doi.org/10.1557/mrs.2016.211.

[111] Ashish, N. Ahmad, P. Gopinath, A. Vinogradov, 3D Printing in Medicine, in: 3D Printing Technology in Nanomedicine, Elsevier, 2019: pp. 1–22. https://doi.org/10.1016/B978-0-12-815890-6.00001-3.

[112] A. Dass, A. Moridi, State of the Art in Directed Energy Deposition: From Additive Manufacturing to Materials Design, Coatings 9 (2019) 418–418. https://doi.org/10.3390/coatings9070418.

[113] M. Zenou, L. Grainger, Additive manufacturing of metallic materials, in: Additive Manufacturing, Elsevier, 2018: pp. 53–103. https://doi.org/10.1016/B978-0-12-812155-9.00003-7.

[114] Y. Hu, X. Lin, Y. Li, Y. Ou, X. Gao, Q. Zhang, W. Li, W. Huang, Microstructural evolution and anisotropic mechanical properties of Inconel 625 superalloy fabricated by directed energy deposition, Journal of Alloys and Compounds 870 (2021) 159426–159426. https://doi.org/10.1016/j.jallcom.2021.159426.

[115] A. Jinoop, C. Paul, K. Bindra, Laser-assisted directed energy deposition of nickel super alloys: A review, Proceedings of the Institution of Mechanical Engineers, Part L: Journal of Materials: Design and Applications 233 (2019) 2376–2400. https://doi.org/10.1177/1464420719852658.

[116] R. Wang, J. Wang, T. Cao, R. Zhao, X. Lu, W. Guan, H. Tao, S. Shuai, X. Songzhe, W. Xuan, C. Panwisawas, C. Chen, Z. Ren, Microstructure characteristics of a René N5 Ni-based single-crystal superalloy prepared by laser-directed energy deposition, Additive Manufacturing 61 (2023) 103363–103363. https://doi.org/10.1016/j.addma.2022.103363.

[117] S.-H. Li, P. Kumar, S. Chandra, U. Ramamurty, Directed energy deposition of metals: processing, microstructures, and mechanical properties, International Materials Reviews 68 (2023) 605–647. https://doi.org/10.1080/09506608.2022.2097411.

[118] V. Madhavadas, D. Srivastava, U. Chadha, S. Aravind Raj, M.T.H. Sultan, F.S. Shahar, A.U.M. Shah, A review on metal additive manufacturing for intricately shaped aerospace components, CIRP Journal of Manufacturing Science and Technology 39 (2022) 18–36. https://doi.org/10.1016/j.cirpj.2022.07.005.

[119] B. Blakey-Milner, P. Gradl, G. Snedden, M. Brooks, J. Pitot, E. Lopez, M. Leary, F. Berto, A. du Plessis, Metal additive manufacturing in aerospace: A review, Materials & Design 209 (2021) 110008–110008. https://doi.org/10.1016/j.matdes.2021.110008.

[120] S. Pratheesh Kumar, S. Elangovan, R. Mohanraj, J.R. Ramakrishna, A review on properties of Inconel 625 and Inconel 718 fabricated using direct energy deposition, Materials Today: Proceedings 46 (2021) 7892–7906. https://doi.org/10.1016/j.matpr.2021.02.566.

[121] M.M. de Oliveira, A.A. Couto, G.F.C. Almeida, D.A.P. Reis, N.B. de Lima, R. Baldan, Mechanical Behavior of Inconel 625 at Elevated Temperatures, Metals 9 (2019) 301–301. https://doi.org/10.3390/met9030301.

[122] B. Dubiel, J. Sieniawski, Precipitates in Additively Manufactured Inconel 625 Superalloy, Materials 12 (2019) 1144–1144. https://doi.org/10.3390/ma12071144.

[123] V. Shankar, K. Bhanu Sankara Rao, S.L. Mannan, Microstructure and mechanical properties of Inconel 625 superalloy, Journal of Nuclear Materials 288 (2001) 222–232. https://doi.org/10.1016/S0022-3115(00)00723-6.

[124] S. Floreen, G.E. Fuchs, W.J. Yang, The Metallurgy of Alloy 625, in: TMS, 1994: pp. 13–37. https://doi.org/10.7449/1994/Superalloys_1994_13_37.

[125] A. Kumar, V. Shankar, T. Jayakumar, K.B.S. Rao, B. Raj, Correlation of microstructure and mechanical properties with ultrasonic velocity in the Ni-based superalloy Inconel 625, Philosophical Magazine A 82 (2002) 2529–2545. https://doi.org/10.1080/01418610208240051.

[126] H.C. Pai, M. Sundararaman, B.C. Maji, A. Biswas, M. Krishnan, Influence of Mo addition on the solvus temperature of Ni2(Cr,Mo) phase in Ni2(Cr,Mo) alloys, Journal of Alloys and Compounds 491 (2010) 159–164. https://doi.org/10.1016/j.jallcom.2009.10.204.

[127] J. Mittra, S. Banerjee, R. Tewari, G.K. Dey, Fracture behavior of Alloy 625 with different precipitate microstructures, Materials Science and Engineering: A 574 (2013) 86–93. https://doi.org/10.1016/j.msea.2013.03.021.

[128] G. Marchese, G. Piscopo, S. Lerda, A. Salmi, E. Atzeni, S. Biamino, Heat-Treated Inconel 625 by Laser Powder Bed Fusion: Microstructure, Tensile Properties, and Residual Stress Evolution, Journal of Materials Engineering and Performance 33 (2024) 6825–6834. https://doi.org/10.1007/s11665-024-09235-7.

[129] M.J. Donachie, S.J. Donachie, Heat Treating, in: Superalloys: A Technical Guide, ASM International, 2002: pp. 135–147. https://doi.org/10.31399/asm.tb.stg2.t61280135.

[130] X. Liu, J. Fan, P. Zhang, K. Cao, Z. Wang, F. Chen, D. Liu, B. Tang, H. Kou, J. Li, Influence of heat treatment on Inconel 625 superalloy sheet: carbides, γ’’, δ phase precipitation and tensile deformation behavior, Journal of Alloys and

Compounds 930 (2023) 167522–167522. https://doi.org/10.1016/j.jallcom.2022.167522.

[131] V. Luna, L. Trujillo, A. Gamon, E. Arrieta, L.E. Murr, R.B. Wicker, C. Katsarelis, P.R. Gradl, F. Medina, Comprehensive and Comparative Heat Treatment of Additively Manufactured Inconel 625 Alloy and Corresponding Microstructures and Mechanical Properties, Journal of Manufacturing and Materials Processing 6 (2022) 107–107. https://doi.org/10.3390/jmmp6050107.

[132] H. Chandler, ed., Heat Treater's Guide : Practices and Procedures for Nonferrous Alloys, ASM International, 1996.

[133] Y.L. Hu, X. Lin, S.Y. Zhang, Y.M. Jiang, X.F. Lu, H.O. Yang, W.D. Huang, Effect of solution heat treatment on the microstructure and mechanical properties of Inconel 625 superalloy fabricated by laser solid forming, Journal of Alloys and Compounds 767 (2018) 330–344. https://doi.org/10.1016/j.jallcom.2018.07.087.

[134] Y. Wang, Y. Su, Z. Dai, Effect of Solution and Aging Heat Treatment on the Microstructure and Mechanical Properties of Inconel 625 Deposited Metal, Crystals 14 (2024) 764–764. https://doi.org/10.3390/cryst14090764.

[135] Y. Hu, X. Lin, Y. Li, S. Zhang, Q. Zhang, W. Chen, W. Li, W. Huang, Influence of heat treatments on the microstructure and mechanical properties of Inconel 625 fabricated by directed energy deposition, Materials Science and Engineering: A 817 (2021) 141309–141309. https://doi.org/10.1016/j.msea.2021.141309.

[136] A. SAFARZADE, M. SHARIFITABAR, M. SHAFIEE AFARANI, Effects of heat treatment on microstructure and mechanical properties of Inconel 625 alloy fabricated by wire arc additive manufacturing process, Transactions of Nonferrous Metals Society of China 30 (2020) 3016–3030. https://doi.org/10.1016/S1003-6326(20)65439-5.

[137] G. Marchese, M. Lorusso, S. Parizia, E. Bassini, J.-W. Lee, F. Calignano, D. Manfredi, M. Terner, H.-U. Hong, D. Ugues, M. Lombardi, S. Biamino, Influence of heat treatments on microstructure evolution and mechanical properties of Inconel

625 processed by laser powder bed fusion, Materials Science and Engineering: A 729 (2018) 64–75. https://doi.org/10.1016/j.msea.2018.05.044.

[138] T. Keya, I. Bikmukhametov, A. Shmatok, G. Harvill, L.N. Brewer, G.B. Thompson, M. Andurkar, S.M. Thompson, V. O'Donnell, J. Gahl, B.C. Prorok, Evolution of microstructure and its influence on the mechanical behavior of LPBF Inconel 625 upon direct aging, Manufacturing Letters 35 (2023) 732–742. https://doi.org/10.1016/j.mfglet.2023.09.009.

[139] G. Marchese, S. Parizia, M. Rashidi, A. Saboori, D. Manfredi, D. Ugues, M. Lombardi, E. Hryha, S. Biamino, The role of texturing and microstructure evolution on the tensile behavior of heat-treated Inconel 625 produced via laser powder bed fusion, Materials Science and Engineering: A 769 (2020) 138500–138500. https://doi.org/10.1016/j.msea.2019.138500.

[140] C. Li, R. White, X.Y. Fang, M. Weaver, Y.B. Guo, Microstructure evolution characteristics of Inconel 625 alloy from selective laser melting to heat treatment, Materials Science and Engineering: A 705 (2017) 20–31. https://doi.org/10.1016/j.msea.2017.08.058.

[141] G.P. Dinda, A.K. Dasgupta, J. Mazumder, Laser aided direct metal deposition of Inconel 625 superalloy: Microstructural evolution and thermal stability, Materials Science and Engineering: A 509 (2009) 98–104. https://doi.org/10.1016/j.msea.2009.01.009.

[142] J. Nguejio, F. Szmytka, S. Hallais, A. Tanguy, S. Nardone, M. Godino Martinez, Comparison of microstructure features and mechanical properties for additive manufactured and wrought nickel alloys 625, Materials Science and Engineering: A 764 (2019) 138214–138214. https://doi.org/10.1016/j.msea.2019.138214.

[143] E.A. Lass, M.R. Stoudt, M.E. Williams, M.B. Katz, L.E. Levine, T.Q. Phan, T.H. Gnaeupel-Herold, D.S. Ng, Formation of the Ni3Nb δ-Phase in Stress-Relieved Inconel 625 Produced via Laser Powder-Bed Fusion Additive Manufacturing, Metallurgical and Materials Transactions A 48 (2017) 5547–5558. https://doi.org/10.1007/s11661-017-4304-6.

[144] E.A. Lass, M.R. Stoudt, M.B. Katz, M.E. Williams, Precipitation and dissolution of δ and γ″ during heat treatment of a laser powder-bed fusion produced Ni-based superalloy, Scripta Materialia 154 (2018) 83–86. https://doi.org/10.1016/j.scriptamat.2018.05.025.

[145] F. Zhang, L.E. Levine, A.J. Allen, M.R. Stoudt, G. Lindwall, E.A. Lass, M.E. Williams, Y. Idell, C.E. Campbell, Effect of heat treatment on the microstructural evolution of a nickel-based superalloy additive-manufactured by laser powder bed fusion, Acta Materialia 152 (2018) 200–214. https://doi.org/10.1016/j.actamat.2018.03.017.

[146] X. Xing, X. Di, B. Wang, The effect of post-weld heat treatment temperature on the microstructure of Inconel 625 deposited metal, Journal of Alloys and Compounds 593 (2014) 110–116. https://doi.org/10.1016/j.jallcom.2013.12.224.

[147] M.R. Stoudt, E.A. Lass, D.S. Ng, M.E. Williams, F. Zhang, C.E. Campbell, G. Lindwall, L.E. Levine, The Influence of Annealing Temperature and Time on the Formation of δ-Phase in Additively-Manufactured Inconel 625, Metallurgical and Materials Transactions A 49 (2018) 3028–3037. https://doi.org/10.1007/s11661-018-4643-y.

[148] G. Lindwall, C.E. Campbell, E.A. Lass, F. Zhang, M.R. Stoudt, A.J. Allen, L.E. Levine, Simulation of TTT Curves for Additively Manufactured Inconel 625, Metallurgical and Materials Transactions A 50 (2019) 457–467. https://doi.org/10.1007/s11661-018-4959-7.

[149] J.A. Glerum, A. De Luca, M.L. Schuster, C. Kenel, C. Leinenbach, D.C. Dunand, Effect of oxide dispersoids on precipitation-strengthened Al-1.7Zr (wt %) alloys produced by laser powder-bed fusion, Additive Manufacturing 56 (2022) 102933–102933. https://doi.org/10.1016/j.addma.2022.102933.

[150] C.W. Park, J.M. Byun, W.J. Choi, S.Y. Lee, Y.D. Kim, Improvement of high temperature mechanical properties of Ni-based oxide dispersion strengthened alloys by preferential formation of Y-Ti-O complex oxide, Materials Science and Engineering: A 740–741 (2019) 363–367. https://doi.org/10.1016/j.msea.2018.10.004.

[151] T. Boegelein, S.N. Dryepondt, A. Pandey, K. Dawson, G.J. Tatlock, Mechanical response and deformation mechanisms of ferritic oxide dispersion strengthened steel structures produced by selective laser melting, Acta Materialia 87 (2015) 201–215. https://doi.org/10.1016/j.actamat.2014.12.047.

[152] E. Aydogan, S.A. Maloy, O. Anderoglu, C. Sun, J.G. Gigax, L. Shao, F.A. Garner, I.E. Anderson, J.J. Lewandowski, Effect of tube processing methods on microstructure, mechanical properties and irradiation response of 14YWT nanostructured ferritic alloys, Acta Materialia 134 (2017) 116–127. https://doi.org/10.1016/j.actamat.2017.05.053.

[153] M.Y. Yalcin, A.A. Gokbayrak, O. Duygulu, B. Derin, J.D. Poplawsky, O. El-Atwani, E. Aydogan, Laser powder bed fusion of oxide dispersion-strengthened IN718 alloys: A complementary study on microstructure and mechanical properties, Materials Science and Engineering: A 903 (2024) 146663–146663. https://doi.org/10.1016/j.msea.2024.146663.

[154] T. Chen, J.G. Gigax, L. Price, D. Chen, S. Ukai, E. Aydogan, S.A. Maloy, F.A. Garner, L. Shao, Temperature dependent dispersoid stability in ion-irradiated ferritic-martensitic dual-phase oxide-dispersion-strengthened alloy: Coherent interfaces vs. incoherent interfaces, Acta Materialia 116 (2016) 29–42. https://doi.org/10.1016/j.actamat.2016.05.042.

[155] E. Aydogan, N. Almirall, G.R. Odette, S.A. Maloy, O. Anderoglu, L. Shao, J.G. Gigax, L. Price, D. Chen, T. Chen, F.A. Garner, Y. Wu, P. Wells, J.J. Lewandowski, D.T. Hoelzer, Stability of nanosized oxides in ferrite under extremely high dose self ion irradiations, Journal of Nuclear Materials 486 (2017) 86–95. https://doi.org/10.1016/j.jnucmat.2017.01.015.

[156] A. Certain, S. Kuchibhatla, V. Shutthanandan, D.T. Hoelzer, T.R. Allen, Radiation stability of nanoclusters in nano-structured oxide dispersion strengthened (ODS) steels, Journal of Nuclear Materials 434 (2013) 311–321. https://doi.org/10.1016/j.jnucmat.2012.11.021.

[157] J. Ribis, S. Lozano-Perez, Nano-cluster stability following neutron irradiation in MA957 oxide dispersion strengthened material, Journal of Nuclear Materials 444 (2014) 314–322. https://doi.org/10.1016/j.jnucmat.2013.10.010.

[158] X. Mao, Y.-B. Chun, C.-H. Han, J. Jang, Precipitation behavior of oxide dispersion strengthened Alloy 617, Journal of Materials Science 52 (2017) 13626–13635. https://doi.org/10.1007/s10853-017-1437-3.

[159] M.A. Moghadasi, M. Nili-Ahmadabadi, F. Forghani, H.S. Kim, Development of an oxide-dispersion-strengthened steel by introducing oxygen carrier compound into the melt aided by a general thermodynamic model, Scientific Reports 6 (2016) 38621–38621. https://doi.org/10.1038/srep38621.

[160] J. Wang, S. Liu, B. Xu, J. Zhang, M. Sun, D. Li, Research progress on preparation technology of oxide dispersion strengthened steel for nuclear energy, International Journal of Extreme Manufacturing 3 (2021) 032001–032001. https://doi.org/10.1088/2631-7990/abff1a.

[161] M.B. Wilms, S.-K. Rittinghaus, M. Goßling, B. Gökce, Additive manufacturing of oxide-dispersion strengthened alloys: Materials, synthesis and manufacturing, Progress in Materials Science 133 (2023) 101049–101049. https://doi.org/10.1016/j.pmatsci.2022.101049.

[162] R.L. Klueh, J.P. Shingledecker, R.W. Swindeman, D.T. Hoelzer, Oxide dispersion-strengthened steels: A comparison of some commercial and experimental alloys, Journal of Nuclear Materials 341 (2005) 103–114. https://doi.org/10.1016/j.jnucmat.2005.01.017.

[163] L. Raman, K. Gothandapani, B.S. Murty, Austenitic Oxide Dispersion Strengthened Steels : A Review, Defence Science Journal 66 (2016) 316–316. https://doi.org/10.14429/dsj.66.10205.

[164] A. Patra, Oxide Dispersion Strengthened Refractory Alloys, CRC Press, Boca Raton, 2022. https://doi.org/10.1201/9781003201007.

[165] W. He, F. Liu, L. Tan, L. Huang, Y. Nie, G. Wang, X. Zhan, Z. Qin, Bimodal-grained high-strength nickel-base ODS alloy fabricated by mechanical alloying and

hot extrusion, Materials Today Communications 26 (2021) 101921–101921. https://doi.org/10.1016/j.mtcomm.2020.101921.

[166] S. Pasebani, A.K. Dutt, J. Burns, I. Charit, R.S. Mishra, Oxide dispersion strengthened nickel based alloys via spark plasma sintering, Materials Science and Engineering: A 630 (2015) 155–169. https://doi.org/10.1016/j.msea.2015.01.066.

[167] C. Suryanarayana, Mechanical alloying and milling, Progress in Materials Science 46 (2001) 1–184. https://doi.org/10.1016/S0079-6425(99)00010-9.

[168] C.-L. Chen, Y.-M. Dong, Effect of mechanical alloying and consolidation process on microstructure and hardness of nanostructured Fe–Cr–Al ODS alloys, Materials Science and Engineering: A 528 (2011) 8374–8380. https://doi.org/10.1016/j.msea.2011.08.041.

[169] Y. Shi, Z. Lu, L. Yu, R. Xie, Y. Ren, G. Yang, Microstructure and tensile properties of Zr-containing ODS-FeCrAl alloy fabricated by laser additive manufacturing, Materials Science and Engineering: A 774 (2020) 138937–138937. https://doi.org/10.1016/j.msea.2020.138937.

[170] C. Kenel, A. De Luca, S.S. Joglekar, C. Leinenbach, D.C. Dunand, Evolution of Y2O3 dispersoids during laser powder bed fusion of oxide dispersion strengthened Ni-Cr-Al-Ti γ/γ’ superalloy, Additive Manufacturing 47 (2021) 102224–102224. https://doi.org/10.1016/j.addma.2021.102224.

[171] C. Doñate-Buendia, P. Kürnsteiner, F. Stern, M.B. Wilms, R. Streubel, I.M. Kusoglu, J. Tenkamp, E. Bruder, N. Pirch, S. Barcikowski, K. Durst, J.H. Schleifenbaum, F. Walther, B. Gault, B. Gökce, Microstructure formation and mechanical properties of ODS steels built by laser additive manufacturing of nanoparticle coated iron-chromium powders, Acta Materialia 206 (2021) 116566–116566. https://doi.org/10.1016/j.actamat.2020.116566.

[172] Y. Zhong, L. Liu, J. Zou, X. Li, D. Cui, Z. Shen, Oxide dispersion strengthened stainless steel 316L with superior strength and ductility by selective laser melting, Journal of Materials Science & Technology 42 (2020) 97–105. https://doi.org/10.1016/j.jmst.2019.11.004.

[173] C. Qiu, A new approach to synthesise high strength nano-oxide dispersion strengthened alloys, Journal of Alloys and Compounds 790 (2019) 1023–1033. https://doi.org/10.1016/j.jallcom.2019.03.221.

[174] G. Wang, L. Huang, Z. Liu, Z. Qin, W. He, F. Liu, C. Chen, Y. Nie, Process optimization and mechanical properties of oxide dispersion strengthened nickel-based superalloy by selective laser melting, Materials & Design 188 (2020) 108418–108418. https://doi.org/10.1016/j.matdes.2019.108418.

[175] L. Yu, Z. Lu, S. Peng, X. Li, Effect of Al/Ti ratio on γ′ and oxide dispersion strengthening in Ni-based ODS superalloys, Materials Science and Engineering: A 845 (2022) 143240–143240. https://doi.org/10.1016/j.msea.2022.143240.

[176] T. Liu, L. Wang, C. Wang, H. Shen, H. Zhang, Feasibility of using Y2Ti2O7 nanoparticles to fabricate high strength oxide dispersion strengthened Fe–Cr–Al steels, Materials & Design 88 (2015) 862–870. https://doi.org/10.1016/j.matdes.2015.08.118.

[177] P. Dou, S. Jiang, L. Qiu, A. Kimura, Effects of contents of Al, Zr and Ti on oxide particles in Fe–15Cr–2W–0.35Y2O3 ODS steels, Journal of Nuclear Materials 531 (2020) 152025–152025. https://doi.org/10.1016/j.jnucmat.2020.152025.

[178] C. Lu, Z. Lu, R. Xie, Z. Li, C. Liu, L. Wang, Effect of Y/Ti atomic ratio on microstructure of oxide dispersion strengthened alloys, Materials Characterization 134 (2017) 35–40. https://doi.org/10.1016/j.matchar.2017.10.004.

[179] L. Li, M. Saber, W. Xu, Y. Zhu, C.C. Koch, R.O. Scattergood, High-temperature grain size stabilization of nanocrystalline Fe–Cr alloys with Hf additions, Materials Science and Engineering: A 613 (2014) 289–295. https://doi.org/10.1016/j.msea.2014.06.099.

[180] H. Xu, Z. Lu, D. Wang, C. Liu, Microstructural evolution in a new Fe based ODS alloy processed by mechanical alloying, Nuclear Materials and Energy 7 (2016) 1–4. https://doi.org/10.1016/j.nme.2016.04.006.

[181] Y. Uchidi, S. Ohnuki, N. Hashimoto, T. Suda, T. Nagai, T. Shibayama, K. Hamada, N. Akasaka, S. Yamashita, S. Ohstuka, T. Yoshitake, Effect of Minor

Alloying Element on Dispersing Nano-particles in ODS Steel, MRS Proceedings 981 (2006) 0981–09. https://doi.org/10.1557/PROC-981-0981-JJ07-09.

[182] R. Gao, T. Zhang, X.P. Wang, Q.F. Fang, C.S. Liu, Effect of zirconium addition on the microstructure and mechanical properties of ODS ferritic steels containing aluminum, Journal of Nuclear Materials 444 (2014) 462–468. https://doi.org/10.1016/j.jnucmat.2013.10.038.

[183] H. Xu, Z. Lu, D. Wang, C. Liu, Microstructure Refinement and Strengthening Mechanisms of a 9Cr Oxide Dispersion Strengthened Steel by Zirconium Addition, Nuclear Engineering and Technology 49 (2017) 178–188. https://doi.org/10.1016/j.net.2017.01.002.

[184] H. Dong, L. Yu, Y. Liu, C. Liu, H. Li, J. Wu, Effect of hafnium addition on the microstructure and tensile properties of aluminum added high-Cr ODS steels, Journal of Alloys and Compounds 702 (2017) 538–545. https://doi.org/10.1016/j.jallcom.2017.01.298.

[185] P. Dou, A. Kimura, R. Kasada, T. Okuda, M. Inoue, S. Ukai, S. Ohnuki, T. Fujisawa, F. Abe, S. Jiang, Z. Yang, TEM and HRTEM study of oxide particles in an Al-alloyed high-Cr oxide dispersion strengthened ferritic steel with Hf addition, Journal of Nuclear Materials 485 (2017) 189–201. https://doi.org/10.1016/j.jnucmat.2016.12.001.

[186] Q. Tang, T. Hoshino, S. Ukai, B. Leng, S. Hayashi, Y. Wang, Refinement of Oxide Particles by Addition of Hf in Ni-0.5 mass%Al-1 mass% Y2O3 Alloys, MATERIALS TRANSACTIONS 51 (2010) 2019–2024. https://doi.org/10.2320/matertrans.M2010163.

[187] Z. Kang, H. Shen, Z. Bai, H. Zhao, T. Liu, Influences of different hydride nanoparticles on microstructure and mechanical properties of 14Cr 3Al ferritic ODS steels, Powder Technology 343 (2019) 137–144. https://doi.org/10.1016/j.powtec.2018.11.029.

[188] Y. Huang, H. Zhang, M.A. Auger, Z. Hong, H. Ning, M.J. Gorley, P.S. Grant, M.J. Reece, H. Yan, S.G. Roberts, Microstructural comparison of effects of hafnium and titanium additions in spark-plasma-sintered Fe-based oxide-dispersion

strengthened alloys, Journal of Nuclear Materials 487 (2017) 433–442. https://doi.org/10.1016/j.jnucmat.2017.02.030.

[189] M.Z. Ghodsi, S. Khademzadeh, E. Marzbanrad, M.H. Razmpoosh, N. De Marchi, E. Toyserkani, Development of Yttria-stabilized zirconia reinforced Inconel 625 metal matrix composite by laser powder bed fusion, Materials Science and Engineering: A 827 (2021) 142037–142037. https://doi.org/10.1016/j.msea.2021.142037.

[190] A.B. Spierings, T. Bauer, K. Dawson, A. Colella, K. Wegener, Processing ODS Modified In625 Using Selective Laser Melting, Proceedings of the 25th Annual International Solid Freeform Fabrication Symposium 2015 (2015) 803–812.

[191] M. Li, L. Wang, H. Yang, S. Zhang, X. Lin, W. Huang, Microstructure and mechanical properties of Y2O3 strengthened Inconel 625 alloy fabricated by selective laser melting, Materials Science and Engineering: A 854 (2022) 143813–143813. https://doi.org/10.1016/j.msea.2022.143813.

[192] K. Arnold, G. Tatlock, C. Kenel, A. Colella, P. Matteazzi, High temperature isothermal oxidation behaviour of an oxide dispersion strengthened derivative of IN625, Materials at High Temperatures 35 (2018) 141–150. https://doi.org/10.1080/09603409.2017.1393145.

[193] X. Zou, K. Yang, J. Li, X. Xie, L. Pan, Microstructural evolution and high-temperature oxidation behavior of oxide dispersion strengthened Inconel 625 superalloy fabricated by directed energy deposition, Materials Characterization 210 (2024) 113810–113810. https://doi.org/10.1016/j.matchar.2024.113810.

[194] K. Inaekyan, A. Kreitcberg, S. Turenne, V. Brailovski, Microstructure and mechanical properties of laser powder bed-fused IN625 alloy, Materials Science and Engineering: A 768 (2019) 138481. https://doi.org/10.1016/j.msea.2019.138481.

[195] C.O.L. Almeida, L.H.L. Lima, M. dos Santos Pereira, Springback comparison between DP600 and DP800 steel grades, Materials Research Express 7 (2020) 016598–016598. https://doi.org/10.1088/2053-1591/ab664e.

[196] L. Wang, M. Li, X. Lin, T. Gui, H. Chai, W. Huang, The distribution of Y2O3 during selective laser melting of IN625/Y2O3 core-shell powders, Advanced

Powder Technology 35 (2024) 104609–104609. https://doi.org/10.1016/j.apt.2024.104609.

[197] N.T. Aboulkhair, N.M. Everitt, I. Ashcroft, C. Tuck, Reducing porosity in AlSi10Mg parts processed by selective laser melting, Additive Manufacturing 1–4 (2014) 77–86. https://doi.org/10.1016/j.addma.2014.08.001.

[198] L. Scime, J. Beuth, Melt pool geometry and morphology variability for the Inconel 718 alloy in a laser powder bed fusion additive manufacturing process, Additive Manufacturing 29 (2019) 100830–100830. https://doi.org/10.1016/j.addma.2019.100830.

[199] S.K. Nayak, S.K. Mishra, A.N. Jinoop, C.P. Paul, K.S. Bindra, Experimental Studies on Laser Additive Manufacturing of Inconel-625 Structures Using Powder Bed Fusion at 100 μm Layer Thickness, Journal of Materials Engineering and Performance 29 (2020) 7636–7647. https://doi.org/10.1007/s11665-020-05215-9.

[200] M. Balbaa, S. Mekhiel, M. Elbestawi, J. McIsaac, On selective laser melting of Inconel 718: Densification, surface roughness, and residual stresses, Materials & Design 193 (2020) 108818–108818. https://doi.org/10.1016/j.matdes.2020.108818.

[201] C. Guo, S. Li, S. Shi, X. Li, X. Hu, Q. Zhu, R.M. Ward, Effect of processing parameters on surface roughness, porosity and cracking of as-built IN738LC parts fabricated by laser powder bed fusion, Journal of Materials Processing Technology 285 (2020) 116788–116788. https://doi.org/10.1016/j.jmatprotec.2020.116788.

[202] G.M. Volpato, U. Tetzlaff, M.C. Fredel, A comprehensive literature review on laser powder bed fusion of Inconel superalloys, Additive Manufacturing 55 (2022) 102871–102871. https://doi.org/10.1016/j.addma.2022.102871.

[203] L. Afroz, R. Das, M. Qian, M. Easton, M. Brandt, Fatigue behaviour of laser powder bed fusion (L-PBF) Ti–6Al–4V, Al–Si–Mg and stainless steels: a brief overview, International Journal of Fracture 235 (2022) 3–46. https://doi.org/10.1007/s10704-022-00641-3.

[204] C. Weingarten, D. Buchbinder, N. Pirch, W. Meiners, K. Wissenbach, R. Poprawe, Formation and reduction of hydrogen porosity during selective laser

melting of AlSi10Mg, Journal of Materials Processing Technology 221 (2015) 112–120. https://doi.org/10.1016/j.jmatprotec.2015.02.013.

[205] G. Marchese, X. Garmendia Colera, F. Calignano, M. Lorusso, S. Biamino, P. Minetola, D. Manfredi, Characterization and Comparison of Inconel 625 Processed by Selective Laser Melting and Laser Metal Deposition, Advanced Engineering Materials 19 (2017). https://doi.org/10.1002/adem.201600635.

[206] L.N. Carter, X. Wang, N. Read, R. Khan, M. Aristizabal, K. Essa, M.M. Attallah, Process optimisation of selective laser melting using energy density model for nickel based superalloys, Materials Science and Technology 32 (2016) 657–661. https://doi.org/10.1179/1743284715Y.0000000108.

[207] M. Mazur, M. Benoit, M. Easton, M. Brandt, Selective laser melting of Inconel 625 alloy with reduced defect formation, Journal of Laser Applications 32 (2020). https://doi.org/10.2351/7.0000093.

[208] J.K. Chaurasia, A.N. Jinoop, P. P, C.P. Paul, K.S. Bindra, S. Bontha, Study of melt pool geometry and solidification microstructure during laser surface melting of Inconel 625 alloy, Optik 246 (2021) 167766–167766. https://doi.org/10.1016/j.ijleo.2021.167766.

[209] F. Yang, L. Dong, X. Hu, X. Zhou, Z. Xie, F. Fang, Effect of solution treatment temperature upon the microstructure and mechanical properties of hot rolled Inconel 625 alloy, J Mater Sci 55 (2020) 5613–5626. https://doi.org/10.1007/s10853-020-04375-2.

[210] E. Pu, W. Zheng, Z. Song, K. Zhang, F. Yang, H. Lu, H. Dong, Evolution of microstructure and tensile properties during solution treatment of nickel-based UNS N10276 alloy, Materials Science and Engineering: A 705 (2017) 335–347. https://doi.org/10.1016/j.msea.2017.08.101.

[211] R. Ferraresi, A. Avanzini, S. Cecchel, C. Petrogalli, G. Cornacchia, Microstructural, Mechanical, and Tribological Evolution under Different Heat Treatment Conditions of Inconel 625 Alloy Fabricated by Selective Laser Melting, Advanced Engineering Materials 24 (2022). https://doi.org/10.1002/adem.202100966.

[212] T. De Terris, O. Castelnau, Z. Hadjem-Hamouche, H. Haddadi, V. Michel, P. Peyre, Analysis of As-Built Microstructures and Recrystallization Phenomena on Inconel 625 Alloy Obtained via Laser Powder Bed Fusion (L-PBF), Metals 11 (2021) 619–619. https://doi.org/10.3390/met11040619.

[213] M. Cabrini, S. Lorenzi, C. Testa, F. Brevi, S. Biamino, P. Fino, D. Manfredi, G. Marchese, F. Calignano, T. Pastore, Microstructure and Selective Corrosion of Alloy 625 Obtained by Means of Laser Powder Bed Fusion, Materials 12 (2019) 1742–1742. https://doi.org/10.3390/ma12111742.

[214] A.M. Beese, Z. Wang, A.D. Stoica, D. Ma, Absence of dynamic strain aging in an additively manufactured nickel-base superalloy, Nat Commun 9 (2018) 2083. https://doi.org/10.1038/s41467-018-04473-5.

[215] Z. Tian, C. Zhang, D. Wang, W. Liu, X. Fang, D. Wellmann, Y. Zhao, Y. Tian, A Review on Laser Powder Bed Fusion of Inconel 625 Nickel-Based Alloy, Applied Sciences 10 (2019) 81–81. https://doi.org/10.3390/app10010081.

[216] A. Kreitcberg, V. Brailovski, S. Turenne, Effect of heat treatment and hot isostatic pressing on the microstructure and mechanical properties of Inconel 625 alloy processed by laser powder bed fusion, Materials Science and Engineering: A 689 (2017) 1–10. https://doi.org/10.1016/j.msea.2017.02.038.

[217] L.N. Brewer, M.A. Othon, L.M. Young, T.M. Angeliu, Misorientation Mapping for Visualization of Plastic Deformation via Electron Back-Scattered Diffraction, Microscopy and Microanalysis 12 (2006) 85–91. https://doi.org/10.1017/S1431927606060120.

[218] U.M. Chaudry, S.-C. Han, K. bin Tayyab, A. Farooq, W.-S. Kim, T.-S. Jun, Unraveling the anisotropic corrosion behavior along the building direction in laser powder bed fusion processed Hastelloy X, Journal of Materials Research and Technology 33 (2024) 1188–1200. https://doi.org/10.1016/j.jmrt.2024.09.115.

[219] D. Liu, X. Zhang, X. Qin, Y. Ding, High-temperature mechanical properties of Inconel-625: Role of carbides and delta phase, Materials Science and Technology 33 (2017) 1610–1617. https://doi.org/10.1080/02670836.2017.1300365.

[220] M. Liu, W. Zheng, J. Xiang, Z. Song, E. Pu, H. Feng, Grain Growth Behavior of Inconel 625 Superalloy, J. Iron Steel Res. Int. 23 (2016) 1111–1118. https://doi.org/10.1016/S1006-706X(16)30164-9.

[221] J. Malaplate, F. Mompiou, J.-L. Béchade, T. Van Den Berghe, M. Ratti, Creep behavior of ODS materials: A study of dislocations/precipitates interactions, Journal of Nuclear Materials 417 (2011) 205–208. https://doi.org/10.1016/j.jnucmat.2010.12.059.

[222] L. Yu, Z. Lu, X. Li, S. Peng, H. Li, Effect of Zr and Hf addition on microstructure and tensile properties of high-Al Ni-based ODS superalloys, Materials Science and Engineering: A 854 (2022) 143811–143811. https://doi.org/10.1016/j.msea.2022.143811.

[223] L. Yu, Z. Lu, J. Xian, X. Chen, Effect of Hf addition on evolution of microstructure and strengthening behavior in Ni-based ODS superalloy, Journal of Alloys and Compounds 941 (2023) 168933–168933. https://doi.org/10.1016/j.jallcom.2023.168933.

[224] M.A. Lebyodkin, T.A. Lebedkina, J. Brechtl, P.K. Liaw, Serrated Flow in Alloy Systems, in: J. Brechtl, P.K. Liaw (Eds.), High-Entropy Materials: Theory, Experiments, and Applications, Springer International Publishing, Cham, 2021: pp. 523–644. https://doi.org/10.1007/978-3-030-77641-1_11.

[225] Y.C. Lin, H. Yang, Y. Xin, C.-Z. Li, Effects of initial microstructures on serrated flow features and fracture mechanisms of a nickel-based superalloy, Materials Characterization 144 (2018) 9–21. https://doi.org/10.1016/j.matchar.2018.06.029.

[226] P. Rodriguez, Serrated plastic flow, Bull. Mater. Sci. 6 (1984) 653–663. https://doi.org/10.1007/BF02743993.

[227] A. Chatterjee, G. Sharma, R. Tewari, J.K. Chakravartty, Investigation of the Dynamic Strain Aging and Mechanical Properties in Alloy-625 with Different Microstructures, Metall Mater Trans A 46 (2015) 1097–1107. https://doi.org/10.1007/s11661-014-2717-z.

[228] K. Gopinath, A.K. Gogia, S.V. Kamat, U. Ramamurty, Dynamic strain ageing in Ni-base superalloy 720Li, Acta Materialia 57 (2009) 1243–1253. https://doi.org/10.1016/j.actamat.2008.11.005.

[229] X. Liu, J. Fan, Y. Song, P. Zhang, F. Chen, R. Yuan, J. Wang, B. Tang, H. Kou, J. Li, High-temperature tensile and creep behaviour of Inconel 625 superalloy sheet and its associated deformation-failure micromechanisms, Materials Science and Engineering: A 829 (2022) 142152. https://doi.org/10.1016/j.msea.2021.142152.

[230] H. Hamdi, H.R. Abedi, Thermal stability of Ni-based superalloys fabricated through additive manufacturing: A review, Journal of Materials Research and Technology 30 (2024) 4424–4476. https://doi.org/10.1016/j.jmrt.2024.04.161.

[231] M. Liu, Y. Cai, Q. Wang, Y. Jiang, T. Zou, Y. Wang, Q. Li, Y. Pei, H. Zhang, Y. Liu, Q. Wang, The low cycle fatigue property, damage mechanism, and life prediction of additively manufactured Inconel 625: Influence of temperature, Fatigue Fract Eng Mat Struct 46 (2023) 3829–3845. https://doi.org/10.1111/ffe.14106.